Lawrence Berkeley Laboratory
UNIVERSITY OF CALIFORNIA

Physics Division

A Search for Right-Handed W Bosons in $\bar{p}p$
Collisions with the DØ Detector at Fermilab

A. Goldschmidt
(Ph.D. Thesis)

January 1996

DISCLAIMER

DISCLAIMER

Portions of this document may be illegible
in electronic image products.   Images are
produced from the best available original
document.

A Search for Right-Handed W Bosons in $\bar{p}p$ Collisions with the DØ Detector at Fermilab

Azriel Goldschmidt
Ph.D. Thesis

Department of Physics
University of California, Berkeley

and

Physics Division
Ernest Orlando Lawrence Berkeley National Laboratory
University of California
Berkeley, CA 94720

January 1996

A Search for Right-Handed W Bosons in $\bar{p}p$ Collisions with the DØ Detector at Fermilab

by

Azriel Goldschmidt

B.A. (Israel Institute of Technology) 1990

A dissertation submitted in partial satisfaction of the
requirements for the degree of
Doctor of Philosophy

in

Physics

in the

GRADUATE DIVISION
of the
UNIVERSITY of CALIFORNIA at BERKELEY

Committee in charge:

Professor Mark Strovink, Chair
Professor Marjorie D. Shapiro
Professor Eugene Haller

1996

Abstract

A Search for Right-Handed W Bosons in $\bar{p}p$ Collisions with the DØ
Detector at Fermilab

by

Azriel Goldschmidt

Doctor of Philosophy in Physics

University of California at Berkeley

Professor Mark Strovink, Chair

This thesis reports on a search for right-handed W bosons (W_R). Data collected with
the DØ detector at the Fermilab Tevatron $p\bar{p}$ collider at $\sqrt{s}$ =1.8 TeV were used to search
for W_R decays into an electron and a massive right-handed neutrino $W_R^{\pm} \rightarrow e^{\pm} N_R$. Using
the inclusive electron data, mass limits independent of the N_R decay were set: $m_{W_R} > 650$
GeV/c^2 and $m_{W_R} > 720$ GeV/c^2 at the 95% confidence level, valid for $m_{N_R} < \frac{1}{2} m_{W_R}$ and
$m_{N_R} \ll m_{W_R}$ respectively (assuming Standard Model couplings). The latter also represents
a new lower limit on the mass of a heavy left-handed W boson (W') decaying into $e\nu$. In
addition, limits on m_{W_R} valid for larger values of the N_R mass were obtained assuming that
N_R decays to an electron and two jets.
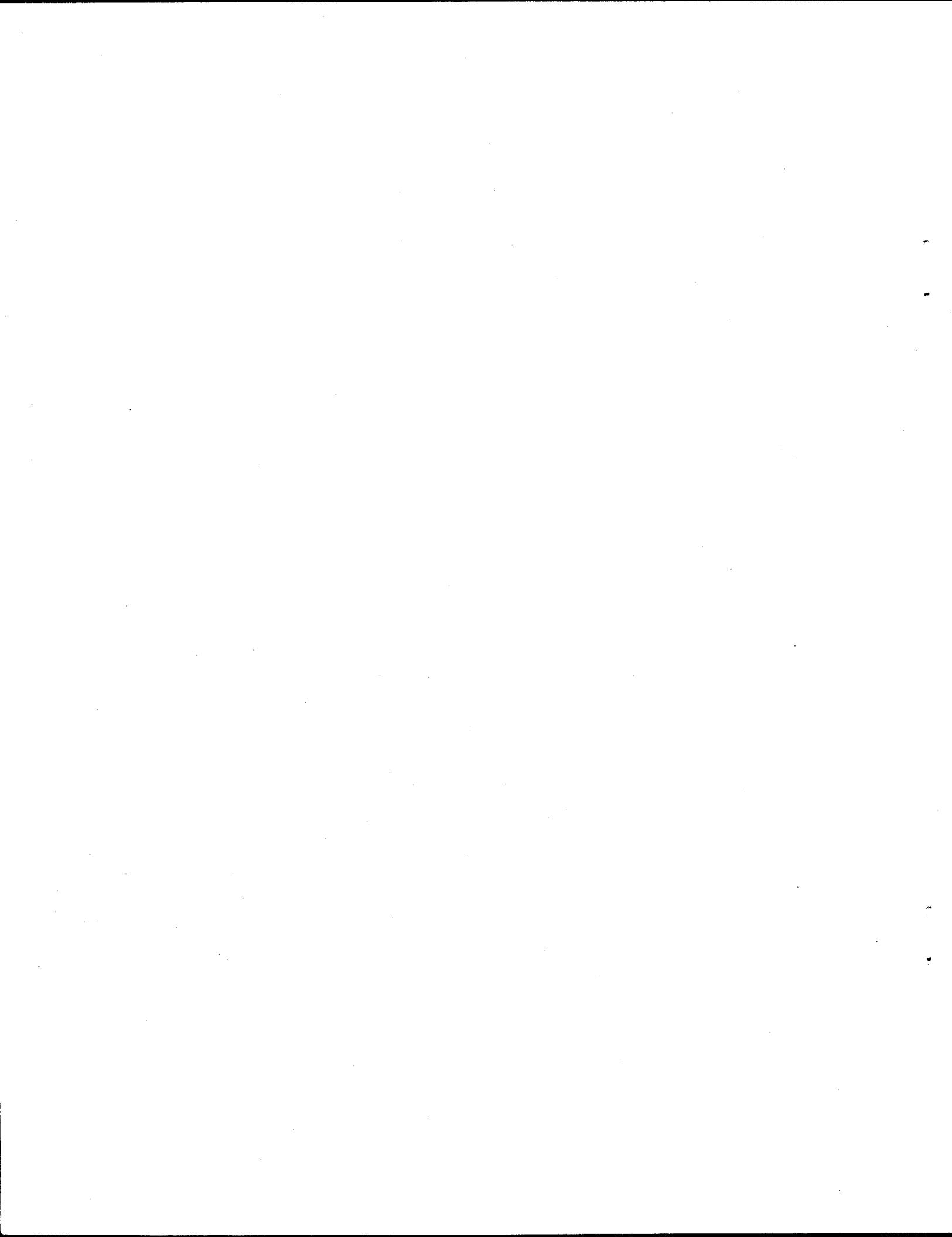
To my Mother and to my Father.

Contents

List of Figures

List of Tables

Acknowledgements

First and most important, I want to thank my advisor, Mark Strovink. For the last four years he allowed me to grow as a physicist by providing incisive and always relevant advice, while letting me choose the specific course of my research. I will always be indebted to him for his trust and support. I want also to thank Marjorie Shapiro and Eugene Haller for being part of the dissertation committee. Marjorie Shapiro, through her friendly and sincere advice, was of great help as my mentor during the first year at Berkeley.

Working on the DØ Collaboration was truly an exciting and unforgettable experience that allowed me to meet numerous excellent physicists and friends. Within those, I am especially happy to have met Danilo Pušeljić, Erich Varnes, Justin Bendich, Patrick Virador, Liang-ping Chen, Myungyun Pang, Srini Rajagopalan, Manuel Martin and Paul Rubinov. Also, thanks to all of the members of the mighty Prerna soccer team for many fun and victorious games and for their invaluable friendship.

I am also indebted to Paul Grannis, Hugh Montgomery, Ron Madaras, Dave Cutts, Nick Hadley, Wyatt Merritt and Adam Para for their inspiring leadership and for their support.

I would also like to thank Geary Eppley, Amber Boehnlein, Meena Narain, Sarah Eno and Danilo Pušeljić. Their comments and help made this thesis possible.

To my family, in Argentina, Colombia, Israel and the U.S.: thanks for your unconditional love, support and care. Special thanks to my mother, for being an infinite source of inspiration, knowledge and spirituality, and to my father for showing to me the beauty of music and for teaching me about the facts of life. Thanks also to both for giving me the best brothers and sisters a person could have.

Thanks also to Miguel Eckstein, Sacha Kopin, Suk-Joon Yoon and Pavlos Tzermias for not letting the distance get in the way of our wonderful friendships.

I want to take the opportunity to thank my teachers and professors at the Colegio Integral Rabino José Caro and at the Colegio Nacional de Buenos Aires, in Argentina, and at the Technion, in Israel. Their guidance, dedication and encouragement left an unerasable mark in me as a scientist and as a person.

A special thanks goes to Dave Buchholz for kindly allowing me to use the Northwestern University facilities, making my life a lot more pleasant and happy. Thanks also to Peter

Heimberg for the many hours of fun physics conversations and more.

Finally, I want to thank Ellisa, my wife and true companion, for her love and her liveliness, and for putting up with my always over-optimistic estimations of this graduation date.

Chapter 1

Introduction

One of the particularities of our human nature is that we aspire and attempt to understand the universe we live in and the laws that govern its perpetual transformation. In order to study some of these features and laws, it is necessary to create environments that differ substantially from our day-to-day, low energy environment. This is particularly true if one wants to inquire about the building blocks of matter and the forces between them.

One way of achieving this is by accelerating particles (such as protons or electrons) to very high energies and colliding them. These collisions can result in the creation of new particles that are more massive, and that have short lifetimes and therefore are not present in our everyday world.

However, just having a high-energy collision is not enough, many are needed. The reason for this is that only a few out of many collisions will lead to an interesting final state, such as a new particle or an unusual process. The Tevatron at Fermilab is a collider for protons and anti-protons. The DØ detector is located in one of two regions where the proton and anti-proton beams meet, causing collisions.

The subject of this thesis is a search for one such new particle, namely a right-handed W boson. Its existence is predicted in Left-Right (LR) symmetric models [1] [2] which are simple extensions of the very successful Standard Model (SM) [3] of particle physics. The motivation for the postulation of such extended models are mainly of theoretical origin. The LR models provide a natural explanation (without recurring to the ad-hoc postulates

of the SM) of the origin of parity violation in low energy experiments. In addition, should the hints from solar neutrino experiments of a non-vanishing neutrino mass be confirmed, the most natural framework in which to understand it is that of the LR models [1].

In Chapter 2 the basic features of the LR models are presented. The possible experimental signatures, and the signatures investigated in this study in particular, are also described. Finally, an overview of the existing limits on right-handed W bosons from low energy experiments and from collider experiments is presented.

Chapter 3 describes the experimental apparatus. The descriptions of the detector and trigger systems are presented with special emphasis on the systems that are most relevant to this study.

Chapter 4 contains the description of the algorithms used to reconstruct and identify the physics objects used later for the data analysis.

Chapter 5 contains the bulk of the analysis. There, the two methods used for the search are described in detail. The cuts applied to the data, as well as the calculation of the signal efficiencies and backgrounds are shown. Limits on the right-handed W boson production and decay are presented for both methods for a variety of values of the model parameters.

Finally, Chapter 6 summarizes the results of the search.

Chapter 2

Left-Right Symmetric Models

2.1 Theory

2.1.1 The Standard Model

The Standard Model (SM) [3] is a gauge field theory that unifies the weak interactions, responsible for processes such as radioactivity, and the electromagnetic interactions, responsible for the interactions between light and matter. This model is based on a $SU(2)_L \times U(1)_Y$ symmetry group. To preserve this local gauge symmetry, four massless spin 1 boson fields, three corresponding to the $SU(2)_L$ group ($W_\mu^{(1)}, W_\mu^{(2)}, W_\mu^{(3)}$) and one for the $U(1)_Y$ (B_μ), are introduced. However, this *unbroken* theory cannot account for the short range nature of the Weak Interactions (WI) that characterizes theories with massive intermediate gauge bosons. To remedy this, the principle of *spontaneously broken symmetry* (SBS) is invoked. In theories with *spontaneously broken symmetries*, the vacuum (minimum of the potential) is not invariant under the corresponding symmetry transformation. Through SBS, gauge bosons can acquire masses while preserving the renormalizability (calculability) of theory.

In the SM (through the Higgs mechanism) the physical boson states (those with definite masses) are:

$$W_\mu^\pm = \frac{1}{\sqrt{2}}(W_\mu^{(1)} \mp i W_\mu^{(2)}), \qquad (2.1)$$

corresponding to the two massive charged W bosons and

$$Z_\mu = \cos\theta_w W_\mu^{(3)} - \sin\theta_w B_\mu \quad A_\mu = \sin\theta_w W_\mu^{(3)} + \cos\theta_w B_\mu, \quad (2.2)$$

corresponding to the massive neutral Z boson and the massless photon, respectively. In Eq.2.2, θ_w is the angle that relates the gauge coupling of the $SU(2)_L$ symmetry group (g) to the charge of the electron (e):

$$g = e/\sin\theta_w. \quad (2.3)$$

The subindex in $SU(2)_L$ means that in the SM only left-handed fermions (or more precisely, negative chirality states) are transformed non-trivially under $SU(2)$ transformations. Therefore, left-handed quarks and leptons form isospin ($SU(2)$) doublets while their right-handed counterparts are singlets. For the leptons:

$$\begin{pmatrix} \nu_e \\ e \end{pmatrix}_L \quad \begin{pmatrix} \nu_\mu \\ \mu \end{pmatrix}_L \quad \begin{pmatrix} \nu_\tau \\ \tau \end{pmatrix}_L \quad e_R, \mu_R, \tau_R. \quad (2.4)$$

This assignment was chosen to reflect the maximal parity violation which is observed in low energy WI experiments.

2.1.2 Left-Right Symmetry

For more than 20 years the Standard Model has been tested against a great variety of experiments. High precision experiments, in a wide range of energy scales, are in excellent agreement with SM calculations. So far, there are no conclusive experimental results that can be ascribed to failures of the model.

There are, however, some features of the model that were purely dictated by experimental results and therefore do not have a theoretical justification. This is the case for the left handedness of the Weak Interactions.

In the SM, only the left-handed helicity projections of the lepton fields participate in the charged WI. In Left-Right (LR) symmetric models the left-handedness of the WI is a low energy phenomenon that disappears at higher energies, and it is due to a vacuum that is noninvariant under parity symmetry.

The LR models are built assuming that the interaction Lagrangian is intrinsically left-right symmetric. This basic idea is realized by replacing the gauge symmetry group structure of the SM, $SU(2)_L \times U(1)_Y$, by an enlarged group: $SU(2)_L \times SU(2)_R \times U(1)_{B-L}$.

As a result of enlarging the symmetry group, one obtains *new gauge bosons*, that mediate the right-handed weak interactions, and *right-handed neutrinos*. From the left-handed nature of the WI at presently attainable energies, we can conclude that the new gauge bosons will have higher masses than the SM's $W^\pm$ and Z^0.

The new gauge bosons can, in principle, mix with the left-handed ones to form mass eigenstates:

$$W_1 = W_L \cos\xi - W_R \sin\xi \tag{2.5}$$

$$W_2 = W_L \sin\xi + W_R \cos\xi. \tag{2.6}$$

The W_1 will then be the predominant gauge boson participating in low energy charged WI processes.

The LR models predict the existence of right-handed neutrinos, but do not constrain their specific nature. Right-handed neutrinos could have Dirac masses, in which case their mass would be the same as the light neutrino's or could have a Majorana mass. The case of the Majorana mass for the right-handed neutrino can, in some models, explain the lightness of the left handed neutrino. This happens through the so called See-Saw [4] Mechanism.

2.1.3   The Models

LR models are based on the gauge group $SU(2)_L \times SU(2)_R \times U(1)_{B-L}$ [2] [1]. The right-handed fermions transform non-trivially under the $SU(2)_R$ group, allowing charged right-handed currents.

For simplicity, only the first family of quarks and leptons is shown here:

$$Q \equiv \begin{pmatrix} u \\ d \end{pmatrix}, \quad \psi \equiv \begin{pmatrix} \nu_e \\ e \end{pmatrix}. \tag{2.7}$$

The assignments are given with 3 numbers: The third component of the weak isospin with respect to the $SU(2)_L$ symmetry (I_{3L}), the corresponding number for $SU(2)_R$ (I_{3R}) and the baryon number B minus lepton number L, corresponding to the $U(1)$:

$$Q_L : (\tfrac{1}{2}, 0, \tfrac{1}{3}), \tag{2.8}$$

$$Q_R : (0, \tfrac{1}{2}, \tfrac{1}{3}), \tag{2.9}$$

$$\psi_L : (\tfrac{1}{2}, 0, -1), \tag{2.10}$$

$$\psi_R : (0, \tfrac{1}{2}, -1). \tag{2.11}$$

The electric charge formula is then:

$$Q = I_{3L} + I_{3R} + \frac{B - L}{2}. \tag{2.12}$$

Since it is assumed that there is a discrete parity symmetry (P), the gauge coupling constants for the two $SU(2)$ groups will be identical before symmetry breaking:

$$g_2 \equiv g_{2L} \equiv g_{2R} \tag{2.13}$$

The first stage of symmetry breaking proceeds as follows [1] [5]:

$$SU(2)_L \times SU(2)_R \times U(1)_{B-L} \times P \tag{2.14}$$

$$\Downarrow M_P$$

$$SU(2)_L \times SU(2)_R \times U(1)_{B-L} \tag{2.15}$$

At this point, the discrete parity symmetry is already broken, allowing for $g_{2L} \neq g_{2R}$, but the weak gauge symmetry is still unbroken leaving massless $W_R^\pm$ and $W_L^\pm$. To give masses to the gauge bosons and remain still with a massless photon, two more symmetry breaking steps are needed, namely,

$$SU(2)_L \times SU(2)_R \times U(1)_{B-L} \tag{2.16}$$

$$\Downarrow M_{W_R}$$

$$SU(2)_L \times U(1)_{B-L} \tag{2.17}$$

$$\Downarrow M_{W_L}$$

$$U(1)_{em}. \tag{2.18}$$

From the last two steps, we learn that at low enough energies, the effective theory is equivalent to the SM with left-handed weak interactions, and that the suppression of right-handed currents is a result of $SU(2)_R$ symmetry being broken at a higher energy scale (*i.e.* $M_{W_R} > M_{W_L}$).

The minimal set of Higgs multiplets required to break the symmetry down to $U(1)_{em}$ is

$$\Delta_L(1, 0, +2) + \Delta_R(0, 1, +2) \tag{2.19}$$

and

$$\phi\left(\frac{1}{2}, \frac{1}{2}, 0\right). \tag{2.20}$$

If one chooses (using a symmetry transformation), the vacuum expectation values (v.e.v) of $\Delta_{L,R}$ to be:

$$< \Delta_{L,R} > = \left(\begin{array}{cc} 0 & 0 \\ v_{L,R} & 0 \end{array}\right) \tag{2.21}$$

the most general parity and gauge-invariant potential involving $\Delta_{L,R}$ reduces to [1]:

$$V(v_L, v_R) = -\mu^2(v_L^2 + v_R^2) + (\rho_1 + \rho_2)(v_L^4 + v_R^4) + \rho_3 v_L^2 v_R^2, \tag{2.22}$$

where ρ_{1-3} and μ^2 are free parameters. One of the extrema of this potential is for $v_L = 0$ and $v_R \neq 0$. This minimum leaves an unbroken SM, while breaking the $SU(2)_R$ symmetry.

The last step needed to give masses to all the gauge bosons (except for the photon) is to choose the v.e.v for the ϕ fields as:

$$< \phi > = \left(\begin{array}{cc} \kappa & 0 \\ 0 & \kappa' \end{array}\right) e^{i\alpha}. \tag{2.23}$$

2.1.4 Gauge Bosons: Masses, Mixing Angles and Interactions

The eigenstates of the charged gauge boson mass matrix are:

$$W_1 = W_L \cos\xi + W_R \sin\xi, \tag{2.24}$$

$$W_2 = -W_L \sin\xi + W_R \cos\xi, \tag{2.25}$$

with masses [1]:

$$M_{W_1}^2 \simeq \frac{1}{2}g^2(\kappa^2 + \kappa'^2), \tag{2.26}$$

$$M_{W_2}^2 \simeq \frac{1}{2}g^2(\kappa^2 + \kappa'^2 + 2v_R^2). \tag{2.27}$$

and with mixing angle:

$$\tan 2\xi = \frac{2\kappa\kappa'}{v_R^2 - v_L^2}. \tag{2.28}$$

The interaction Lagrangian becomes:

$$L = \frac{g}{\sqrt{2}}(\bar{u}_L\gamma_\mu d_L + \bar{\nu}_L\gamma_\mu e_L)(W_1^{\dagger\mu}\cos\xi + W_2^{\dagger\mu}\sin\xi) \tag{2.29}$$

$$+\frac{g}{\sqrt{2}}(\bar{u}_R\gamma_\mu d_R + \bar{\nu}_R\gamma_\mu e_R)(W_2^{\dagger\mu}\cos\xi - W_1^{\dagger\mu}\sin\xi) + h.c.$$

The weak quark and lepton current can include, as in the SM, mixing angles as well as CP-violating phases.

In the neutral gauge sector, one obtains an extra boson, Z_R. This boson can also mix with the Z_L to produce two mass eigenstates. One can then identify the Z^0 boson with the lower mass eigenstate, which will have a small admixture of Z_R.

2.1.5   Fermions: Masses and Mixing Angles

Fermions acquire masses and mixing angles between them, through their interactions with the Higgs particles, via Yukawa couplings. For the specific choice of Higgs sector (minimal) described above, symmetry considerations constrain the relation between the mixing angle matrix (CKM) of the right- and left-handed quarks. There are two cases:

- *manifest left-right symmetry*

- *pseudo-manifest left-right symmetry*

In the manifest left-right symmetry case, all the elements of the CKM matrix are identical for right-handed and left-handed quarks. In the pseudo-manifest case, the corresponding angles are the same, but their relative phases are different.

In some models with other choices for the Higgs sector (non-minimal), the right-handed CKM matrix elements can be completely arbitary and different from their left-handed counterpart.

2.1.6 Neutrinos: Masses and the connection with LR symmetry

Electrically neutral spin 1/2 fermions are allowed to have two different forms of mass terms in the Lagrangian, as opposed to only one for the charged ones. These are the Dirac and Majorana mass terms:

$$L_D = m_D \bar{\nu}_L \nu_R + h.c. \tag{2.30}$$

and

$$L_M = m_L \nu_L^T C^{-1} \nu_L + m_R \nu_R^T C^{-1} \nu_R, \tag{2.31}$$

where m_D and $m_{L,R}$ are complex numbers, $\nu_{R,L}$ are the respective right- and left-handed projections of the neutrino and C is the charge-conjugation operator. In the SM the ν_R does not exist and therefore the Dirac neutrino gets exactly zero mass (to all orders in perturbation theory). On the other hand, ν_R must exist in LR models, therefore allowing both mass terms.

For one specific symmetry breaking scheme [1] [6] the neutrino mass matrix can be written as:

$$M = \begin{pmatrix} 0 & m_D \\ m_D & m_R \end{pmatrix}. \tag{2.32}$$

The eigenvalues of this matrix are (for $m_R \gg m_D$):

$$m_\nu \simeq -\frac{m_D^2}{m_R} \tag{2.33}$$

and

$$m_N \simeq m_R. \tag{2.34}$$

Since the same symmetry breaking scheme (interaction with the Higgs bosons of the theory) gives masses to the charged and neutral leptons as well as the gauge bosons, the above eigenvalues can be written as a function of the known masses of the charged leptons and the right-handed W boson. For the first family this translates into [1]:

$$m_\nu \simeq \frac{r^2}{\beta} \frac{m_e^2}{m_{W_R}} \tag{2.35}$$

$$m_N \simeq \beta m_{W_R} \tag{2.36}$$

where r and β are free dimensionless parameters.

In this theoretically attractive case there is a connection between N and W_R from the fact that they both acquire the scale of their mass at the same step in the symmetry breaking $(SU(2)_L \times SU(2)_R \times U(1)_{B-L} \Rightarrow SU(2)_L \times U(1))$.

The most interesting feature of these See-Saw [4] type mass relations is that they give a connection between the lightness of the light neutrino and the suppression of right-handed (V+A) currents for large M_{W_R}.

The eigenstates of the neutrino mass matrix in this case are:

$$\nu = \nu_L \cos \zeta + \nu_R \sin \zeta, \qquad (2.37)$$

$$N = -\nu_L \sin \zeta + \nu_R \cos \zeta, \qquad (2.38)$$

with

$$\tan \zeta \approx \sqrt{\frac{m_\nu}{m_N}}. \qquad (2.39)$$

The doublets participating in the charged current will then be:

$$\begin{pmatrix} \nu \cos \zeta + N \sin \zeta \\ e^- \end{pmatrix}_L \text{ and } \begin{pmatrix} -\nu \sin \zeta + N \cos \zeta \\ e^- \end{pmatrix}_R. \qquad (2.40)$$

It is important to notice that the Majorana mass term in the Lagrangian (L_M) breaks the lepton number by two units ($\Delta L = 2$), therefore it allows lepton-number non-conservation. This could materialize in processes such as neutrinoless double beta decay $(\beta\beta)_{0\nu}$, $K^+ \rightarrow \pi^- e^+ e^+$, etc.

The connection between the masses of the neutrinos, their Majorana nature and the suppression of right-handed currents can be also understood from the charge formula:

$$Q = I_{3L} + I_{3R} + \frac{B-L}{2}. \qquad (2.41)$$

If we probe nature with interactions at an energy scale above the left-handed symmetry breaking scale , the $SU(2)_L$ becomes a good symmetry, forcing $\Delta I_{3L} = 0$. In that case, for V+A currents $|\Delta I_{3R}| = 1$ and for purely leptonic processes:

$$|\Delta I_{3R}| = 1 = \frac{1}{2}\Delta L. \qquad (2.42)$$

The Majorana (lepton number violating) mass of the neutrinos is therefore connected to the strength of parity violation.
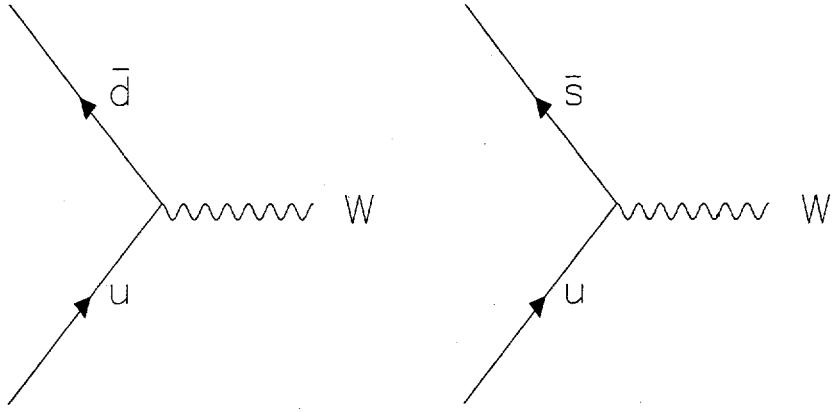
Figure 2.1: The lowest order Drell-Yan W Production Diagrams. These are identical for standard W and W_R production.

2.2 LR Phenomenology at Hadron Colliders

2.2.1 $W_R^{\pm}$ Properties and Production

In $p\bar{p}$ colliders, the mechanism for the production of $W_R^{\pm}$ is the same as for standard W production. At the lowest order, the production takes place through a Drell-Yan process in which a quark (q) and an anti-quark $(\bar{q})$ annihilate to form a W. Figure 2.1 shows the lowest order Drell-Yan W production diagrams (assuming negligible c, b, t contributions to the p momentum) where the charge conjugate of these processes will give W^- production.

The main differences between $W_R^{\pm}$ and the standard $W_L^{\pm}$ production are:

- the spin projection of the leptons and of the W. Only the right-handed helicity quarks participate in the interaction vertex $(V + A)$ and, as a consequence, the longitudinal component of the W_R spin will be in opposite direction to the spin of a standard W produced in a similar reaction. See Fig. 2.2 for a graphic illustration of the spin projections.

- the cross section $(\sigma_{p\bar{p} \to W})$.
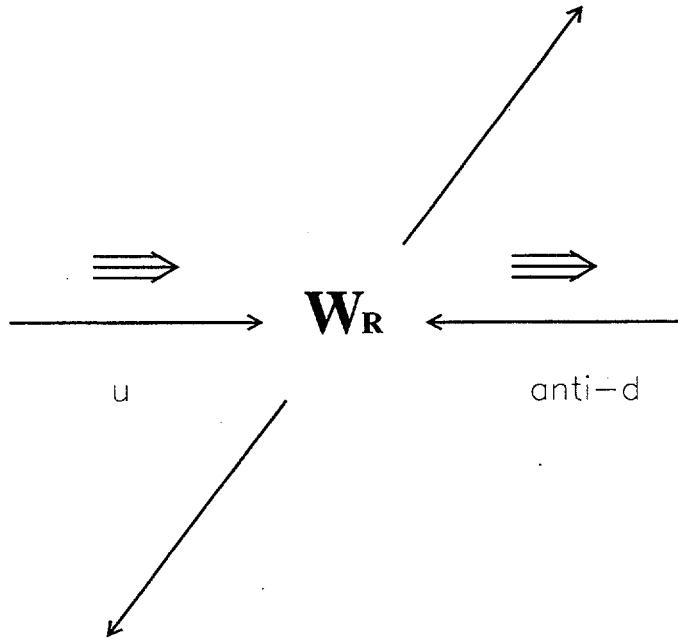
Figure 2.2: Helicity diagram for the production of W_R to lowest order. A right-handed u quark, with its spin projection (thick arrow) in the same direction as the momentum (thin arrow), interacts with a right-handed $\bar{d}$ quark with its spin opposite to the momentum direction.

The difference in the production cross sections is due to:

- possibly different coupling constants: g_L vs. g_R.

- the CKM matrix elements $V_{qq'}^{L,R}$, especially $V_{ud}^{L,R}$. As discussed in Sec. 2.1.5, the CKM matrix elements can be different for the right-handed quarks. Since the u and the d are the quarks that carry most of the proton's momentum, the V_{ud} element is the most important.

- the dependence of the parton-parton cross section on the center of mass energy $(\sqrt{\hat{s}})$ of the process. The parton-parton cross section scales with $\frac{1}{\hat{s}}$. Therefore, a larger
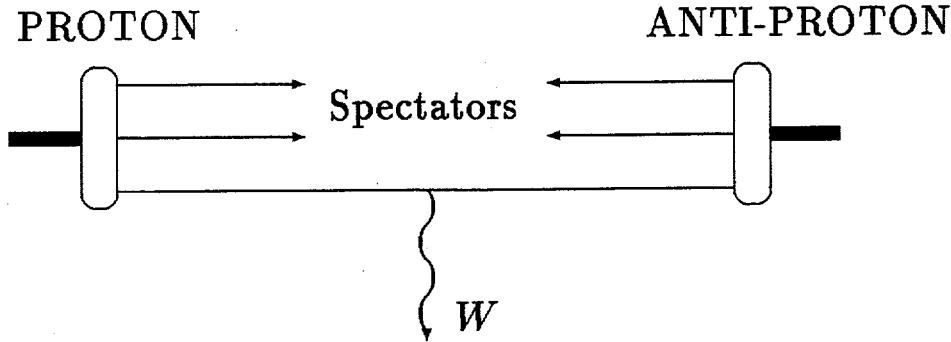
Figure 2.3: Parton Model picture of the production of a W or W_R in a $p\bar{p}$ collision. In the production of W_R the right-handed helicity quarks are the ones that interact in the vertex. The other quarks and gluons in the proton and anti-proton are spectators.

mass object will have a smaller production cross section.

- the falling parton distribution functions (PDF) at higher $\sqrt{\hat{s}}$. Since the W_R is expected to be heavier that the standard W, more energetic and sparse partons are necessary to produce them. This is the main factor that reduces the W_R production w.r.t the standard W_L.

According to the parton model, the quarks and anti-quarks inside the hadrons can be regarded as free particles. This is true for high momentum transfers and it is the result of the so-called asymptotic freedom of Quantum Chromodynamics theory (QCD). The cross section calculation consists of folding the sub-processes' cross sections for Drell-Yan production (using the electro-weak Lagrangian), with the momentum density distribution functions for the partons inside the proton and antiproton. Figure 2.3 shows the parton model picture of the process.

A Drell-Yan process for the production of a vector gauge boson of mass M by colliding hadrons A and B has a cross section per unit rapidity [7]:

$$\frac{d\sigma}{dy}(W^+) = K\frac{\pi g_{L,R}^2}{12M^2}\sum_{q,\bar{q}'}|V_{qq'}^{L,R}|^2 x_a x_b q(x_a, M^2)\bar{q}'(x_b, M^2) \tag{2.43}$$

where x_a (x_b) is the momentum fraction of q ($\bar{q}'$) in hadron A (B) and is evaluated at

$$x_{a,b} = \frac{M}{\sqrt{s}}e^{\pm y}, \tag{2.44}$$

the K-factor includes first order QCD corrections

$$K \simeq 1 + \frac{8\pi}{9}\alpha_s(M^2), \tag{2.45}$$

and q is the parton density at momentum fraction x_a and evaluated at a momentum transfer scale of M^2.

The total cross section for W production is then obtained by integration over the full kinematic range of rapidity:

$$-\ln\frac{\sqrt{s}}{M} \leq y \leq \ln\frac{\sqrt{s}}{M}. \tag{2.46}$$

A more precise calculation includes diagrams of up to order α_s^2 [8]. Figure 2.4 shows the results of such calculation as a function of the mass of the W_R mass using three different sets of parton-density distributions (from oldest to newest): EHLQ [9], HMRSB [10] and MRS(H) [11].

2.2.2 Heavy Majorana Neutrinos: Properties and Decays

The existence of right-handed neutrinos is a direct consequence of LR models as was shown in Sec. 2.1.6. A massive Majorana neutrino fits naturally into these models and leaves a very light left-handed neutrino through a See-Saw-type [6] [4] mechanism. Therefore, it is important to understand the ways in which such a massive Majorana neutrino will decay.

The mixing between the light and heavy neutrino (to form weak interaction eigenstates) is expected to be small [1]: from $\tan\zeta \approx \sqrt{\frac{m_\nu}{m_M}}$ and using the current limit on the mass of the electron neutrino (5.2 eV) [12] [13],

$$\zeta < 7\cdot10^{-4} \tag{2.47}$$

for a $N > 1$ GeV. Therefore we will assume that the neutrinos are not mixed (light and heavy).

The two decay diagrams for massive Majorana neutrinos of this type are shown in Fig. 2.5.
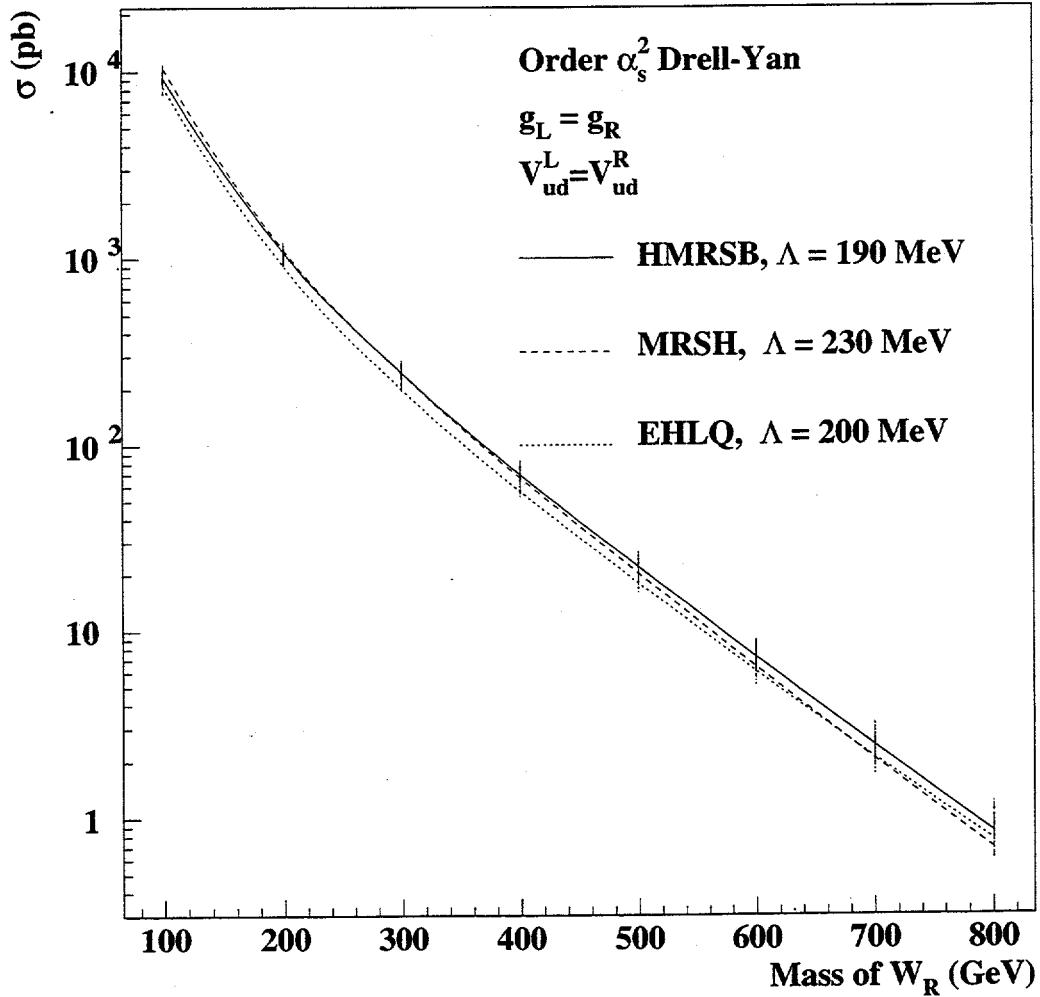
Figure 2.4: The W_R production cross section in $p\bar{p}$ collisions at $s^{1/2} = 1.8$ TeV as a function of the W_R mass. Results from three different PDF sets are shown, the most modern of which is the MRSH set. The apparent small vertical lines are the result of the cross sections using 24 other PDF sets and of varying the number of fermions in the loops allowed in the calculation (4,5,6). In these plots it was assumed that $g_L = g_R$ and that $V_{qq'}^L = V_{qq'}^R$.

The first diagram proceeds through a W_2 boson that is predominantly W_R. For Majorana fields the anti-particle is the same as the particle. Therefore either an electron or a positron can be emitted in the decay (and the charge of the W_2 is fixed by charge conservation). The W_2 is on-shell for $M_N > M_{W_2}$ or off-shell for $M_N < M_{W_2}$. The W_2 boson subsequently decays into any of the open channels:

- $u\bar{d}, c\bar{s}$

- $t\bar{b}$, if M_{W_2}(on or off-shell)$> M_t + M_b$

- lN for e, μ and τ families, if M_{W_2}(on or off-shell)$> M_l + M_N$

The second diagram proceeds through a W_1 boson. For this channel to be open, there must be some mixing between W_L-W_R ($\xi \neq 0$). The W_1 is usually on-shell for $M_N > M_{W_1}$ but must be off-shell for $M_N < M_{W_1}$. The W_1 boson subsequently decays into any of the open channels:

- $u\bar{d}, c\bar{s}$

- $l\nu$ for e, μ and τ families

In this case a light neutrino can appear in the final state since W_1 is predominantly W_L (the SM W).

In general, the two decay channels will contribute with their relative strengths determined by the masses (M_{W_2} and M_N) and the W_L-W_R mixing angle ξ.

The signatures of the possible decays will be discussed in a later section.

2.2.3 $W_R^{\pm}$ Decay Signatures

The right-handed W boson (or more precisely, the W_2 mass eigenstate in the presence of mixing) decays similarly to the SM W boson decay. All the quark channels are open (the charge conjugate of which give W_R^- decays):

$$W_R^+ \rightarrow q\bar{q}' \tag{2.48}$$
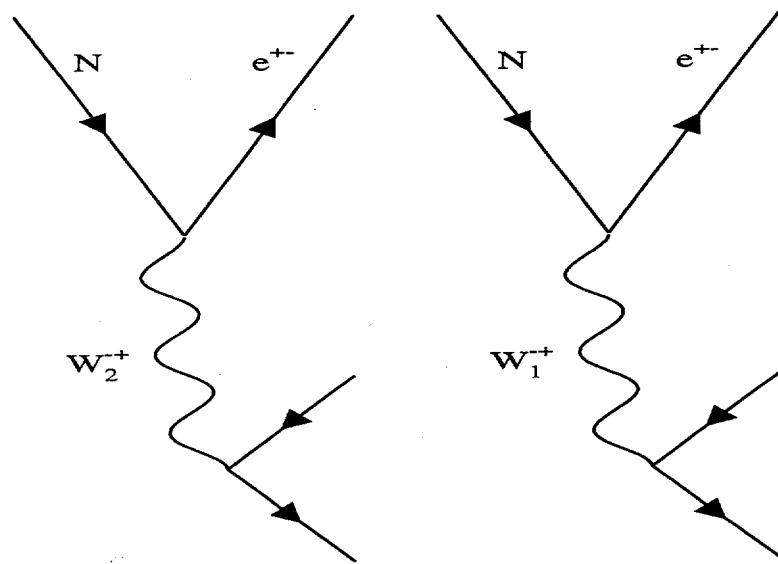
Figure 2.5: Heavy Majorana neutrino decays (electron family). The decay on the left diagram proceeds through a W_2 (predominantly W_R) either on-shell or off-shell depending on the masses. The diagram on the right contributes only in the presence of W_L-W_R mixing. If the mixing is negligible only the first diagram will contribute to the decay. The relative strengths of the two channels depend on the masses (M_{W_2} and M_N) and on the W_L-W_R mixing angle ξ.

where q is a u, c or t quark and $\bar{q}'$ is a $\bar{d}$, $\bar{s}$ or $\bar{b}$ quark. The specific branching ratios into each $q\bar{q}'$ pair depend on the elements of the CKM matrix for the right-handed quarks, $V_{qq'}^R$. The experimental signature for such decays (except for when there is a t quark) is the detection of two hadronic jets of particles (from now on called simply jets). The jets appear as a result of the fragmentation/hadronization of the bare quarks. In this process mesons and baryons that are boosted in the same direction as the parent quark are created. Such a final state will give a peak in the two-jet invariant mass spectrum with a mean of M_{W_R} and whose width is determined by the hadronic energy resolution and the natural width of the boson, Γ_{W_R}. In hadron colliders this signal has to be distinguished from a large background of two-jet events from QCD processes.

In the decays in which there is a t quark in the final state, additional jets or leptons (including normal escaping neutrinos ν) will result from the subsequent t quark decay. Such decays can be mimicked by standard W production in conjunction with jets.

The leptonic channels:

$$W_R \rightarrow lN, \tag{2.49}$$

where N is a generic right-handed neutrino (of any nature and family), will be open if $M_N < M_{W_R}$. Their branching ratio will depend on:

- the ratio of the masses $\frac{M_N}{M_{W_R}}$

- how many heavy neutrinos N_i ($i=e,\mu$ or τ) have $M_N < M_{W_R}$

- the ratio of the masses $\frac{M_{top}}{M_{W_R}}$

For simplicity, we will assume here that the right-handed neutrinos from the three families have the same mass. In that case the branching ratio into, say, l_iN_i will be [7]:

$$BR(W_R \rightarrow l_iN_i) = \frac{b_m(M_N/M_{W_R})}{3 + 3 + 3b_m(M_{top}/M_{W_R}) + 3b_m(M_N/M_{W_R})} \tag{2.50}$$

where $b_m(x) = (1 - x^2)(1 - \frac{1}{2}x^2 - \frac{1}{2}x^4)$. Figure 2.6 shows the contours of same expected branching ratios for this process as a function of the W_R and N mass. Figure 2.7 shows the same branching ratio as a function of the ratio M_N/M_{W_R} and its dependence on the mass of the top quark.
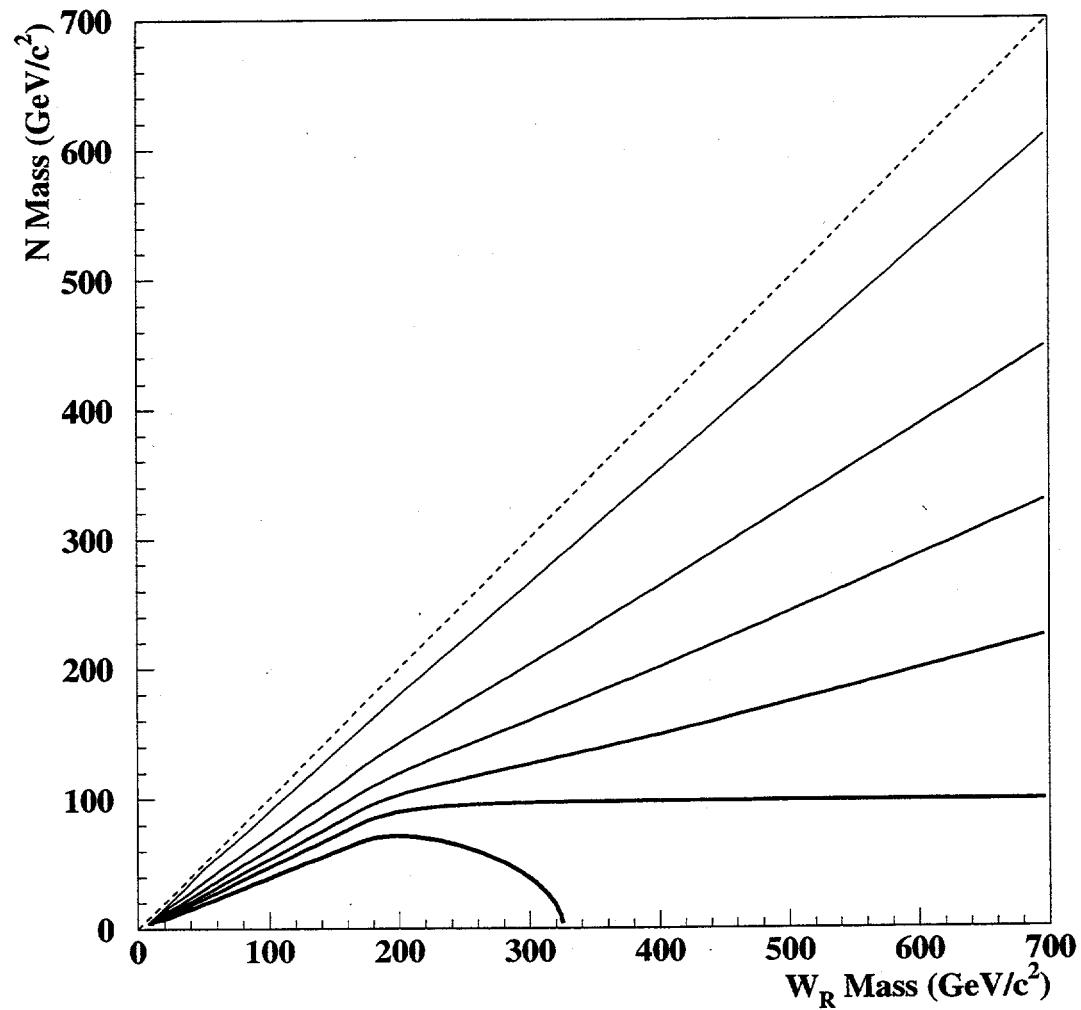
Figure 2.6: The contours of same branching ratios for the $W_R \rightarrow eN$ decay. From bottom to top, the lines represent the 110, 100, 90, 75, 50 and 10 percent of the naive $\frac{1}{12}$ value.
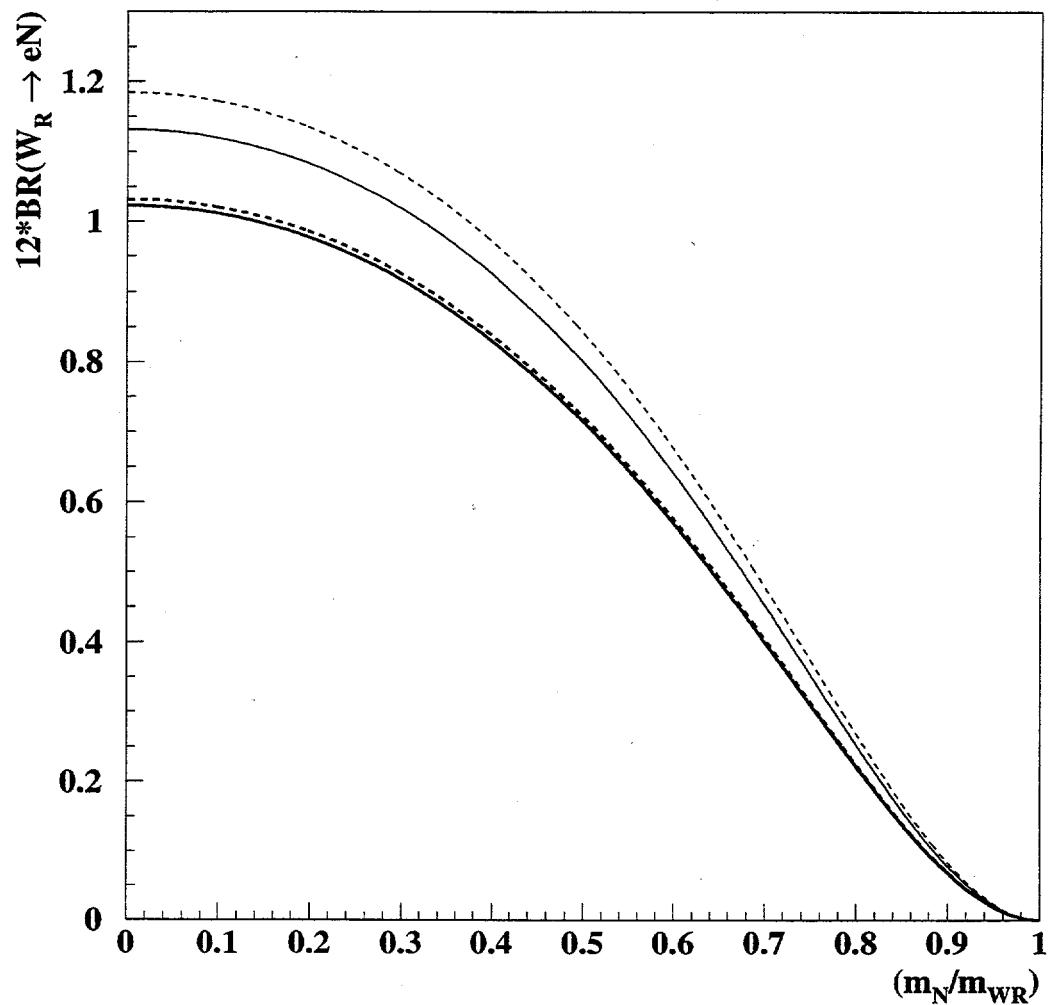
Figure 2.7: The branching ratios for the $W_R \rightarrow eN$ decay times 12. From bottom to top, the lines represent the branching ratio for different values of M_{W_R} and the top quark mass M_t: (700,170),(700,200),(300,170),(300,200). It is assumed that all the massive neutrinos have the same mass.

If the right-handed neutrino escapes undetected, it will lead to a transverse energy imbalance, $\not{E}_T$. Events with such decays have the distinct characteristic of having a high transverse momentum (p_T) lepton and large $\not{E}_T$. On the other hand, if the right-handed neutrinos are massive they could decay inside the detector. In that case the decay will not necessarily lead to large $\not{E}_T$. Since this decay chain is the subject of this dissertation, more details about it are presented in what follows.

The production and decay chain under study is [14] [15] [16] [17] [18]:

$$\bar{p}p \rightarrow W_R^{\pm} \rightarrow e^{\pm}N. \tag{2.51}$$

The first and trivial condition for this to happen is that $M_N < M_{W_R}$. In the presence of mixing the two diagrams in Fig. 2.5 will contribute to the N decay. If the massive neutrino is much lighter than 80 GeV ($M_N < M_{W_1}$), the decay width into the eW_1(off-shell) mode is:

$$\Gamma(N \rightarrow eW_1) = 9\xi^2 G_F^2 \frac{M_N^5}{192\pi^3} \tag{2.52}$$

where ξ is the W_L-W_R mixing angle and the factor of 9 reflects the number of channels open for the W_1 decays ($3u\bar{d}$, $3c\bar{d}$, $e\nu$, $\mu\nu$ and $\tau\nu$). If the massive neutrino is heavier than 80 GeV ($M_N > M_{W_1}$), the decay width into the eW_1(on-shell) mode is [7]:

$$\Gamma(N \rightarrow eW_1) = G_F \frac{M_N^3}{8\pi\sqrt{2}}\xi^2(1 - \frac{M_{W_1}^2}{M_N^2})^2(1 + \frac{2M_{W_1}^2}{M_N^2}). \tag{2.53}$$

On the other hand, the W_2 mode is always off-shell if the N was produced in $W_R^{\pm} \rightarrow e^{\pm}N$, and therefore the decay width for this decay is:

$$\Gamma(N \rightarrow eW_2) = f_c(G_F^R)^2 \frac{M_N^5}{192\pi^3}. \tag{2.54}$$

f_c=6 if $N < M_{top}$ and 9 otherwise, because the leptonic channels are closed (assuming that the three N's have the same mass), and $G_F^R = G_F \frac{M_{W_1}^2}{M_{W_2}^2}$ to reflect the mass of the boson participating in the decay.

All the above decay widths are increased by an extra factor of two if the right-handed neutrinos are Majorana particles. The reason is that Majorana particles are their own anti-particle and thus the charge-conjugate of any of the decays is also allowed and has the same strength.

Figure 2.8 shows the region of the parameter space (M_N and M_{W_R}) for which the N decay is expected to go predominantly through the W_2 diagram (shown in Fig. 2.5) for different values of the mixing angle. For $\xi < 0.001$ the non-mixed decays are expected to dominate over most of the parameter space under study.

2.3   This Search: Experimental Signatures

We search for right-handed W bosons in the production/decay chain:

$$\overline{p}p \rightarrow W_R^\pm \rightarrow e_1^\pm N \tag{2.55}$$

with the subsequent heavy neutrino decay:

$$N \rightarrow e_2^\pm jj. \tag{2.56}$$

The decay signature is the presence of two electrons and two additional jets. The invariant mass of the two electrons and the two jets gives the mass of the W_R. The invariant mass of one of the electrons with the two jets gives the mass of N. In addition, if the decay occured through mixing and $N > 80$ GeV, the invariant mass of the two jets is approximately 80 GeV. For $N > 80$ GeV the invariant mass of the two jets is 80 GeV, if the decay proceeded through mixing.

There are also topological signatures that can be exploited to infer the presence of such decay. One example of these is the transverse momentum distribution of the first electron, e_1. This electron is the product of the two body decay of the W_R and, in the center of mass frame of the W_R, it is monoenergetic (neglecting intrinsic width effects) with

$$E_{CM}^{e_1} = \frac{M_{W_R}^2 - M_N^2}{2M_{W_R}}, \tag{2.57}$$

therefore its p_T distribution will have a Jacobian peak

$$\frac{d\sigma}{dp_T} \propto \frac{2p_T(1 - 2p_T^2/s)}{s\sqrt{(1 - 4p_T^2/s)}} \tag{2.58}$$

where $s = (2E_{CM}^{e_1})^2$. Figure 2.9 shows the transverse momentum distribution of the first electron for different values of M_{W_R} and M_N.
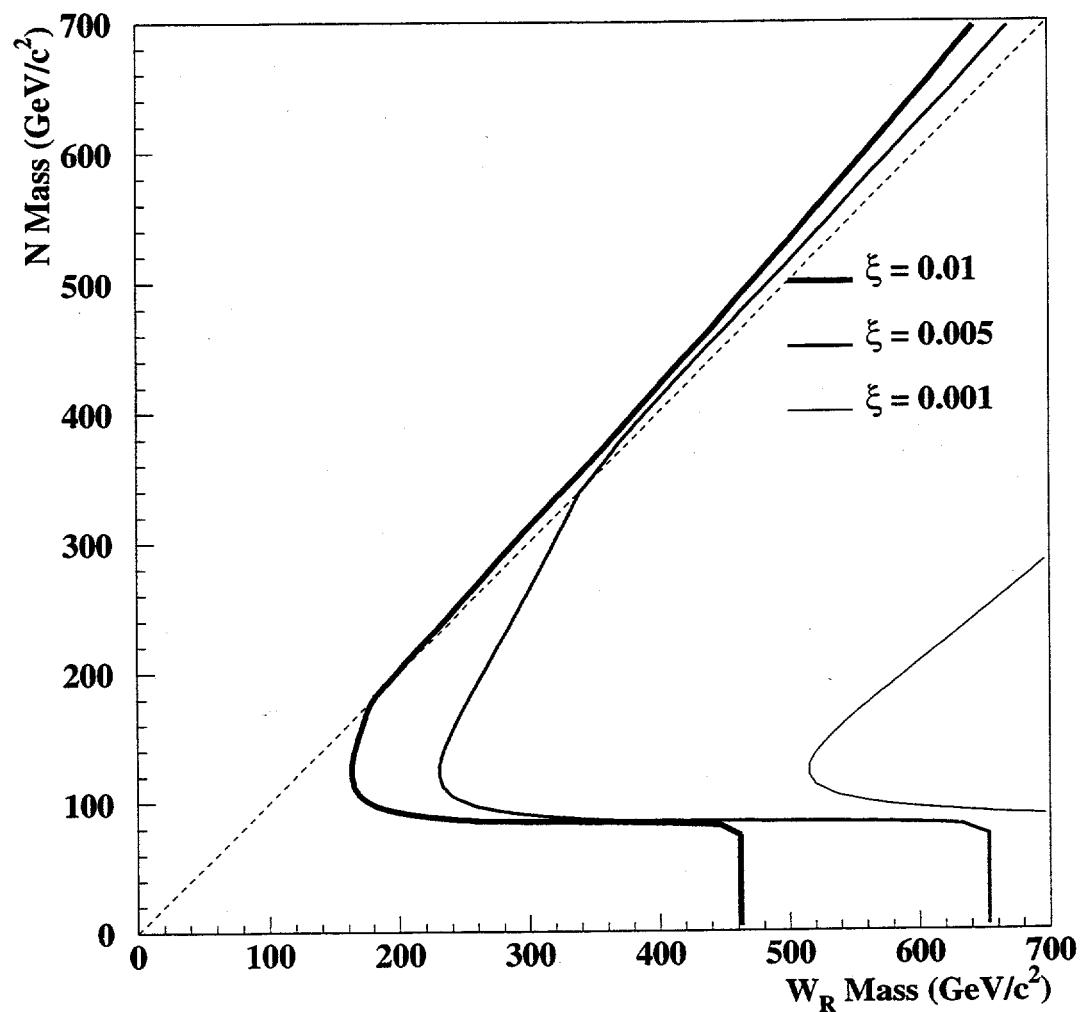
Figure 2.8: For each given W_L-W_R mixing angle ξ, the region on the left is dominated (more than 90%) by non-mixed N decays. $\xi < 0.013$ is the most general limit on the angle, but there are more stringent ones ($\xi < 0.0025$). For $\xi < 0.001$ most of the N decays will be non-mixed. Only the area under the 45° line is relevant to this analysis.
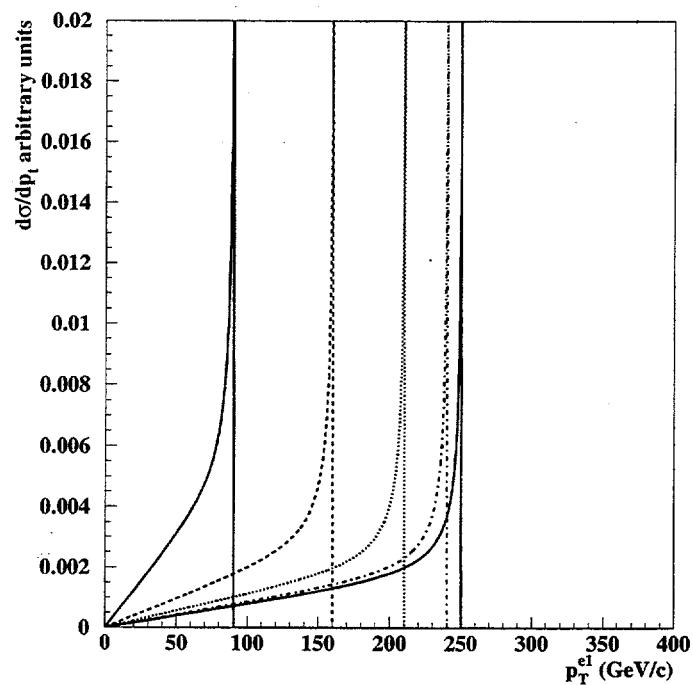
Figure 2.9: Transverse momentum of the electron in unpolarized $W_R \to eN$. The Jacobian peak of this distribution is shown for $M_{W_R} = 500$ GeV with different values of M_N. From left to right, $M_N = 400, 300, 200, 100$ and 0 GeV. The relative normalizations are arbitrary. The effects of the intrinsic width of the W_R and its transverse motion are not included.

2.4 Existing Limits on LR Model Parameters

Since LR models were first proposed, much theoretical and experimental work has been done to constrain its parameters. The experimental constraints can be divided into two large groups: limits from low energy experiments and limits from collider experiments.

In the presence of right-handed currents (V+A terms in the Lagrangian), the effective theory at low energy will show deviations from the SM expected behavior, even if the scale for those currents is much larger than the V-A scale. The limits from low energy experiments are based on searches for such small deviations.

On the other hand, in collider experiments the goal is to directly produce the new particles ($W_R^\pm$ and Z_R) and observe them through their distinct decays. Limits of this type are normally less model-dependent.

The two basic parameters that one wishes to constrain are:

- the masses of the new gauge bosons: $M_{W_R^\pm}$ and M_{Z_R} and

- the mixing angle between the W_L and W_R and the corresponding angle for the $Z_{L,R}$ bosons.

The limits on the above quantities depend on:

- the value of the coupling constant, g_R,

- the value of the CKM matrix elements for the right-handed quarks, $V_{qq'}^R$ and

- the mass and nature (Dirac or Majorana) of the right-handed neutrinos.

2.4.1 Limits from Low Energy Experiments

The most important low energy limits are listed in Table 2.1 [19]:

1. If the right-handed neutrinos are light (< 1-10 MeV), there are very stringent limits from nucleosynthesis and from Supernova 1987A [20].

2. If the right-handed neutrinos are light enough to be produced without kinematic suppression in μ decay (< 6 MeV), there are limits [21] from the non-observation of

deviations from the V-A predictions. In this case the limit on the M_{W_R} and the angle ξ are correlated (μ decay).

3. In the K^0-$\bar{K}^0$ system, the mass difference Δm_K can get additional contributions from new diagrams with W_R exchange. These limits [22] [13] are very stringent for $V_{qq'}^R = V_{qq'}^L$, but get diluted for other values. On the other hand, they do not depend at all on the mass or nature of the right-handed neutrinos (Δm_K).

4. If the right-handed neutrinos are relatively heavy ($> m_b - m_c = 3.5$ GeV), the right-handed currents do not contribute to the leptonic or semileptonic decays of the b and c quarks [23]. However, the non-leptonic decay channels will be open, leading to deviations of the semileptonic branching ratios from the SM values (referred as b in Table 2.1).

5. For some (restricted) choices of $V_{qq'}^R$, there are stringent limits on M_{W_R} from $B_d\bar{B}_d$ mixing [24] ($B_d\bar{B}_d$).

6. If the right-handed neutrinos are heavy and of Majorana type, they can contribute to diagrams for neutrinoless double beta decay. From the limits [25] [13] on the lifetime of these decays in nuclei, correlated limits for M_{W_R} and M_N are obtained ($\beta\beta_{0\nu}$).

In order to quantify the change in the limits due to the different values of the CKM matrix for the right-handed quarks ($V_{qq'}^R$), five different matrices are used:

$$V_{(I)}^R = \begin{pmatrix} 1 & 0 & 0 \\ 0 & 1 & 0 \\ 0 & 0 & 1 \end{pmatrix} \quad V_{(II)}^R = \begin{pmatrix} 1 & 0 & 0 \\ 0 & 0 & 1 \\ 0 & 1 & 0 \end{pmatrix} \quad V_{(III)}^R = \begin{pmatrix} 0 & 1 & 0 \\ 1 & 0 & 0 \\ 0 & 0 & 1 \end{pmatrix} \tag{2.59}$$

$$V_{(IV)}^R = \begin{pmatrix} 0 & 1 & 0 \\ 0 & 0 & 1 \\ 1 & 0 & 0 \end{pmatrix} \qquad |V_{(LR)}^R| = |V^L| \tag{2.60}$$

Table 2.1 shows the limits [19] on $M_{2g} = \frac{g_L}{g_R}M_{W_2}$ for the different right-handed neutrino assumptions and for the five V^R matrices.
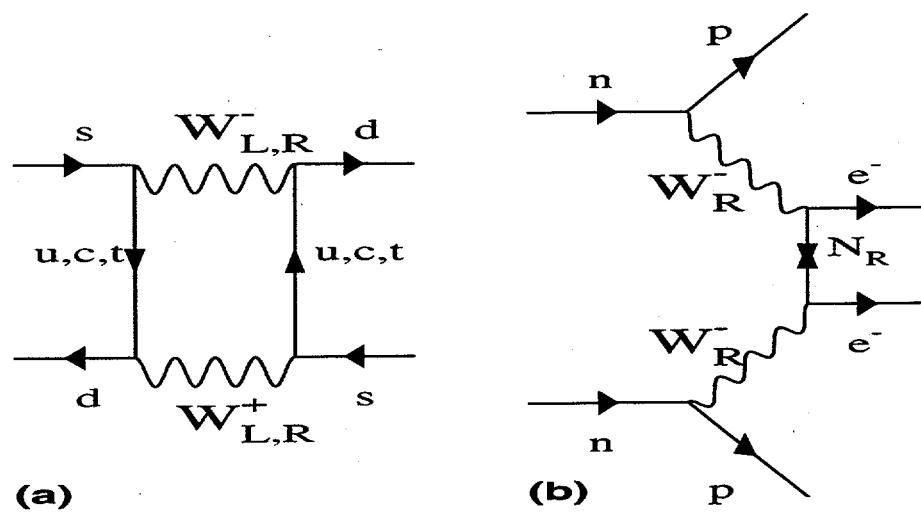
Figure 2.10: (a) New diagrams that contribute to Δm_K from K^0-$\bar{K}^0$ mixing with W_R exchange. Limits from this system do not depend on the mass or nature of the right-handed neutrino. (b) Diagram for $\beta\beta_{0\nu}$ in the presence of heavy Majorana neutrinos. This decay does not conserve lepton number.

Neutrino case Limit method	V^R case	M_{2g} Limit (GeV/c^2)
Heavy Majorana $\Delta M_K + B_d \bar{B}_d + b + \beta\beta_{0\nu}$	$V^R_{(I)}$	810
	$V^R_{(II)}$	800
	$V^R_{(III)}$	670
	$V^R_{(IV)}$	1300
	$V^R_{(LR)}$	1400
Heavy Dirac $\Delta M_K + B_d \bar{B}_d + b$	$V^R_{(I)}$	300
	$V^R_{(II)}$	460
	$V^R_{(III)}$	670
	$V^R_{(IV)}$	1300
	$V^R_{(LR)}$	1400
Intermediate mass $\Delta M_K + B_d \bar{B}_d + \mu$ decay	$V^R_{(I)}$	500
	$V^R_{(II)}$	500
	$V^R_{(III)}$	560
	$V^R_{(IV)}$	1300
	$V^R_{(LR)}$	1300
Light ($m_{\nu_{1R}} < 10$ MeV) Supernova 1987A	$V^R_{(III)}, V^R_{(IV)}$	720
	$V^R_{(I)}, V^R_{(II)}, V^R_{(LR)}$	16 TeV
Light ($m_{\nu_{iR}} < 1$ MeV) Nucleosynthesis	any	$O(1$ TeV$)$

Table 2.1: Limits on $M_{2g} = \frac{g_L}{g_R} M_{W_2}$ from low energy experiments [19]. Results are shown for the different assumptions about the neutrino's nature and mass and for different values of the CKM matrix for right-handed quarks. References for the experiments and for the review article summarizing them are given in the text.

2.4.2 Limits from Collider Experiments

There have been, so far, two types of direct searches for W_R at colliders. The first one looks for $p\bar{p} \rightarrow W_R \rightarrow l\nu_{lR}$, for $l = e$ or μ with the neutrino escaping detection. From such a searches using 1992-93 data, the CDF collaboration obtains [26]:

$$M_{W_R} > 652 \text{ GeV} \tag{2.61}$$

and the DØ collaboration finds [27]:

$$M_{W_R} > 610 \text{ GeV}. \tag{2.62}$$

These limits, however, do not necessarily apply for right-handed W bosons if the right-handed neutrinos are massive and decay inside the detector leaving no $\not{E}_T$. This dependence on the nature and decay of the right-handed neutrinos is avoided in searches for $p\bar{p} \rightarrow W_R \rightarrow q\bar{q}'$. From the UA2 dijet invariant mass spectrum a limit [28] of:

$$M_{W_R} < 101 \text{ GeV or } M_{W_R} > 261 \text{ GeV} \tag{2.63}$$

was obtained at the 90% confidence level, assuming $g_L = g_R$ and that the $t\bar{b}$ and leptonic channels are closed. A recent similar search by CDF [29] constrained the W_R to have:

$$M_{W_R} < 380 \text{ GeV or } M_{W_R} > 470 \text{ GeV} \tag{2.64}$$

All the limits quoted in this section assume that the quark mixing matrix for the right-handed quarks is identical to the known CKM matrix ($V_{qq'}^R = V_{qq'}^L$). For other values of $V_{qq'}^R$ these existing limits become, in general, less restrictive.

The previous collider searches described in this section do not distinguish between the helicities of the gauge boson or the final state particles. Therefore, the limits derived from them apply also to a heavy left-handed W boson (W_L').

To date, no direct searches have been reported for W_R decaying leptonically with the daughter right-handed neutrino allowed to decay inside the detector. That is the subject of this dissertation.

Chapter 3

Tevatron and the DØ Detector

3.1 The Tevatron

The Tevatron (schematically shown in Fig. 3.1) is the last of a chain of accelerators that take protons from hydrogen gas atoms and accelerate them up to 900 GeV. In the process of accelerating the protons, anti-protons are created by dumping 120 GeV protons on a target. From the strong interactions between the target and the energetic protons, many new particles are created, from which the anti-protons are extracted to form the second beam. To reduce the momentum spread (longitudinal and transverse) of the anti-protons collected from the production target, this beam is stochastically cooled [30]. This process uses a pickup coil in one section of the orbit to sense the average deviation of the particles from the ideal orbit. Correction signals are then sent across a chord to a kicker, in time to deflect them towards the ideal trajectory. After being cooled the anti-protons are stored in a storage ring or Accumulator. When about 4×10^{11} antiprotons have been accumulated, the antiprotons are transfered to the Main Ring, where they get accelerated up to 120 GeV (the same as the protons but in the opposite direction). The last step is the acceleration in the Tevatron where both protons and antiprotons reach 900 GeV. The Tevatron uses superconducting magnets that produce the intense magnetic fields necessary to keep 900 GeV protons and antiprotons in a 1 km radius orbit.

The particles are formed into six proton and six antiproton bunches. The two beams are
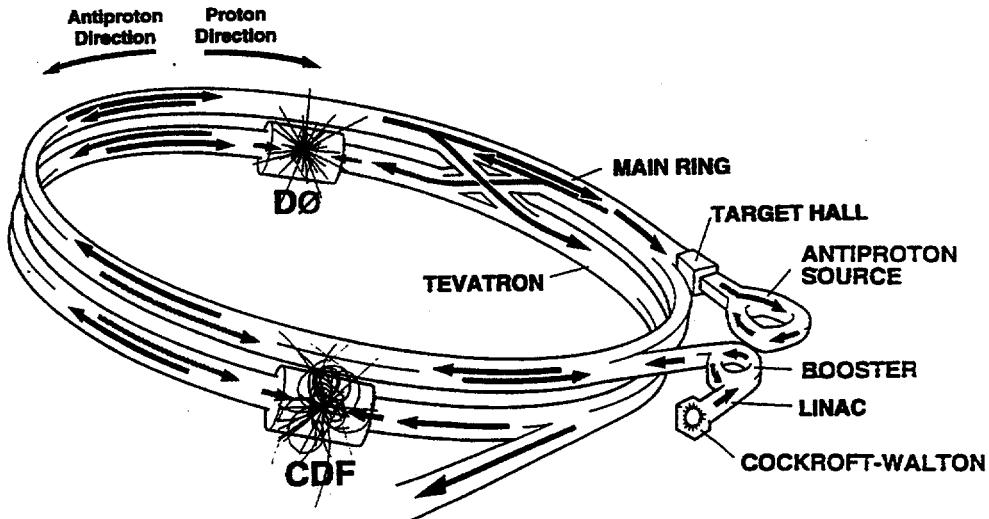
Figure 3.1: Schematic layout of the Tevatron accelerator.

parallel to each other and travel in opposite directions meeting in two points: BØ (where the CDF detector is located) and DØ. The resulting collisions are then at a center of mass energy of $\sqrt{s} = 1.8$ TeV. The typical luminosities achieved during the first DØ collider run (Run Ia), which lasted from April 1992 until May 1993, were around 5×10^{30} sec^{-1} cm^{-2}, and for the second run (Run Ib), which lasted between November 1993 and August 1995, the maximum luminosity exceeded 20×10^{30} sec^{-1} cm^{-2}. A comprehensive review of the technical aspects and mode of operations of the Tevatron is given in Ref. [31].

3.2 The DØ Detector

The DØ Detector (shown in Fig. 3.2) has three main components. Closest to the interaction point are the tracking chambers used for charged particle tracking and for the determination of the position of the interaction vertex. Immediately outside of the tracking chambers is the calorimeter, used for the measurement of the energies of the particles and jets of particles. Last are the muon chambers used for muon identification and measurement. A complete description of the detector, from which most of the information in the

following sections was obtained, can be found in Ref. [32] and references therein.

In its present state, the DØ detector does not have a central magnetic field. For this reason only a small tracking system is necessary (charged particle tracks are straight lines). In turn, the calorimeter could be made compact and almost hermetic.

The detector was optimized with the following three general goals in mind:

- Excellent electron and muon identification and measurement.

- Good measurement of jets at large p_T.

- Good measurement of the E_T imbalance for the inference of the presence of neutrinos or other weakly interacting particles.

A right-handed coordinate system is defined with the z-axis along the direction of the proton beam and with a vertical y-axis. The polar coordinate system is also used (mainly for physics objects) with the azimuthal angle ϕ in the x-y plane ($\phi = 0$ is the x-axis) and the polar angle θ measured relative to the z axis. For most purposes, the pseudorapidity:

$$\eta \equiv -\ln(\tan\frac{\theta}{2}) = \tanh^{-1}(\cos\theta) \tag{3.1}$$

is used instead of the polar angle.

3.3 Calorimeter

The function of the calorimeter is to provide excellent energy measurement for electrons, photons and hadrons. In addition to the energy, the calorimeter provides information useful for particle identification which is essential in a non-magnetic detector.

The DØ calorimeter is a sampling device, in which absorber plates of a large-Z material are interspersed with gaps of liquid argon. Electrons, photons and hadrons shower in the absorber plates according to the relative probabilities as determined from the radiation length X_0 (for electrons and photons) and the interaction length λ (for hadrons). The number of particles in the shower, as determined by the ionization in the liquid-argon gaps, provides a measure of the total energy of the shower.
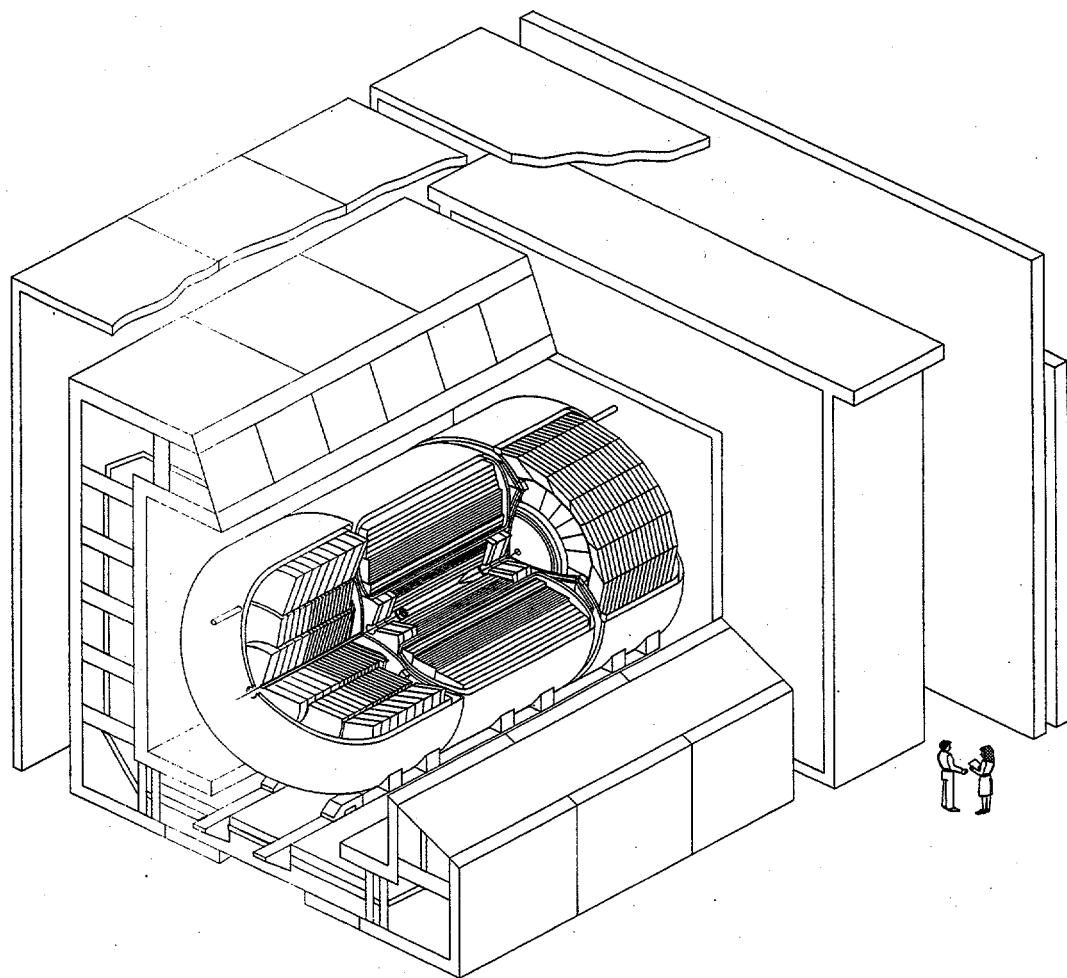
DØ Detector

Figure 3.2: Isometric view of the DØ detector.

D∅ LIQUID ARGON CALORIMETER
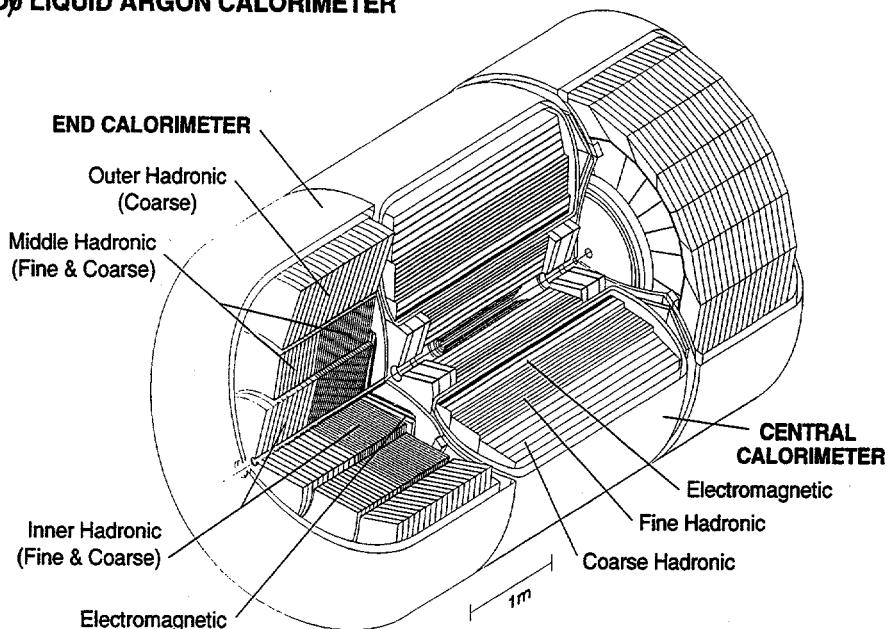
Figure 3.3: D∅ calorimeter.

The interaction length λ is typically much larger than the radiation length X_0 for most heavy materials, particularly uranium (the material used in the inner sections of the calorimeter). Therefore, electrons and photons deposit their energy in the first layers of the calorimeter (hence called the electromagnetic calorimeter), while the hadrons deposit their energy preferentially in the outer layers (called the hadronic calorimeter).

The D∅ Calorimeter consists of the Central Calorimeter (CC) and two identical End Calorimeters (EC) (See Fig. 3.3). Each of the three calorimeters is surrounded by a cryostat, in order to keep the argon in the liquid state, and is subdivided into three modules: the electromagnetic (EM) part, and the fine hadronic (FH) and coarse hadronic (CH) parts.

The gaps between absorber plates are filled with liquid argon. The readout boards are located in the middle of the gaps (see Fig. 3.4). They consist of copper readout pads sandwiched between two G10 plastic plates coated with a resistive epoxy. The absorber plates are grounded while the resistive coat is held at 2.0 kV. Free charges from the ionization in the liquid argon gap drift toward the anode and induce a charge on the copper readout
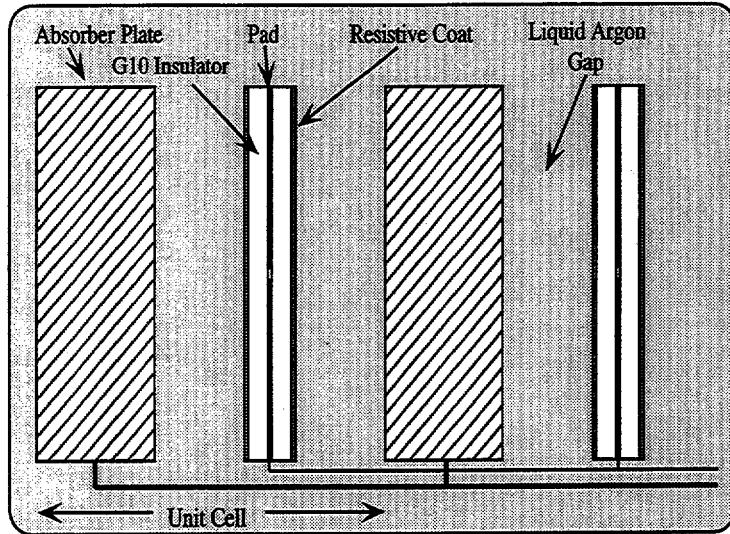
Figure 3.4: Schematic of a DØ calorimeter cell.

pads via capacitive coupling.

Since there is no charge gain in the liquid argon, several pads are ganged together in depth to form a readout cell. This produces a measurable signal even for a single minimum ionizing particle traversing the calorimeter (such as a muon). The analog signals thus obtained are then used for the fast hardware trigger decisions. The signals are also properly shaped, digitized in 12-bit analog-to-digital converters and fed into the data acquisition system.

The EM part of the calorimeter is subdivided into four layers of cells: EM1 through EM4. The transverse size of the cells is $\Delta\eta \times \Delta\phi = 0.1 \times 0.1$ for most layers (approximately 10×10 cm in the CC). In EM3, the cell size is $\Delta\eta \times \Delta\phi = 0.05 \times 0.05$ to provide more transverse shower shape information at the depth where electromagnetic showers are most developed. Layers of EM, FH and CH cells are grouped together to form pseudo-projective towers defined from the nominal interaction vertex point (see Fig. 3.5).

The energy resolution of the DØ Calorimeter can be parametrized in the following form:

$$\left(\frac{\sigma_E}{E}\right)^2 = C^2 + \frac{S^2}{E} + \frac{N^2}{E^2}, \tag{3.2}$$

where C, S and N are contants that correspond to the calibration error, the sampling fluctuations and the noise, respectively. These constants were measured using a test beam of electrons and pions of various energies. For electrons, the resolution is [32]:

$$\left(\frac{\sigma_E}{E}\right)^2 = (0.003 \pm 0.002)^2 + \frac{(0.157 \pm 0.005)^2}{E}, \tag{3.3}$$

and for pions:

$$\left(\frac{\sigma_E}{E}\right)^2 = (0.032 \pm 0.004)^2 + \frac{(0.41 \pm 0.04)^2}{E}, \tag{3.4}$$

where E is the energy in GeV. The noise term is small (~ 100 MeV per readout tower). The azimuthal position resolution of the EM calorimeter (measured with electrons from the collider data) is ≈ 2.5 mm.

The resolution on the missing transverse energy measurement ($\not{E}_T$) is determined primarily by the hadronic energy resolution. This was measured [33] and parameterized as a function of the scalar sum of the transverse energy energy (S_T):

$$\sigma(\not{E}_T) = (1.89 \pm 0.05)GeV + (6.7 \pm 0.7) \cdot 10^{-3} S_T + (9.9 \pm 2.1) \cdot 10^{-6} S_T^2/GeV. \tag{3.5}$$

3.3.1 Central Calorimeter (CC)

The Central Calorimeter (see Fig. 3.3) consists of three concentric rings: an inner ring (EM) with 32 independent modules, and an intermediate and an outer rings (FH and CH) with 16 modules each. The total length of the CC is 2.6 m, and it covers the pseudorapidity range $|\eta| < 1.2$. Additional parameters of the CC are shown in Table 3.1.

3.3.2 End Calorimeters (EC)

The End Calorimeters (see Fig. 3.3) consist of an electromagnetic module (ECEM), an inner fine hadronic module (IFH), and an inner coarse hadronic module (ICH) in the region closest to the beam (small inner radii). In addition, there are two concentric rings at intermediate and large radii. The intermediate ring has a fine hadronic (MCF) and a coarse hadronic (MCH) part, while the outer ring has only a coarse hadronic section (OCH). The ECEM and the IFH modules are built as single modules, while the other sections are
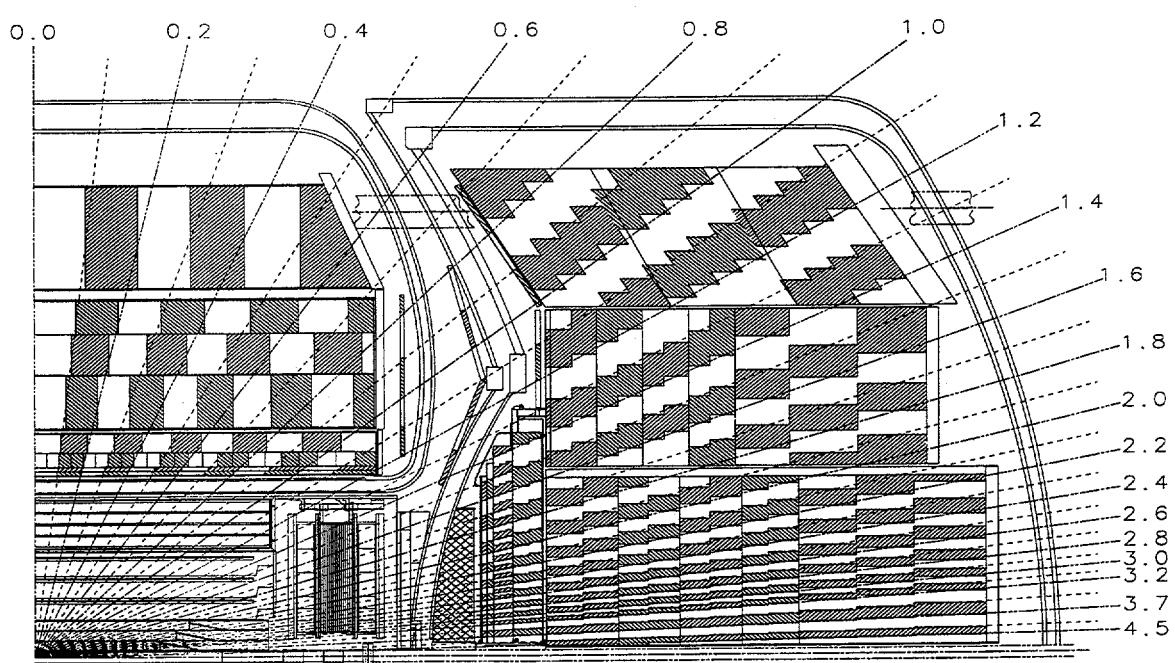
Figure 3.5: A schematic view of a portion of the DØ calorimeter showing the transverse and longitudinal segmentation pattern.

	CCEM	CCFH	CCCH
Absorber	U	U-Nb	Cu
Absorber thickness (mm)	3	6	46.5
Argon gap (mm)	2.3	2.3	2.3
Longitudinal depth ($\perp$)	20.5 $X_0 = 0.76\ \lambda$	3.2 λ	3.2 λ
Number of readout layers	4	3	1
Cells per readout layer	2/2/7/10	20/16/14	9
Depth per readout layer	2/2/6.8/9.8 X_0	1.3/1.0/0.9 λ	3.2 λ
Total number of channels	10,368	3,000	1,224

Table 3.1: Central Calorimeter parameters.

	ECEM	IFH	ICH	MFH	MCH	OCH
Absorber	U	U-Nb	SS	U-Nb	SS	SS
Absorber thickness (mm)	4	6	46.5	6	46.5	46.5
Argon gap (mm)	2.3	2.1	2.1	2.2	2.2	2.2
Longitudinal depth ($\perp$)	20.1 X_0 0.95 λ	4.4 λ	4.1 λ	3.6 λ	4.4 λ	4.4 λ
Number of readout layers	4	4	1	4	1	3
Cells per readout layer	2/2/6/8	16	14	15	12	8
Total number of channels	7,488	4,228	928	1,472	384 + 64 + 896	

Table 3.2: End Calorimeters parameters.

composed of 16 modules. The inner and outer radii of the ECEM module are 5.7 cm and 104 cm, respectively.

As for the CC, most of the readout cells are 0.1 $\times$ 0.1 in (η, ϕ), with two exceptions: the third layer of the ECEM (EM shower maximum) has 0.05 $\times$ 0.05 segmentation and the cells in the most forward region ($|\eta| > 3.2$) have (a factor of two to four) larger cells.

The entire EC covers the pseudorapidity range 1.1 $< |\eta| <$ 4.5. Additional parameters of the EC are shown in Table 3.2.

3.3.3 Intercryostat detectors and Massless Gaps

The region $0.8 < |\eta| < 1.4$ (see Fig. 3.5) contains a large amount of uninstrumented material, such as cryostat walls and mechanical structure materials. In order to correct for energy deposited in these regions, two scintillator counter arrays (Intercryostat Detectors) are mounted on the front surface of the ECs. The light produced in the scintillators is collected by bundles of wavelength-shifter scintillating fibers and readout by 1.3 cm radius photomultipliers. In addition, separate single-cell structures called massless gaps are installed close to the end plates of the CC and the front plates of the EC.

The segmentation and the projective geometry of these additional detection cells is the same as for the CC and EC calorimeters. The main purpose of these detectors is to estimate the amount of energy lost in the uninstrumented material. However, the Intercryostat and Massless Gap detectors do not provide a good measurement of electromagnetic showers, and therefore the electron and photon identification is not effective in the $1.2 < |\eta| < 1.4$ region, where the electromagnetic coverage of the CC and EC is incomplete.

3.4   Central Detectors

The function of the Central Detectors (CD) is to measure charged tracks originating from the proton-antiproton collisions. Because there is no central magnetic field, the tracks left by passing particles are straight and therefore relatively simple to reconstruct. Functionally, good track finding and measurement helps to distinguish photons from electrons. In addition, the dE/dx measurement helps to distinguish between single minimum ionizing particles and multiple minimum ionizing particles (such as in photon conversions). The tracks found in the CD are used to determine the position along the z axis of the primary interaction.

The CD is comprised of three conventional drift chambers and a transition radiation detector (see Fig. 3.6) and is contained in the cylindrical space ($r = 78$ cm, $z = \pm 135$ cm) bounded by the calorimeter cryostats. The Vertex Chamber (VTX) is the innermost tracking device, while the Central Drift Chamber and Forward Drift Chamber provide tracking information in the intermediate region between the VTX and the calorimeter cryostats for
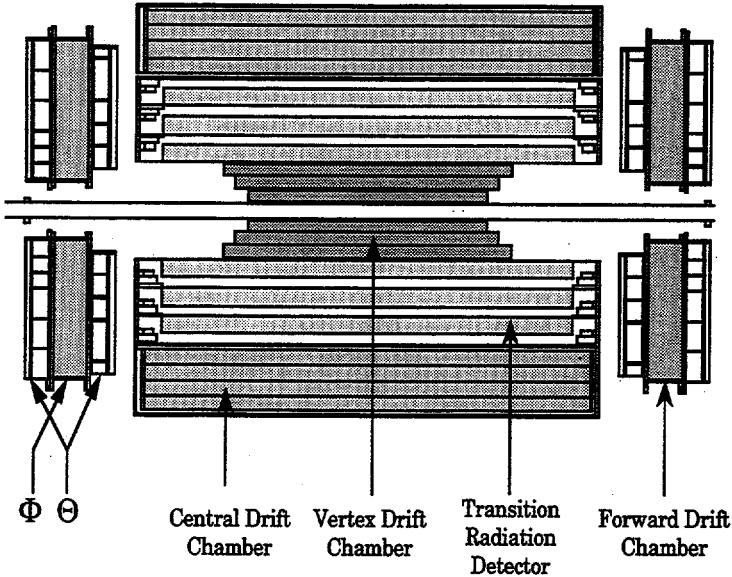
Figure 3.6: Arrangement of the DØ central detectors.

the central and forward regions, respectively. The transition radiation detector provides additional information useful for separating pions from electrons.

Fast analog-to-digital converters with ≈ 10 ns sampling time are used in the CD readout. With the typical drift velocity of 10-35 μm/ns, this corresponds to an effective detector granularity of 100-300 μm with relatively small ($\approx 6{,}000$) total number of readout channels [32].

In the following sections, brief descriptions of the CD components are presented.

3.4.1   Vertex Chamber (VTX)

The VTX (shown in Fig.3.7) is the innermost tracking detector in DØ . Its inner radius of 3.7 cm is just outside the beryllium beam pipe. It consists of three independent concentric layers of drift cells. In each cell, sense wires provide measurement of the r-ϕ coordinate. The electrostatic properties of the cells are determined by the grounded planes of grid wire on either side of the sense wire planes and the outer cathode field wires which shape the electric field in the cells. The resistivity of the sense wires provide a measurement of the

Sense
Grid
Cathode
Coarse Field
Fine Field
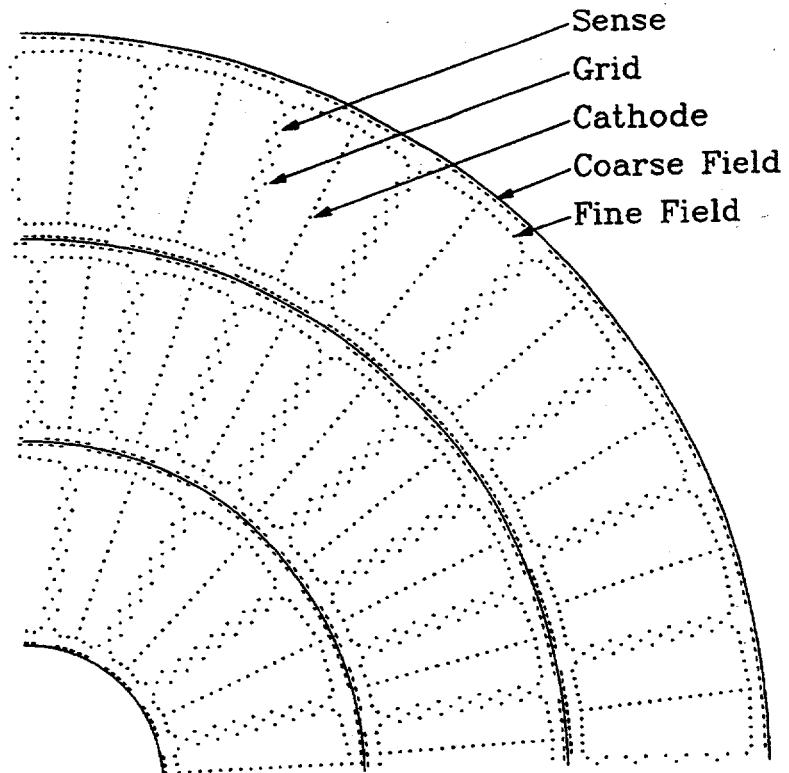
Figure 3.7: End view of one quadrant of the VTX

z position by charge division from readouts at both ends. Overall, the vertex chamber has a resolution of 60 μm in r-ϕ and 1.5 cm in z (for isolated tracks). In this analysis, tracks in the VTX chamber were used only if they matched with tracks found in the outer drift chambers. This limited use of this chamber is due to the difficulty of tracking (with good efficiency and good z determination) in the high multiplicity enviroment near the beam.

3.4.2 Transition Radiation Detector (TRD)

The TRD (shown in Fig.3.8) occupies the space immediately outside the VTX. Transition radiation X-rays are produced when highly relativistic particles ($\gamma > 10^3$) traverse boundaries between media with different dielectric constants. The TRD consists of three separate units, each containing a radiator and an X-ray detection chamber. The radiator is made with stacks of foils separated by gaps filled with gas. The detection of the emitted
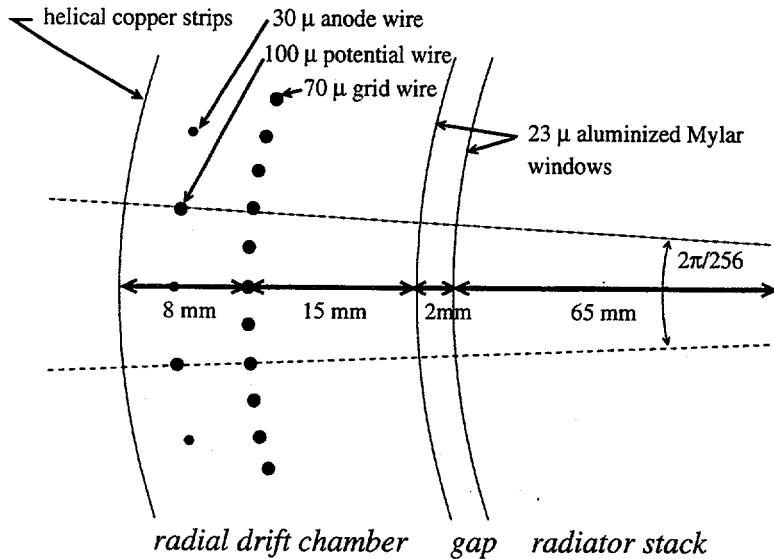
Figure 3.8: End view of a TRD module.

X-rays is achieved with a two-stage time-expansion radial-drift proportional wire chamber. The X-rays convert mainly in the first stage of the chamber, which is filled with gas, and the resulting electrons drift radially towards the sense wires in the second stage of the chamber, separated from the first one by a grounded wire grid. The sense wires measure the collected charge and the arrival time. The z coordinate is determined by a set of helical pads mounted on the outer wall of the chamber. The primary goal of the TRD is to discriminate electrons from pions. Because of their vastly different masses only electrons produce measurable transition radiation, providing a rejection factor of 50 against pions with 90% efficiency for isolated electrons.

3.4.3 Central Drift Chamber (CDC)

The CDC (shown in Fig.3.9) fills the space between the TRD and the central calorimeter. It consists of four concentric layers of drift cells. Each cell has anode wires in the center and cathodes at the cell boundaries. In addition, two transmission lines (delay lines) with carefully controlled inductance and capacitance and a minimum resistance are read from
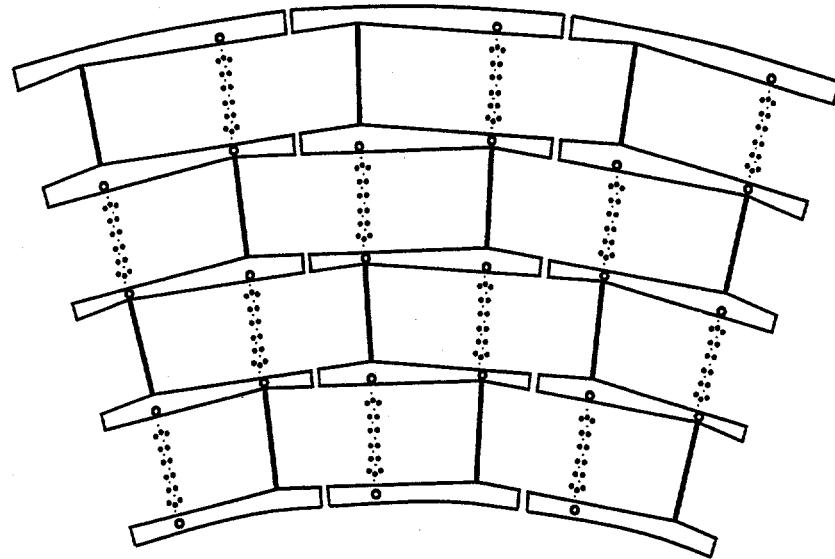
Figure 3.9: End view of a CDC section.

both ends in each cell. The induced signals in the delay lines (from signals in neighboring sense wires) then propagate to both ends with known velocity, from which the z coordinate is determined. The position resolution is 180 μm in r-ϕ and 2.9 mm in z. The CDC is of key importance to the analysis presented in this thesis. It is used to determine the position of the primary vertex, from which the polar angles of electrons and jets are determined, and is a powerful tool for electron identification. In addition to track position and direction, the CDC provides the ionization per unit length (dE/dx) which is useful to reject photon conversions.

3.4.4 Forward Drift Chambers (FDC)

The two FDC's (one of which is shown in Fig.3.10) extend the tracking coverage to the forward region in front of the two end-cap calorimeters. Each FDC consists of three chambers stacked along the beam direction. The middle chamber has radial wires and measures the ϕ coordinate of tracks. The outer two chambers have azimuthal wires and measure the polar angle θ. The electrostatics of the cells is analogous to the CDC cells
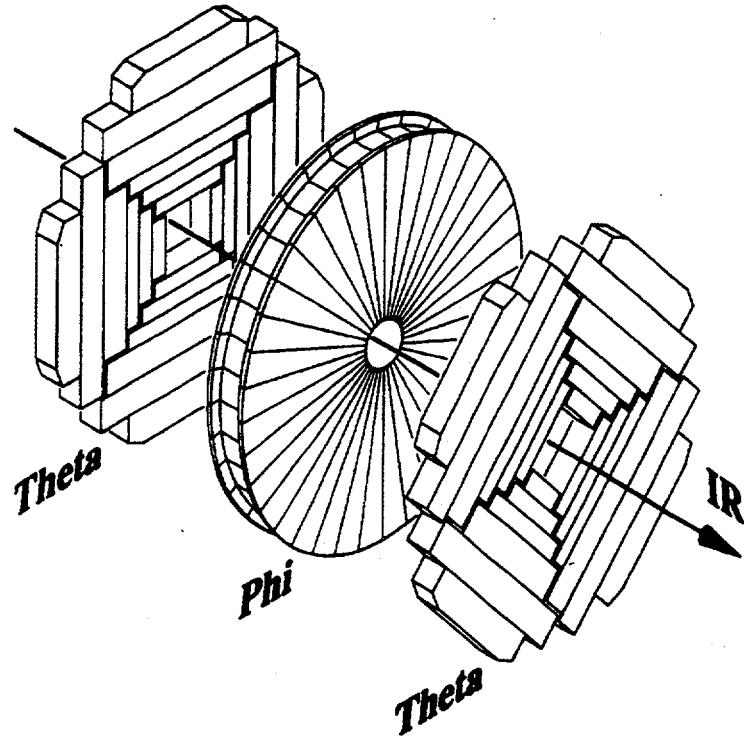
Figure 3.10: FDC layout.

(see Sec. 3.4.3). As for the CDC, the coordinate parallel to the sense wire is measured with delay lines. The position resolution is approximately 200 μm in the two coordinates. The function and use of the FDC tracks in this analysis is primarily for electron identification. The FDC also provides the ionization per unit length (dE/dx) of tracks which is useful to reject photon conversions.

3.5 Muon System

The DØ muon system consists of five separate solid-iron toroidal magnets, in addition to sets of proportional drift tube chambers to measure track coordinates. The purpose of the system is two-fold: identification of muons and momentum measurement.

Most of the particles produced in a $p\bar{p}$ collision lose all their energy in the calorimeters. Muons, on the other hand, traverse the calorimeter depositing (typically) only a small

amount of energy through ionization. This allows the identification of muons even when they are part of a hadronic jet.

The bend in the toroids, due to the 1.9 T magnetic field, is approximately in the $r - z$ plane. To measure the track position and momentum, a closely spaced set of measurements of the track before the toroid, and two sets of measurements, separated by 1-3 m, after the toroid, are provided. Multiple Coulomb scattering in the iron toroids limits the relative momentum resolution. The resolution for $1/p$ is approximately Gaussian and given by

$$\sigma(1/p) = \frac{0.18(p - 2)}{p^2} \oplus 0.003, \tag{3.6}$$

where p is in GeV/c units.

The muon system consists of a central toroid (CF), which covers the region $|\eta| \leq 1$, two end toroids (EFs), for the $1 < |\eta| \leq 2.5$ region, and the small-angle muon system (SAMUS) toroids, for $2.5 \leq |\eta| \leq 3.6$.

The anode wires of the proportional drift tubes are aligned with the magnetic field to measure the bending coordinates. The position of the track along the wire is determined from the time difference between the arrival of the signal to both ends of the anode wires. Additional information about the position of the track along the wire is obtained through the readout of diamond-shaped cathodes.

3.6   Trigger and Data Acquisition

The trigger and data acquisition systems select and record interesting physics events for offline analysis. The trigger is done in three levels of increasing sophistication. The Level 0 is a scintillator based trigger that signals the occurrence of an inelastic proton-antiproton collision. For the relatively large luminosities achieved during Run Ia and Run Ib, the probability for such an occurrence is almost one (for any given beam crossing). Therefore, typical Level 0 rates are 286 kHz $\approx 1/3.5$ μsec (the time interval between bunch crossings). The Level 1 trigger consists of a collection of hardware trigger elements most of which reach a trigger decision in less than 3.5 μsec, and therefore introduce no dead-time. Some hardware triggers that take more than 3.5 μsec are referred to as Level 1.5. The rejection provided by the Level 1/1.5 reduce the event rate to approximately 100 Hz. Events passing

the Level 1/1.5 trigger are transfered to a farm of microprocessors, where sophisticated software algorithms are implemented to further reduce the rate to a level (typically 2 Hz) at which it can be transferred to a host computer and then saved in magnetic tapes. Figure 3.11 shows a schematic of the DØ trigger system, data acquisition system and data flow.

3.6.1   Level 0 Trigger

The Level 0 uses two hodoscopes of scintillator counters mounted on the front surface of the end calorimeters. They cover a rapidity region of $1.9 \leq |\eta| \leq 4.3$ which provide a 99% efficiency for detecting non-diffractive inelastic collisions.

In addition to identifying inelastic collisions, the Level 0 trigger provides information on the z-coordinate of the primary interaction vertex. This information is useful to determine the transverse energy (E_T) of objects found in the calorimeter (electron, photons or jets) used to make trigger decisions at Level 1 and Level 2. The spread of the Tevatron vertex distribution is approximately 30 cm. The Level 0 provides a determination with a resolution of 3 cm (to Level 2), from a 150 ps time resolution of the scintillator counters.

For beam crossings in which more than one proton-antiproton collision occur (a likely situation for instantaneous luminosities larger than 5×10^{30} cm^{-2} s^{-1}), the timing information is imprecise. Such events are flagged by the Level 0 system as likely multiple interaction events.

The Level 0 is also used to calculate the instantaneous luminosity. This is done by counting (by means of scalers) the number of crossings for which the Level 0 did not fire. For the calculation, the total proton-antiproton inelastic cross section and the Level 0 acceptance are also used.

3.6.2   Level 1 Trigger

The Level 1 is a special-purpose hardware processor that uses information from the calorimeter and from the muon system to perform triggering decisions. The primary input for those decisions are 256 trigger terms. These 256 terms are then used to define specific triggers, by requiring that some of the terms be true (requirements) while others be false
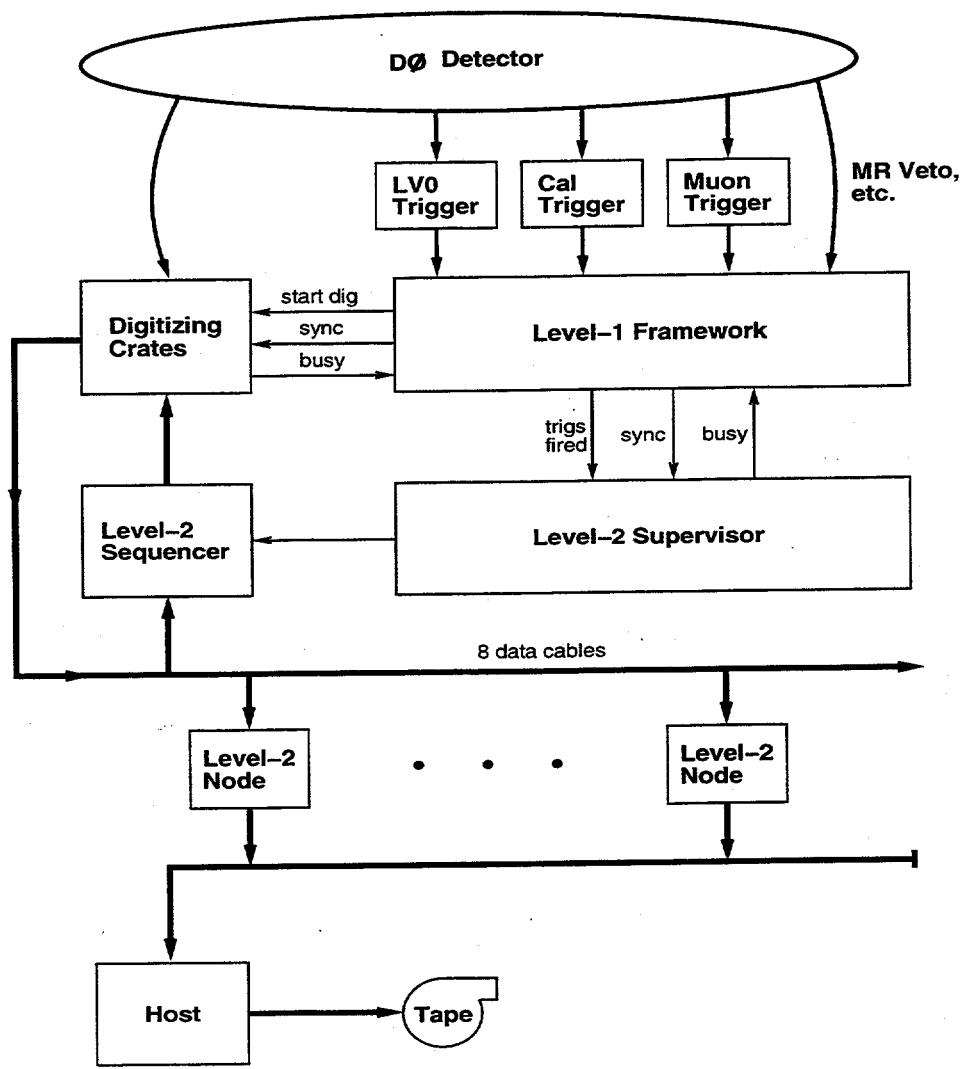
Figure 3.11: Overall layout of the DØ trigger and data acquisition system.

(vetos). Level 0 information and accelerator timing signals are also available to the Level 1 trigger.

For each specific trigger there is also a prescale factor used to discard a predetermined portion of the events that fired the trigger to further reduce the output rate, if needed.

Events that fired any specific trigger are transferred to digitizing crates. The Level 1 system controls the begining of the digitization and also informs the Level 2 system that an event is ready for transfer (after the digitization). What digitizing crates are read into the Level 2 depend on the specific trigger. However, for normal physics running, all the crates are read out for every specific trigger. For the specific triggers that require a Level 1.5 confirmation, the digitization is aborted if no such confirmation is received.

For illustration of the trigger logic and use, the specific triggers used for the analysis presented in this thesis are described in detail in what follows. The first trigger used was designed to accept events with two electrons. This Level 1 trigger (em_2_med) requires the presence of two electromagnetic energy towers (trigger towers are 0.2 × 0.2 in η-ϕ space) with more than 7 GeV E_T each. In Run Ib, this trigger required, in addition, a Level 1.5 confirmation, requiring one tower (0.2 × 0.1 in η-ϕ space) with more 12 GeV E_T and with an electromagnetic fraction larger than 0.85.

The second trigger was designed to accept events with one large transverse momentum electron. This Level 1 trigger (em_1_med in Run Ia and em_1_high in Run Ib) requires one electromagnetic energy tower with $E_T > 10$ GeV. In Run Ib, this trigger also required a Level 1.5 confirmation, requiring one tower with $E_T > 15$ GeV and with an electromagnetic fraction larger than 0.85.

The triggers described above were kept unprescaled for the duration of the corresponding running periods. Therefore, the full luminosity available was used for the searches presented here. However, the single electron trigger in Run Ib contained an additional veto, to avoid triggering on junk events caused by accelerator backgrounds (particularly due to the Main Ring beam which traverses the DØ calorimeter). For this reason, the total effective luminosity used for the single electron analysis is slightly smaller than that for the two-electron analysis (see Sec. 5.2.1 and 5.3.1).

3.6.3 Level 2 Trigger

Events that pass the Level 1/1.5 trigger are transferred to the Level 2. This consists of a farm of 48 Vaxstation 4000/60 nodes. These nodes run software filters that use the entire digitized event information to reach a final trigger decision. In the nodes, the event data are put into the final data structure used for the offline analysis. For each Level 1 specific trigger that was fired, a set of scripts (filters) is executed. These scripts call specific tools (subroutines) designed to identify physics objects such as electrons, photons, jets and missing E_T with variable parameters (such as E_T thresholds and the numbers of objects of each kind). If an event passed at least one of these scripts (filters), the event is transferred to the host computer and recorded in a magnetic tape.

Again, for the purpose of illustrating the Level 2 filtering capabilities and algorithms, the filters used for this analysis are described in detail in what follows.

The first filter (ELE_2_MAX in Run Ia and EM2_EIS2_HI in Run Ib) is designed to select events with two electrons. It requires the presence of two EM clusters with $E_T > 20$ GeV each. In addition, the filter requires that the energy depositions be consistent with that of electrons. This is achieved by applying a cut on the maximum fractional energy (of the total EM energy in the cluster) in the first hadronic layer and in the fourth EM layer allowed. In addition, transverse shape and isolation cuts are applied. Because of their vital importance in the trigger, all these shape cuts were tuned using test beam data and Monte Carlo data to be more than 99% efficient.

The second filter (ELE_HIGH in Run Ia) requires the presence of a single electron with $E_T > 20$ GeV with the same shape and isolation cuts as described above. Because of its large rate, this filter was not kept unprescaled during Run Ib. Therefore, a filter (EM1_GIS_HI) requiring an EM object with $E_T > 40$ GeV was used instead.

The efficiencies of the triggers used for the search described in this thesis were calculated using a Monte Carlo simulation of the trigger system and the Level 2 selection algorithms. These are included in the description of the overall efficiency calculation in Sec. 5.2.2 and Sec. 5.3.2.

The next chapter describes the offline reconstruction algorithms used to identify and measure physics objects (electrons, jets, muons, etc) for further analysis.

Chapter 4

Event Reconstruction

In this chapter the basic algorithms used to reconstruct and identify physics objects are presented. The decay channels of right-handed W bosons studied in this thesis contain electrons and jets in the final state. For this reason, special emphasis is put on the algorithms used for reconstruction and identification of these two types of objects.

4.1   Electron Reconstruction and Identification

The first step in the offline reconstruction of electrons consists in finding all the EM calorimeter clusters. The building blocks of an EM calorimeter cluster are towers of cells (see Sec. 3.3) from all the electromagnetic layers (EM1, EM2, EM3, EM4) and the first fine hadronic layer (FH1). These towers (0.1×0.1 in $\eta \times \phi$ space) are then grouped into clusters using a nearest neighbour (NN) algorithm. The NN algorithm starts up with the highest energy tower and adds to the cluster the tower with largest energy within the eight neighbouring towers. The newly added tower then replaces the function of the first tower but only including a neighbouring cell if it has not yet been included in the cluster, and so on. The algorithm completes a cluster when the next tower to be added has less than a threshold energy of 0.05 GeV. The most energetic unused tower is then used to start a new cluster. Only EM calorimeter clusters with total energy greater than 1.5 GeV are kept as electron candidates.

The EM calorimeters are typically 20 radiation lengths (X_0) deep. Therefore, very little energy from an electron shower leaks into the first hadronic layer. For this reason, only clusters that have more than 90% of their energy in the EM layers are kept as electron candidates.

At this point, clusters are required to have more than 40% of their energy in the central (highest energy) tower. This is a very rudimentary way of checking that the energy deposition is consistent with an electron shower, which should have a large fraction of its energy in one or two towers (Molière Radius = 1.14 cm, and a typical tower is 5-10 is cm wide).

The position of the cluster is then calculated with an algorithm that uses the logarithm of the energies in the cluster cells as the weight (see Appendix A). This method relies on the fact that the electron showers are of exponential form and therefore the tails of the shower provide useful information about the centroid position.

Electrons are expected to have a track in the central detectors (See Sec. 3.4) pointing to the calorimeter cluster. In the absence of a magnetic field, the tracks left by charged particles are straight lines. In order to find the track corresponding to the EM cluster, a road is defined around the direction of the electron candidate. This direction is defined using the primary vertex of the event and the calorimeter cluster position (see Appendix A). In the ϕ direction the road size is ± 0.1 radians. In the θ direction the road size varies between ± 0.25 radians (for central candidates) and ± 0.1 radians (for forward candidates). Only clusters with at least one track in this road are kept as electron candidates. If there are many tracks in a given electron road, the track that has the smallest distance between the calorimeter centroid position (at the EM3 layer) and the extrapolated track is chosen.

All the requirements explained above provide a very loose definition of an electron. As a consequence, a typical sample of these objects is predominantly due to hadronic jets for which π^0 and η mesons carry most of the energy and for which the associated tracks are due to soft charged pions or to photon conversions within the jet. In order to reduce the probability of identifying hadronic jets as electrons, while maintaining a good efficiency for real electrons, the definition of an electron needs to be further refined. This is achieved by applying cuts on the set of variables defined below.

Track ionization The track measured in the central detectors is required to have an ion-

ization per unit length consistent with that of a minimum ionizing particle. This is particularly useful for rejecting photon conversions. Because of the lack of a magnetic field, e^+e^- pairs from conversions have constant and small angular separations and are therefore often reconstructed as a single track. For e^+e^- pairs that merge into a single track the ionization per unit length is twice that of a single electron.

Cluster-track match The track found in the road of an EM cluster is required to match with the cluster position in azimuth and pseudorapidity. The significance of the match defined as

$$\text{track-match significance} = \sqrt{\left(\frac{\Delta\phi}{\sigma_{\Delta\phi}}\right)^2 + \left(\frac{\Delta z}{\sigma_{\Delta z}}\right)^2}, \qquad (4.1)$$

for EM clusters in the CC and

$$\text{track-match significance} = \sqrt{\left(\frac{\Delta\phi}{\sigma_{\Delta\phi}}\right)^2 + \left(\frac{\Delta r}{\sigma_{\Delta r}}\right)^2}, \qquad (4.2)$$

for EM clusters in the EC, where $\Delta\phi$, Δz and Δr are the mismatch between the track and the cluster and σ_x is the resolution for the observable x. The resolution for the matching in the azimuthal direction is 2–3 mm. For the other coordinates the resolution is 1–3 cm.

Covariant matrix χ^2 (H-matrix) The shower shape [34] may be characterized by the fraction of the cluster energy deposited in each layer of the calorimeter. These fractions are also dependent on the incident electron energy. However, they are correlated, *i.e.* a shower which fluctuates and deposits a large fraction of its energy in the first layer will then deposit a smaller fraction in the subsequent layers and vice versa. A covariant matrix (M) of 41 observables x_i is used to take into account the energy depositions in all the layers and their correlation to characterize the *electron-ness* of the shower. The matrix elements were computed from samples of N Monte Carlo (MC) electrons with energies ranging between 10 and 150 GeV. They are defined as

$$M_{ij} = \frac{1}{N} \sum_{n=1}^{N} (x_i^n - \overline{x}_i)(x_j^n - \overline{x}_j), \qquad (4.3)$$

where x_i^n is the value of the ith observable for the nth electron and $\overline{x}_i$ is the mean of the x_i observable. The observables are the fractional energies in layers EM1, EM2,

EM4, and the fractional energy in each cell of a 6 × 6 array of EM3 cells centered around the most energetic tower. The remaining observables are the logarithm of the total energy of the cluster and the z-coordinate of the primary vertex position. A matrix is computed for each of the 74 towers into which the calorimeter is subdivided in pseudorapidity. For a measured shower characterized by the observables x'_i, the covariance parameter

$$\chi^2 = \sum_{i,j=1}^{41} (x'_i - \overline{x}_i)H_{ij}(x'_j - \overline{x}_j), \tag{4.4}$$

where $H = M^{-1}$, measures how consistent its shape is with that expected from an electromagnetic shower.

Cluster isolation The EM clusters are required to be isolated from other objects in the event. The isolation variable is defined as

$$\text{Isolation} = \frac{E(0.4) - EM(0.2)}{EM(0.2)}, \tag{4.5}$$

where $E(0.4)$ is the energy in the calorimeter cells within a radius of 0.4 in $\eta - \phi$ space and $EM(0.2)$ is the EM energy within a 0.2 radius.

The plots in Fig. 4.1 show the distributions of these four variables for a sample of real electrons (solid histograms) from collider $W \rightarrow e\nu$ events. The events were selected from a high transverse momentum ($E_T > 50$ GeV) and central ($|\eta| < 1.1$) electron sample that passed the single electron trigger (see Sec. 3.6.3) requirement and that had large missing transverse energy ($\not{E}_T > 25$ GeV). The corresponding distributions for a sample of highly electromagnetic jets (dashed histograms) from the collider data are also shown. These were selected from the same parent sample (with same kinematic, fiducial and trigger requirements) as the $W \rightarrow e\nu$ events, but requiring that the EM fraction of the largest central EM cluster in the event be in the range $0.90 \leq EM\ fraction \leq 0.95$, ensuring minimal true electron contamination. For each variable, the two distributions are normalized to the same area. For illustration, the value of the cut applied in one of the two analyses presented in this thesis (see Sec. 5.3) on each variable is also shown (arrows).

The plots in Fig. 4.1 serve as a qualitative description of the differences in these electron-identification variables between real electrons and the backgrounds. The efficiency and

background rejection that can be achieved with these variables depend primarily on the cut values used and on the fiducial region where the electrons are detected (EC vs. CC). Both of these (cut values and fiducial region) are different for the two methods used for this search. For this reason, the cut values and fiducial region and their resulting efficiency and background rejection are discussed in the sections (Sec. 5.2 and Sec. 5.3) where the two different methods are presented.

4.2   Jet Reconstruction

The jet finding algorithm [34] defines a jet by summing the E_T in a cone of radius $R = \sqrt{\Delta\eta^2 + \Delta\phi^2}$. For the analyses presented in this thesis, jets defined with $R = 0.5$ were used. The first step in the jet reconstruction is the formation of preclusters with contiguous cells out to a radius of $R = 0.3$. Only calorimeter towers with $E_T > 1$ GeV are included in the preclusters. The preclusters then become the starting point for jet finding and the precluster center is used as the initial cone center. A new E_T weighted center is then obtained using E_T of all towers within a radius $R \leq 0.5$. The process is then repeated with the new calculated center until the jet is stable. A cluster of energy must have $E_T > 8$ GeV to be kept as a jet. If two jets have some calorimeter cells in common, which can happen if a precluster seed is found at a distance between one and two radii from the center of an already formed jet, their energies are combined or split. The jets are combined into one jet if more than 50% of the energy in the lower E_T jet is also part of the higher E_T jet.

The jet energy resolution is extracted from the imbalance in E_T between the two jets in dijet events and from the imbalance between the photon and the jet in direct photon ($\gamma +$ jet) events. The resolution is parameterized using:

$$\left(\frac{\sigma_E}{E}\right)^2 = C^2 + \frac{S^2}{E} + \frac{N^2}{E^2}, \tag{4.6}$$

where the constant (C), sampling (S) and noise (N) constants are given for various calorimeter fiducial regions in Table 4.1 [34]:
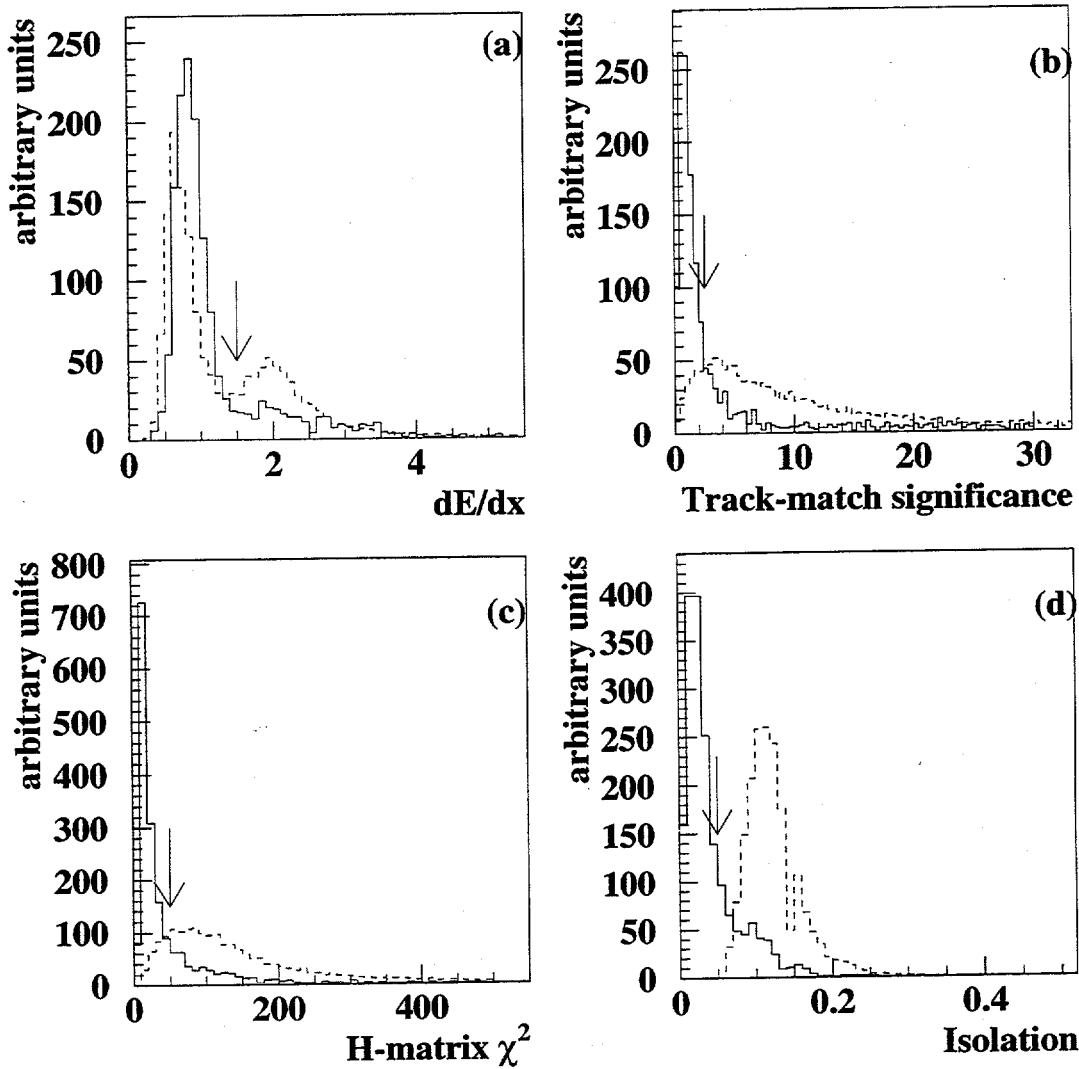
Figure 4.1: Comparison of the electron identification variables for electrons from $W \to e\nu$ (solid histograms) and for EM jets (dashed histograms). (a) Central track ionization. (b) Track match significance between the central track and the calorimeter cluster position. (c) Covariant matrix χ^2. (d) EM cluster isolation.

η region	Constant Term (C)	Sampling Term (S)	Noise Term (N)
$|\eta| < 0.5$	0.0 ± 0.005	0.81 ± 0.016	7.07 ± 0.09
$0.5 < |\eta| < 1.0$	0.0 ± 0.01	0.91 ± 0.019	6.92 ± 0.12
$1.0 < |\eta| < 1.5$	0.052 ± 0.006	1.45 ± 0.016	0.0 ± 1.4
$1.5 < |\eta| < 2.0$	0.0 ± 0.014	0.48 ± 0.07	8.15 ± 0.21
$2.0 < |\eta| < 3.0$	0.012 ± 0.58	1.64 ± 0.13	3.15 ± 2.5

Table 4.1: Jet energy resolution parameters for different calorimeter regions.

4.3 Missing E_T ($\not{E}_T$) Measurement

The missing transverse energy measurement is useful to infer the presence of undetected neutrinos. It is defined as

$$\not{E}_T = \sqrt{\not{E}_{Tx}^2 + \not{E}_{Ty}^2}, \tag{4.7}$$

where

$$\not{E}_{Tx} = -\sum_i E_i \sin(\theta_i) \cos(\phi_i) \quad \not{E}_{Ty} = -\sum_i E_i \sin(\theta_i) \sin(\phi_i). \tag{4.8}$$

The sums are over all cells in the calorimeter and ICD.

4.4 Offline Corrections

The absolute energy scale is set by the EM sections of the calorimeter. The EM energy scale is established by setting the invariant mass peak of the two electrons in inclusive dielectron events equal to the Z boson mass [35]. This absolute EM energy calibration was performed separately for the three calorimeter cryostats. Figure 4.2 shows the invariant mass of the two electrons M_{ee} in $Z \rightarrow ee$ collider events after the EM scale correction was applied. The first plot in the figure (a) shows M_{ee} for events that had both electrons in the central calorimeter (CC), while the other two (b and c) show M_{ee} for events that had one electron in the CC and one electron in the north and south end calorimeters (EC), respectively. Also shown (dashed line) is the value of the Z boson mass [35] which, by construction, agrees with the observed peak positions. Studies of π^0's, J/ψ and Z resonances
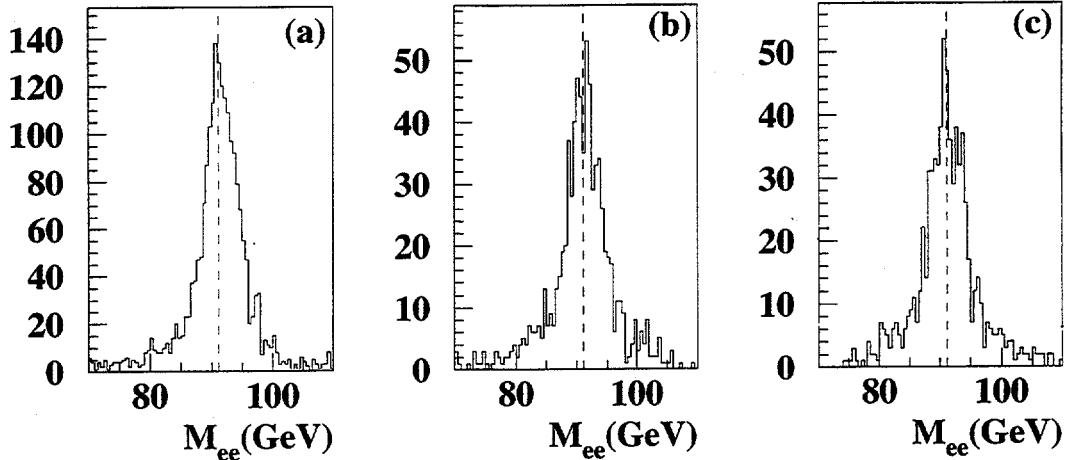
Figure 4.2: Invariant mass of two electrons in $Z \rightarrow ee$ data (after correction). M_{ee} is shown (after EM scale correction) for events with the electrons in different calorimeter modules: (a) CC-CC (b) CC-EC-north (c) CC-EC-south. The dashed line represents the value of the Z boson as measured by the experiments at LEP [35], which was used to determine the absolute EM energy scale.

indicate that the deviation from unity of $M_Z(\text{LEP})/M_Z(\text{D}\emptyset)$ is due solely to a scale factor with no offset. In addition, analyses of test beam electrons show the EM section to be linear to better than 1% in the energy range 10 GeV to 150 GeV [34].

Once the EM energy scale is fixed, the jet energy scale is determined relative to it. Several effects degrade the ability to measure jet energies: detector-related response variations and non-linearities, out-of-cone showering, deposition of energy due to uranium decays in the absorber plates, and energy deposited via the soft interaction of spectator partons within the proton and antiproton (i.e., underlying event).

To measure the response of the calorimeter to the fragmentation products associated with a jet, a variant of the Missing E_T Projection Fraction (MPF) method [36] was used. Events with one good isolated EM cluster that is balanced by a recoiling central jet were selected. The $\not{E}_T$ opposite the direction of the EM cluster equals the amount that the jet
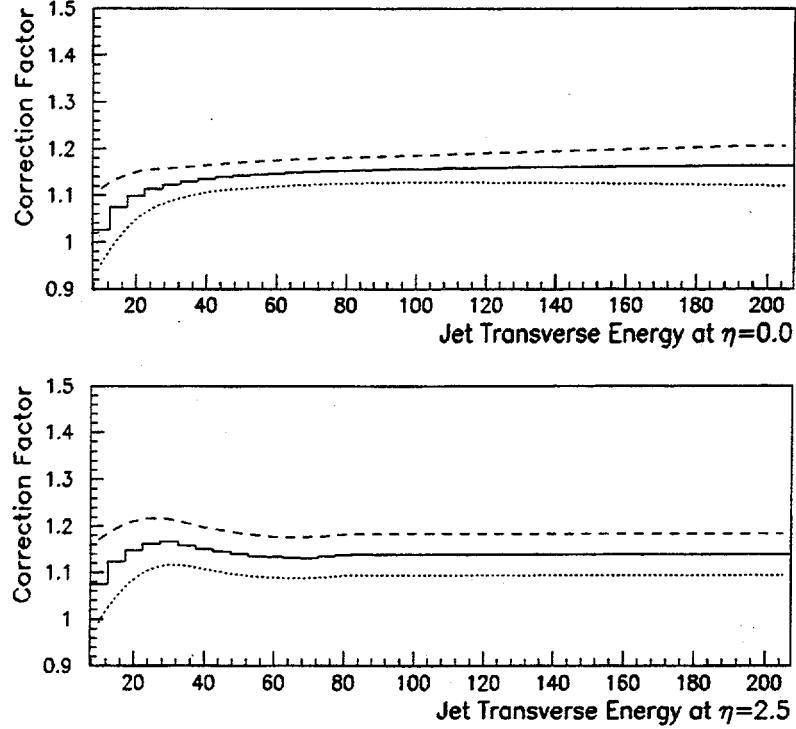
Figure 4.3: The MPF energy scale correction for collider data jets as a function of the jet E_T in the (a) central and (b) forward regions. The dashed curves represent the error band.

E_T is mismeasured due to the jet response. The quantity MPF is defined as:

$$\text{MPF} = \frac{\vec{\not{E}_T} \cdot \hat{n}_T^{EM}}{E_T^{EM}}, \tag{4.9}$$

where $\hat{n}_T^{EM}$ is the unit vector in the direction of the transverse energy (E_T^{EM}) of the EM cluster. The response of the calorimeter to the jet, denoted R_J, is then expressed as $R_J = 1 + \text{MPF}$.

Figure 4.3 shows the MPF correction applied to data jets. An equivalent procedure was also applied on Monte Carlo events to obtain the corresponding corrections for MC data. For those, the response as a function of energy with its error band is shown in Fig. 4.4.

The fragmentation products from final state partons falling within the jet cone produce wide showers in the calorimeter causing some of the energy to fall outside of the cone. To measure this out-of-cone fraction [34], single particle test-beam showers were substituted
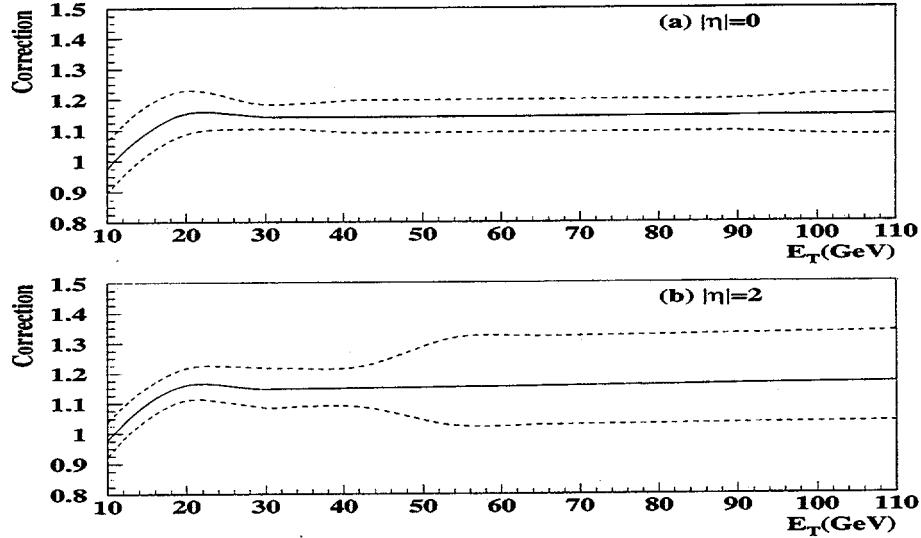
Figure 4.4: The MPF energy scale correction for Monte Carlo jets as a function of the jet E_T in the (a) central and (b) forward regions. The dashed curves represent the error band.

for fragmentation products in Monte Carlo jet events. A correction is then applied only for the energy deposited outside of the jet cone due to showering, and none for any out-of-cone particles due to fragmentation or radiation.

Having obtained the corrections described above, the dependence of the jet energy scale on eta and EM energy fraction was determined using dijet events. The calibration was then propagated to the forward regions by calculating the correction needed to bring a jet of a given eta into agreement with a central jet. The variation of the jet response with EM fraction was measured by balancing one jet of varying EM fraction with an average jet.

Corrections are also applied for the amount of unassociated energy in the fixed cone-size of a jet due to the underlying event, and for the energy originating in the decay of uranium nuclei.

The cumulative correction to collider data jets from all of these effects (including the MPF correction) is shown in Figure 4.5 [34]. It is typically [34] 25% for central jets above 20 GeV in E_T. The correction generally increases with η as out-of-cone losses increase, while it decreases at the very lowest jet E_T due to the 8 GeV jet reconstruction E_T threshold.
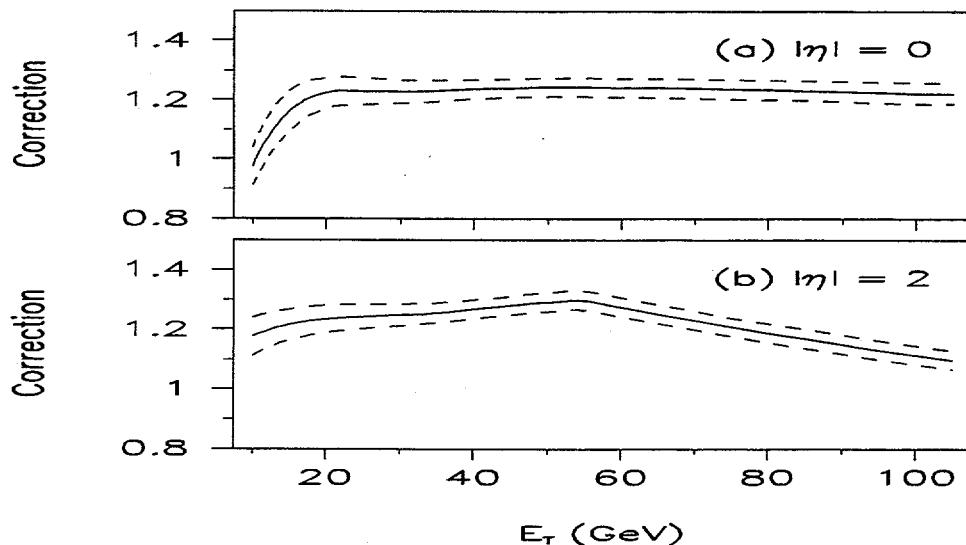
Figure 4.5: The cumulative energy scale correction (including the MPF correction) for data jets as a function of the jet E_T in the (a) central and (b) forward regions. The dashed curves represent the error band.

The last step, after the energies of electrons, photons and jets have been corrected, is the recalculation of $\not{E}_T$ using the new energies.

Chapter 5

Data Analysis

In this chapter, the data analysis is presented. The first section describes the Monte Carlo simulation of the W_R signal. The second section describes the search for two electrons plus two jets from the decay chain $\bar{p}p \to W_R^{\pm} \to e_1^{\pm}N \to e_1^{\pm}e_2^{\pm}jj$. The third and last section describes the shape analysis of the electron transverse energy spectrum in search for the Jacobian peak characteristic of the two-body $W_R^{\pm} \to e_1^{\pm}N$ decay.

5.1 Signal Monte Carlo

Monte Carlo (MC) event simulation is of central importance in the search for new particles such as right-handed W bosons. MC events are useful to determine what selection criteria (cuts) to apply, so that most of the potential signal events are retained while minimizing the number of non-signal events (background). Once the cuts have been chosen, the MC samples are used to determine the probability that a signal event passes all of the cuts (acceptance and efficiency).

For the simulation of W_R production and decay, the PYTHIA [37] program is used. This program includes hard scattering matrix elements, structure functions and initial and final state parton showers. Fragmentation (hadronization) of quarks and gluons is performed using the Lund fragmentation model, through the JETSET [37] program.

The original PYTHIA program does not contain the exact decay chain under study, but

it is flexible enough to produce the desired physics simulation by simply changing input parameters to the program. Specifically, a W' decaying into a fourth lepton generation matrix element was used. The fourth generation charged lepton was then replaced by an electron (or positron). Furthermore, the fourth generation neutrino decays were modified to model the decays of a massive first-generation right-handed neutrino N. The decay of N depends on the amount of mixing between the W_L and W_R (see Sec. 2.2.2).

1. In the extreme case of **no mixing**, or $\xi=0$, N was made to decay into an electron and a quark-antiquark pair (ud, cs or tb if $M_{N_R} > 170$ GeV). A weak decay matrix element, as the one used for b-quark decays, was used to generate this decay.

2. In the extreme case of **large mixing**, or $\xi \simeq 1$, N was made to decay into an electron and a standard W boson (on shell if $M_{N_R} > 80$ GeV). The standard W was then allowed to decay as in the standard model ($e\nu$, $\mu\nu$, $\tau\nu$ ud, cs). In this case a weak matrix element like the one used in t-quark decays was utilized.

Figures 5.1 and 5.2 show the distributions of the mass of the W_R generated, the transverse energy of the primary ($E_T^{e_1}$) and secondary electron ($E_T^{e_2}$) and the invariant mass of the two electrons for two MC samples with different values of M_{W_R} and M_{N_R}. The natural width of the W_R, Γ_{W_R}, shows the expected scaling with M_{W_R}:

$$\Gamma_{W_R} = \Gamma_W \frac{M_{W_R}}{M_W} = 2.1 \frac{M_{W_R}}{80.2}. \tag{5.1}$$

The $E_T^{e_1}$ distributions show the expected Jacobian peak (see Sec. 2.3). The histograms in Fig. 5.2 are of variables that depend on the mixing angle. The two extreme mixing cases, no mixing and large mixing, are shown.

For each mixing case 31 samples, of 400 events each, were generated with different values of M_{W_R} and M_{N_R} spanning the region of parameter space under study. The total of 24,800 events then passed a detailed detector simulation program called DØGEANT [38]. The DØGEANT program was used in a slightly simplified version, called the DØ Shower Library [39]. This version uses a library of particle showers instead of tracking the energy loss in the detector for each particle in an event. The main difference between the full version and this simplified one (apart from some loss of randomness) is that in
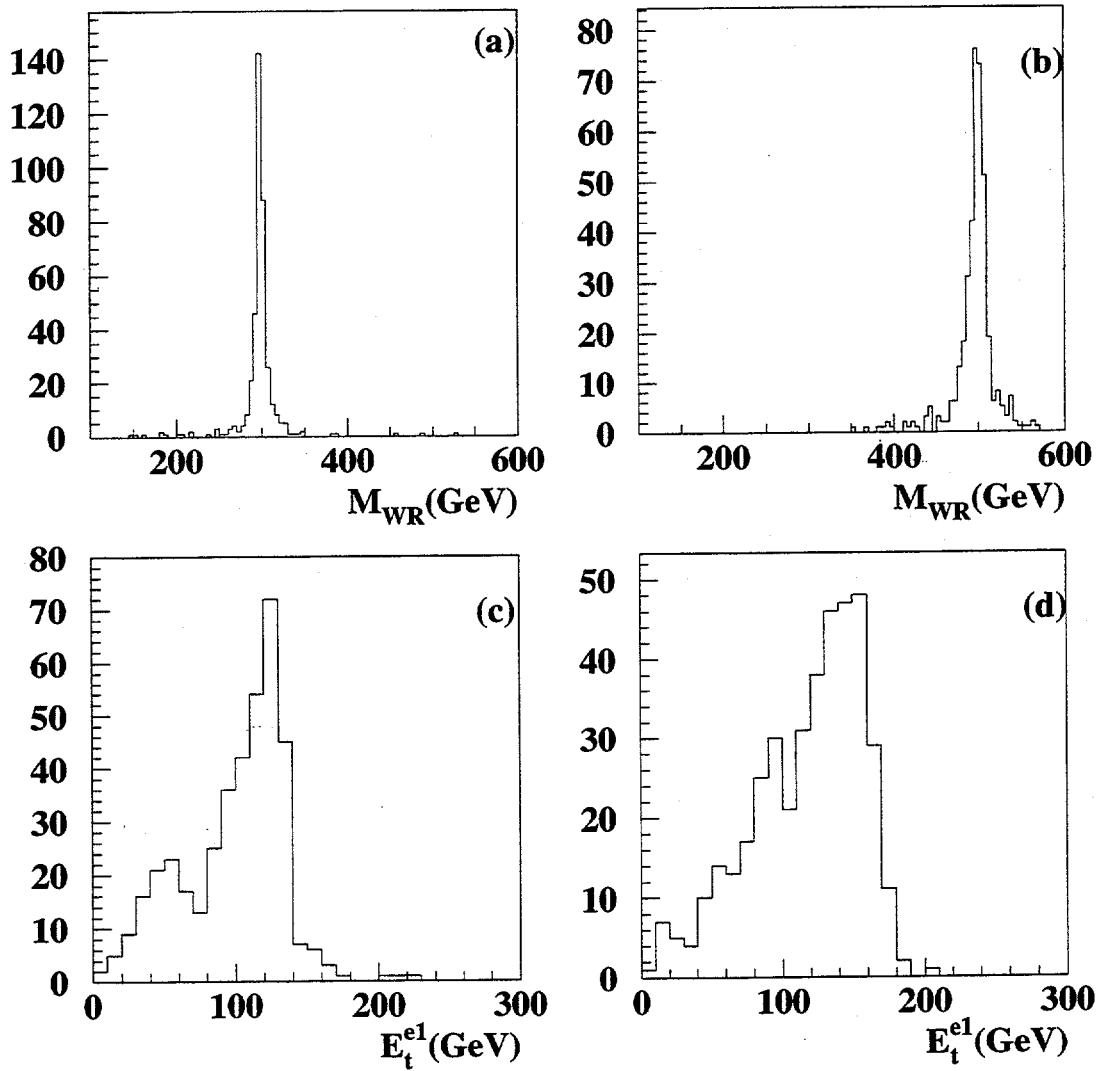
Figure 5.1: MC distributions of (a) the mass of the generated W_R and (c) the transverse energy of the electron in $W_R \to e_1 N$ for a sample with M_{W_R}=300 GeV and M_{N_R}=100 GeV. In (b) and (d) the same distributions are shown for a sample with M_{W_R}=500 GeV and M_{N_R}=300 GeV.
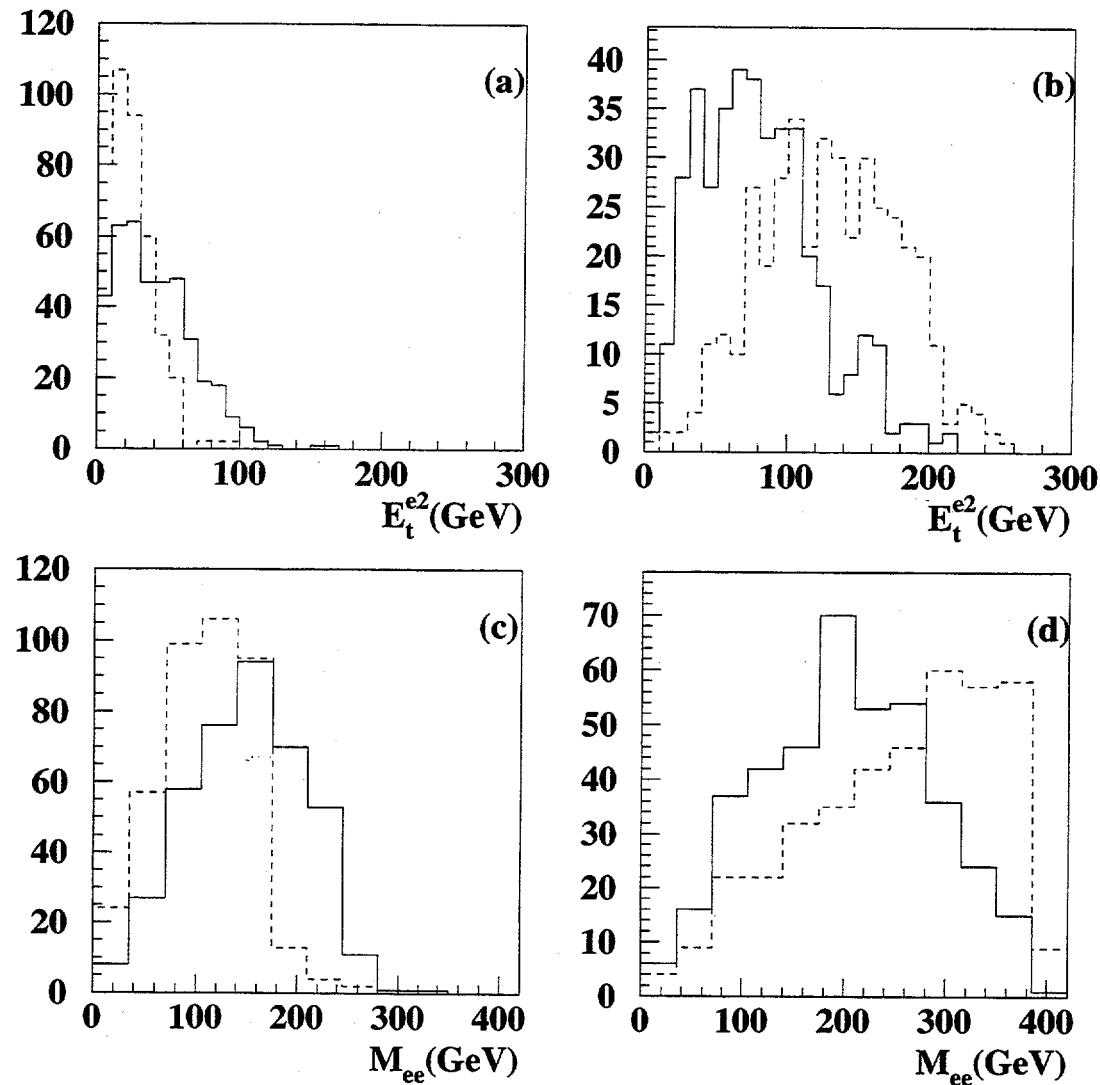
Figure 5.2: MC distributions of (a) the transverse energy of the electron in $N \rightarrow e_2 X$ and (c) the invariant mass of the two electrons, for a sample with $M_{W_R}=300$ GeV and $M_{N_R}=100$ GeV. In (b) and (d) the same distributions are shown for a sample with $M_{W_R}=500$ GeV and $M_{N_R}=300$ GeV. The solid histograms are for the no mixing case and the dashed histograms are for the large mixing case.

the library of showers only the energies of the cells containing the 95% of the total shower energy are retained (discarding the smallest energy cells). The remaining 5% of the energy is then distributed among the retained cells, maintaining their original energy distribution. Because most of the low energy cells in a cluster are in the region farthest from its center, this procedure causes Shower Library energy clusters to be slightly narrower than the full DØGEANT ones.

In order to simulate the trigger conditions in which the data was taken, the MC samples were passed through a trigger simulation program with a trigger configuration equivalent to the online configuration. In particular, the triggers used for the search (see Sec. 3.6.3) of two electrons and two jets (ELE_2_MAX in Run Ia and EM2_EIS2_HI in Run Ib) and the trigger used for the search of additional peaks in the inclusive electron E_T spectrum (ELE_HIGH in Run Ia) are fully simulated. The different trigger used for the peak search in Run Ib (EM1_GIS_HI) was not simulated. Therefore, its efficiency was studied using collider data (see Sec. 5.3.1 and Fig. 5.17).

The next step was to run the DØ offline reconstruction program, DØRECO, to produce the physics output in the same format as the data, after which, the standard offline corrections were applied (see Sec. 4.4). After this reconstruction, the analysis of MC events and data events is virtually identical, except for specific differences that will be stated in later sections.

In order to illustrate the effect and quality of the detector simulation and the reconstruction program, the plots in Fig. 5.3 show the invariant mass of the two electrons using MC information and using the reconstructed electrons after detector simulation. The reduction in the number of events after simulation/reconstruction is due maily to the absence of electromagnetic calorimeter coverage in the $1.2 \leq |\eta| \leq 1.4$ region and to the inefficiency in the reconstruction if the electron overlaps a hadronic jet.

In addition to the MC samples generated with the full detector simulation and standard reconstruction program (which take a large amount of CPU time to produce), a large number of PYTHIA generated events with a highly simplified detector simulation and reconstruction were used. This simplied version (or **dummy** MC) uses the basic detector geometry and nominal energy resolutions for EM and hadronic particles to fill calorimeter cells that are then clustered using a simple cone algorithm [40]. Even though these **dummy** MC events
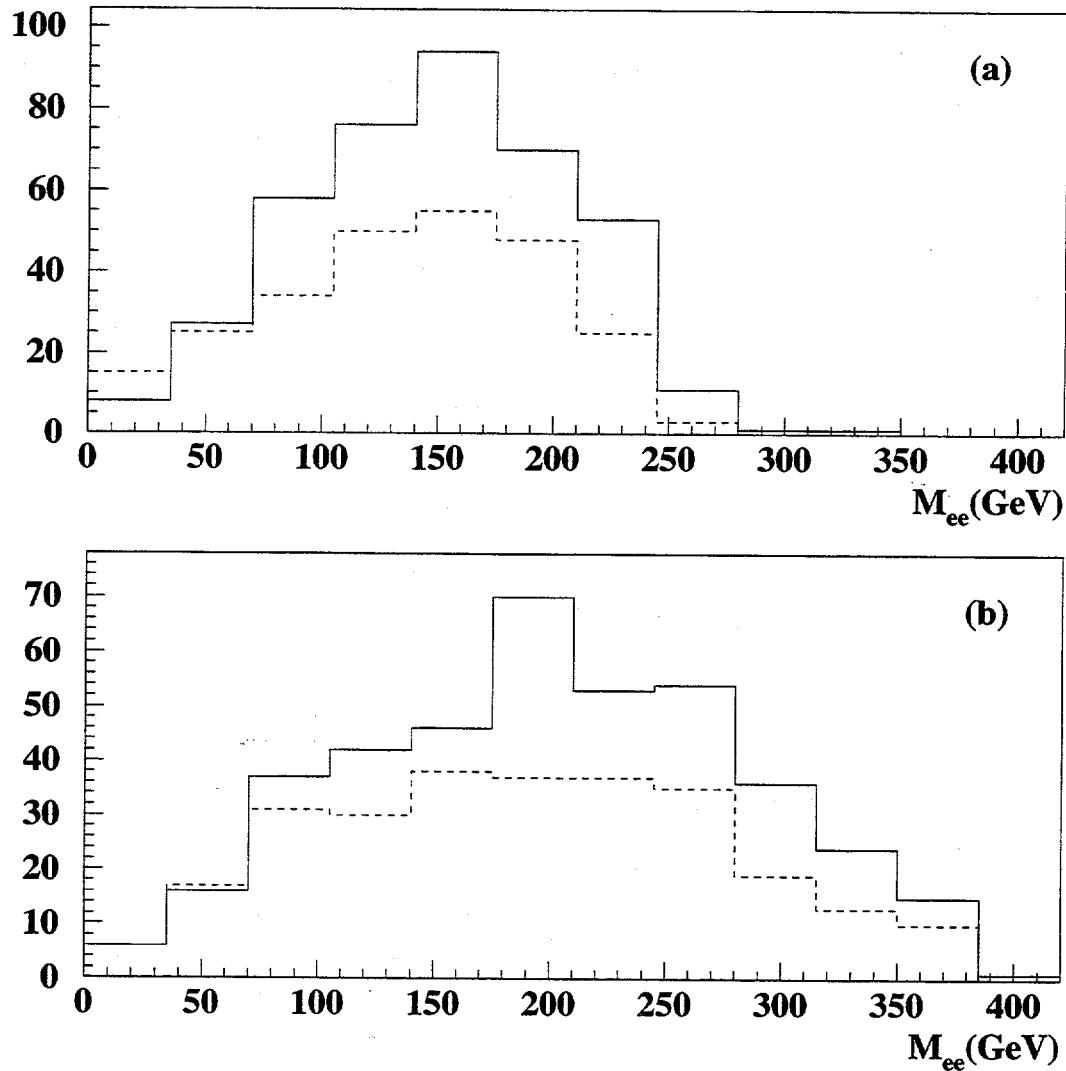
Figure 5.3: (a)The invariant mass of the two electrons using the MC quantities (solid) and using the reconstructed electrons after the detector simulation (dashed) for a sample with M_{W_R}=300 GeV and M_{N_R}=100 GeV with no mixing. (b) Same as (a), but for a sample with M_{W_R}=500 GeV and M_{N_R}=300 GeV. The inefficiencies are due to the lack of EM coverage in the inter-cryostat region and to the overlap of hadronic showers close to the electrons.

do not contain many of the necessary details for the complete analysis, they are very useful for studying the systematics and to fill the parameter space with a dense grid of points (within a reasonable CPU time and resources usage).

5.2   The Counting Search: $2e + 2j$

In this section, the search for events with two electrons and two jets is described. There is a large overlap between this analysis and other search analyses in DØ such as the first generation leptoquark search [41, 42]. A sample of events with two good electron candidates is first selected. Then, the presence of jets is required and kinematic cuts are imposed on the electrons and the jet(s). The remaining events are mostly due to Z+jets. Therefore a final cut on the invariant mass of the two electrons reduces the sample to very few events. The expected background is studied with a combination of MC and collider data.

5.2.1   Data Selection

Data from both run Ia and run Ib were analyzed. Run Ia data were taken in the Tevatron collider run from April 1992 to May 1993 and had a total integrated luminosity of $\int \mathcal{L} dt = \mathcal{L}^{Ia}_{int} = (14.8 \pm 0.81)$ pb^{-1}. Run Ib started in November 1993 and ended in August 1995, however at the time when this analysis was done (July 1995) only a partial set of $\mathcal{L}^{Ib}_{int} = (64.2 \pm 3.6)$ pb^{-1} of data was available (out of approximately 80 pb^{-1} for the entire Run Ib). The total number of events from global physics runs processed in run Ia was more than 12.5 million and in run Ib more than 30 million.

Before applying the analysis cuts, the energies of electrons, photons and jets were corrected. The main corrections are a scale factor applied to the electromagnetic energy response (that brings the Z mass peak to the LEP measured value) and a correction to the hadronic energy response (that balances the transverse energy of hadronic jets recoiling against highly electromagnetic jets). More details about these offline corrections are provided in Sec. 4.4.

From the total sample of collected events, W_R candidates were filtered with the following requirements:

Trigger: Events from run Ia and run Ib had to pass a hardware-level trigger (Level 1) requiring two electromagnetic trigger towers with $E_T > 7$ GeV and an online software-level filter (Level 2) requiring two electromagnetic clusters with $E_T > 20$ GeV, with some isolation and electron-shape requirements (see Sec. 3.6). This trigger

was chosen because it remained unchanged between run Ia and Ib (ELE_2_MAX in 1b and EM2_EIS2_HI in Ib).

Electrons: Two good electrons, according to a DØ standard [34], with $E_T > 25$ GeV must be found in the event. A good (tight) electron is an energy cluster (see Sec. 4.1 for details on these quantities):

- with high electromagnetic fraction: EMF > 0.90,

- in a fiducial region defined by $|\eta_{det}| < 2.5$,

- with shape consistent with that of an electron: H-matrix $\chi^2 < 100$,

- isolated: ISO < 0.1,

- with a track matching the calorimeter cluster position in ϕ and θ with significance (TMS) $\sqrt{\left(\frac{\Delta\phi}{\sigma_{\Delta\phi}}\right)^2 + \left(\frac{\Delta z}{\sigma_{\Delta z}}\right)^2} < 5.0$ and

- with a track ionization consistent with a single minimum ionizing particle: $\frac{dE}{dx} < 1.5$ or $\frac{dE}{dx} > 3.0$ for electrons in the central calorimeter (CC), and $\frac{dE}{dx} < 1.3$ or $\frac{dE}{dx} > 2.5$ for electrons in the forward region (EC).

Central electrons with $\frac{dE}{dx} > 3.0$ and forward electrons with $\frac{dE}{dx} > 2.5$ are kept because the specific ionization of single electrons has large tails. This choice maximizes the efficiency while not seriously hurting the background rejection. In order to further increase the efficiency, one electron is allowed to have $1.3 < \frac{dE}{dx} < 2.5$ if it is in the forward region (loose), where the specific ionization has a larger resolution.

Jets: Events must have two or more jets with $E_T > 25$ GeV in a fiducial region $\eta < |2.5|$. The jets have to be separated from the electrons in the event by: $\sqrt{\Delta\phi^2 + \Delta\eta^2} = \Delta R_{ej} > 0.25$. In addition, in order to avoid counting fake jets produced by the Main Ring (see Sec. 3.1) losses in the calorimeter, jets are required to have $\phi_j > 1.8$ or $\phi_j < 1.65$.

Kinematics: After the selection of two good electrons in the event, most of the remaining events are due to Z+jets. Therefore, the reduction of this large background is achieved by discarding events with $70 < M_{ee} < 110$ GeV.

Cuts applied	Number of events passing cut	
	Run Ia $\mathcal{L}_{int}^{Ia} = 14.8$ pb^{-1}	Run Ib $\mathcal{L}_{int}^{Ib} = 64.2$ pb^{-1}
$2e + 1j$, $E_T^{e,j} > 25$ GeV	51	173
$2e + 2j$, $E_T^{e,j} > 25$ GeV	2	20
$2e + 2j$, $E_T^{e,j} > 25$ GeV and no Z^0	0	2

Table 5.1: The effect of the cuts on the observed number of events. All the events on the table passed the trigger requirement and the electron identification criteria (see text). Two events from Run Ib survive all the cuts.

Table 5.1 shows the number of events passing the imposed cuts. After all the above cuts, no events are observed in the Ia sample. From the Ib sample, two events survive and are, therefore, the signal candidates. Relevant information about the candidate events is listed in tables 5.2. Figure 5.4 shows the invariant mass of the two electrons for eej and $eejj$ events.

5.2.2 Signal Efficiency

The calculation of the efficiency to detect signal events can be done by applying all of the same cuts, as were applied to the data, to infinite samples of a perfect MC with a perfectly accurate detector simulation. In reality, we must deal with finite MC samples generated by man-made event simulators and with good but not perfect detector simulation programs. For this reason, both MC and data events are used to calculate this efficiency (here the term efficiency means the combination of kinematic and fiducial acceptance with trigger and reconstruction efficiencies). More specifically, the calculation of the efficiency for finding good electrons requires a detailed knowledge of the EM shower development (both longitudinal and transverse), and therefore it can be more reliably determined using real electrons from the collider data.

The efficiency for the electron quality cuts was obtained [43] using $Z \to ee$ collider events. In events with two electromagnetic clusters, strict electron quality criteria were applied to one of the electrons (the tagging electron) and the invariant mass of the pair was required to be in the Z mass peak (to ensure high true electron content). The remaining

Object	E_T (GeV)	η	ϕ
Electron 1	62.5	1.73	4.82
Electron 2	48.6	0.78	0.81
Jet 1	82.6	-0.86	5.82
Jet 2	76.9	-0.33	3.07
Jet 3	33.0	-0.94	2.45
$\not{E}_T$	14.9	N/A	1.77
m(e_1e_2) (GeV)	113.7		
m($e_1j_1j_2$) (GeV)	359.9		
m($e_2j_1j_2$) (GeV)	250.1		
m($e_1e_2j_1j_2$) (GeV)	529.5		

Object	E_T (GeV)	η	ϕ
Electron 1	70.8	0.56	3.13
Electron 2	54.9	1.83	1.32
Jet 1	52.6	-1.62	6.12
Jet 2	26.3	-1.50	4.80
$\not{E}_T$	20.4	N/A	5.49
m(e_1e_2) (GeV)	130.1		
m($e_1j_1j_2$) (GeV)	239.6		
m($e_2j_1j_2$) (GeV)	368.0		
m($e_1e_2j_1j_2$) (GeV)	455.8		

Table 5.2: Candidate I (run 84870, event 29917) and Candidate II (run 90498, event 13191) kinematic information.
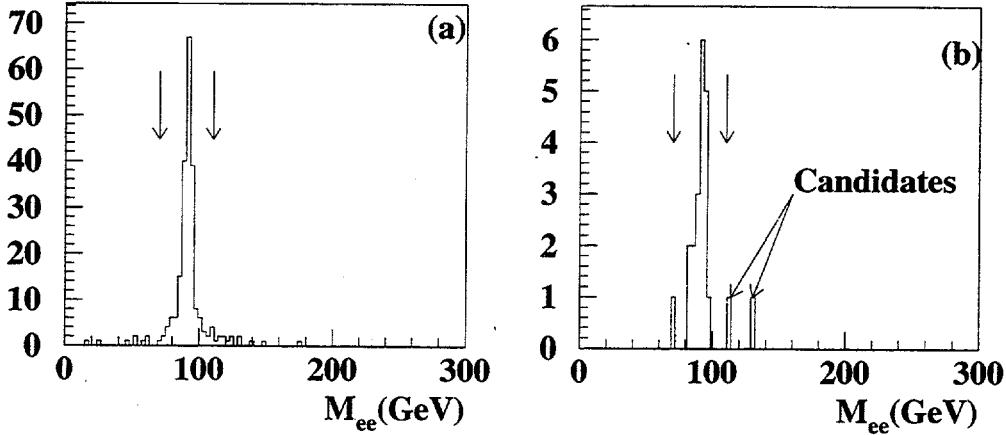
Figure 5.4: The invariant mass of the two electrons for events with (a) two electrons and one or more jets and, (b) two electrons and two or more jets. The two events surviving all the analysis cuts are shown.

electron is then unbiased because it was not required to pass the electron quality criteria. The efficiency of the electron quality cuts is then calculated as:

$$\epsilon_{e-ID} = \frac{N^{\text{pass}}}{N^{\text{unbiased}}}, \tag{5.2}$$

where N^{unbiased} is the total number of unbiased electrons and N^{pass} is the number of unbiased electrons that passed a given electron quality cut. Because of the difference between the forward and central detectors, the electron identification is different in those two regions. For this reason the efficiency was obtained separately for central (CC) and forward (EC) electrons. Table 5.3 shows the values of the electron identification efficiency for the tight (first row) and loose (second row) definitions for run Ia and Ib for the cuts used in this analysis. In the table, the CC entries for the loose cuts are empty because loose electrons are allowed only in the EC. The increased efficiency for EC electrons in Run Ib is due to improvements made to the FDC track-finding code. No electron-E_T dependence of the efficiency is observed [43].

The isolation cut is intentionally left out for reasons that will become clear in the following paragraphs. There is some dependence of these efficiencies on the the instantaneous

Cut Applied	Efficiency (%)			
	Run Ia		Run Ib	
	CC ϵ_{CC}^{Ia}	EC ϵ_{EC}^{Ia}	CC ϵ_{CC}^{Ib}	EC ϵ_{EC}^{Ib}
$\chi^2 < 100$ and TMS < 5 and dE/dx< 1.5 or dE/dx> 3.0 (if CC) dE/dx< 1.3 or dE/dx> 2.5 (if EC)	74.0 ± 2.5	39.8 ± 3.1	72.1 ± 1.4	47.7 ± 2.3
$\chi^2 < 100$ and TMS < 5 (loose in EC)	N/A	53.0 ± 3.6	N/A	62.3 ± 2.3

Table 5.3: Efficiencies of the electron quality cuts used in this analysis obtained from collider $Z \rightarrow ee$ events. The isolation cut is intentionally not included (see text).

luminosity, primarily due to the presence of multiple vertices. For a small percentage of the events the wrong vertex is chosen to construct the road (see Sec. 4.1) used to find the track corresponding to the electron. This effect, which is more important in run Ib due to its higher instantaneous luminosities, is taken into account in the values shown.

The combined electron quality cut efficiencies for two electrons in the same or different calorimeter cryostats were obtained with:

$$\epsilon_{CC-CC} = \epsilon_{CC}^2 \quad \epsilon_{EC-EC} = 2\epsilon_{EC-tight}\epsilon_{EC-loose} - \epsilon_{EC-tight}^2 \quad \epsilon_{CC-EC} = \epsilon_{CC}\epsilon_{EC-loose}. \quad (5.3)$$

The corresponding values of the two-electron efficiencies are shown in Table 5.4. As mentioned before, events with two loose electrons (two EC electrons failing dE/dx cut) are discarded. The uncertainties in all of the quoted efficiencies have contributions from the uncertainty in the background shape and normalization (systematic) and from the statistical error from the finite Z sample used.

In order to correctly combine the data derived efficiencies with the MC derived efficiencies/acceptances, a **matched** electron is defined. A MC electron has a **match** if there is an EM cluster with $E_T > 20$ GeV and with ISO < 0.1 that matches it in η and ϕ with:

$$\Delta R(e_{MC} - EM^{ISO}) = \sqrt{(\phi_e - \phi_{EM})^2 + (\eta_e - \eta_{EM})^2} < 0.1. \quad (5.4)$$

In this way, we rely on the reconstructed MC to determine only the isolation of a given electron, which depends primarily on the event's activity (such as jets) in its vicinity. This

Sample	Two-electron efficiencies (%)		
	CC-CC ϵ^{e-ID}_{CC-CC}	CC-EC ϵ^{e-ID}_{CC-EC}	EC-EC ϵ^{e-ID}_{EC-EC}
Run Ia	54.8 ± 3.8	39.2 ± 2.6	26.4 ± 2.7
Run Ib	52.0 ± 2.1	44.9 ± 1.7	36.7 ± 2.3

Table 5.4: Combined two-electron quality cut efficiencies. Events must have at least one tight electron to be used in the analysis.

method would fail for low E_T electrons because the isolation for those is a strong function of the noise and of the underlying event's energy.

Finally, then, to determine the overall efficiency, the reconstructed MC events are required to have two matched electrons in addition to the simulated trigger, jets, kinematic, fiducial and topological requirements. The MC events passing all these cuts are then grouped into three subsets according to the location of the two matched electrons (CC-CC, CC-EC and EC-EC) to obtain:

$$A_{CC-CC} = \frac{N_{CC-CC}}{N_{tot}}, \quad A_{CC-EC} = \frac{N_{CC-EC}}{N_{tot}}, \quad A_{EC-EC} = \frac{N_{EC-EC}}{N_{tot}}, \quad (5.5)$$

where N_{CC-CC} is the number of MC events passing all the cuts with the two matched electrons in the CC (analogous for the other two), and N_{tot} is total number of MC events generated (at that mass point). The overall efficiency is then:

$$\epsilon = A_{CC-CC}\epsilon^{e-ID}_{CC-CC} + A_{CC-EC}\epsilon^{e-ID}_{CC-EC} + A_{EC-EC}\epsilon^{e-ID}_{EC-EC}. \quad (5.6)$$

Table 5.5 shows the effect of the cuts on the acceptance for each of the MC samples (400 events each) for the no mixing case. The overall efficiency, as obtained from equation 5.5, and the expected number of events in 100 pb^{-1} of data (assuming the cross sections and branching fractions from Sec. 2.2.1 and Sec. 2.2.3) are also shown. The acceptance in the ee column includes the (simulated) trigger and the two matched EM clusters (therefore isolated) with $E_T > 25$ GeV. Table 5.6 shows the corresponding values for the large mixing MC samples.

As expected, the efficiency of the analysis cuts for small M_{N_R} (<30 GeV) almost vanishes because the N decay products are close together and therefore either an EM cluster is not

M_{W_R} (GeV)	M_{N_R} (GeV)	ee (%)	eej (%)	$eejj$ (%)	$eejj$ $M_{ee} \neq Z$ (%)	Overall efficiency ϵ (%)	Expected in 100 pb^{-1} (events)
100	30	4.6	0.2	0.0	0.0	< 0.1	0.0
200	30	5.8	2.9	0.0	0.0	< 0.1	0.0
200	100	25.2	20.9	6.0	1.4	0.7± 0.3	58.3
200	150	25.7	23.0	10.8	4.6	2.3± 0.6	86.9
300	30	2.6	1.2	0.0	0.0	< 0.1	0.0
300	100	34.3	29.3	10.1	9.8	4.9± 0.9	99.3
300	150	39.6	37.7	21.8	17.8	8.7± 1.2	140.8
300	200	48.2	47.5	31.9	19.7	9.6± 1.3	101.1
300	250	41.0	40.1	29.8	19.0	9.6± 1.3	36.9
400	30	2.9	1.2	0.0	0.0	< 0.1	0.0
400	100	36.5	34.6	14.9	14.4	7.2± 1.1	41.3
400	150	39.4	36.2	22.3	20.6	10.3± 1.3	53.2
400	200	47.8	47.3	32.9	29.0	14.2± 1.6	61.8
400	250	50.6	49.9	37.7	33.1	16.4± 1.8	53.0
400	300	51.6	51.6	41.8	32.9	16.4± 1.8	31.3
400	350	40.1	39.6	33.8	22.8	11.4± 1.4	7.1
500	30	0.5	0.0	0.0	0.0	< 0.1	0.0
500	100	27.8	25.7	11.8	11.8	5.8± 0.9	10.4
500	150	44.9	43.9	25.2	25.2	12.4± 1.5	21.1
500	200	46.3	45.8	31.2	29.5	14.7± 1.7	22.7
500	250	54.2	53.0	39.8	37.2	18.4± 2.0	24.5
500	300	54.2	53.5	41.8	36.5	18.3± 2.0	19.4
500	350	52.3	51.4	43.9	38.9	19.3± 2.0	14.4
500	400	52.1	51.8	43.7	37.9	19.0± 2.0	7.9
500	450	47.0	46.8	39.6	29.5	14.9± 1.7	1.9
600	30	1.7	0.7	0.5	0.5	0.2± 0.2	0.1
600	100	25.0	22.8	8.4	8.4	4.1± 0.8	2.4
600	200	48.5	47.0	30.7	30.0	14.9± 1.7	8.0
600	300	50.6	49.4	40.8	38.6	19.3± 2.0	8.3
600	400	57.1	56.6	48.7	44.4	22.1± 2.2	6.1
600	500	48.5	48.5	42.7	37.4	18.6± 2.0	1.9

Table 5.5: The efficiency of the analysis cuts for different values of M_{W_R} and M_{N_R} in the *no mixing* limit. The trigger requirement has been imposed, as well as the two-electrons **match** requirement. The (data-derived) electron quality-cuts efficiencies are included only in the overall efficiency column. All objects (e's and j's) have $E_T > 25$ GeV. The expected yield was estimated assuming $g_R = g_L$, and $V_{qq'}^L = V_{qq'}^R$ using the HMRSB parton distribution functions.

M_{W_R} (GeV)	M_{N_R} (GeV)	ee (%)	eej (%)	$eejj$ (%)	$eejj$ $M_{ee} \neq Z$ (%)	Overall efficiency ϵ (%)	Expected in 100 pb^{-1} (events)
100	30	4.8	0.2	0.0	0.0	< 0.1	0.0
200	30	16.3	4.6	0.2	0.2	0.1± 0.1	14.2
200	100	10.6	6.7	2.6	0.2	0.1± 0.1	10.4
200	150	32.2	21.4	10.1	3.6	1.8± 0.5	67.4
300	30	10.6	2.6	0.0	0.0	< 0.1	0.0
300	100	19.4	12.2	4.3	4.1	2.1± 0.5	41.3
300	150	51.8	34.1	14.6	10.3	5.2± 0.9	83.7
300	200	53.5	40.3	20.4	16.8	8.3± 1.2	87.1
300	250	40.3	30.5	17.0	11.3	5.6± 0.9	21.5
400	30	13.9	2.4	0.5	0.5	0.2± 0.2	1.3
400	100	20.2	10.8	5.8	5.5	2.8± 0.6	16.2
400	150	51.8	36.7	16.3	14.9	7.4± 1.1	38.5
400	200	54.5	40.8	21.8	19.2	9.5± 1.3	41.3
400	250	60.2	46.1	26.4	24.0	12.1± 1.5	39.2
400	300	49.9	38.9	22.3	19.9	9.9± 1.3	18.8
400	350	43.9	32.9	23.5	19.0	9.7± 1.3	6.0
500	30	10.6	2.2	0.5	0.5	0.2± 0.2	0.4
500	100	15.8	10.3	6.2	6.2	3.1± 0.7	5.7
500	150	51.1	40.6	19.0	18.5	9.1± 1.2	15.6
500	200	58.1	42.2	20.9	19.4	9.6± 1.3	14.8
500	250	61.4	48.0	27.6	26.9	13.2± 1.6	17.6
500	300	61.0	45.6	31.0	29.3	14.6± 1.7	15.5
500	350	52.1	39.1	26.2	24.2	12.1± 1.5	9.0
500	400	58.8	45.6	31.4	29.5	14.7± 1.7	6.1
500	450	44.4	33.8	23.0	18.2	9.1± 1.2	1.2
600	30	11.5	1.9	0.2	0.2	0.1± 0.1	0.1
600	100	15.6	8.9	3.6	3.6	1.8± 0.5	1.1
600	200	57.8	42.7	22.3	21.8	10.7± 1.4	5.7
600	300	62.4	47.8	27.4	26.9	13.5± 1.6	5.8
600	400	60.2	45.8	28.1	27.1	13.6± 1.6	3.8
600	500	59.0	46.3	30.7	28.8	14.3± 1.7	1.4

Table 5.6: The efficiency of the analysis cuts for different values of M_{W_R} and M_{N_R} in the *large mixing* limit. The trigger requirement has been imposed, as well as the two-electrons **match** requirement. The (data-derived) electron quality-cuts efficiencies are included only in the overall efficiency column. All objects (e's and j's) have $E_T > 25$ GeV. The expected yield was estimated assuming $g_R = g_L$, and $V_{qq'}^L = V_{qq'}^R$ using the HMRSB parton distribution functions.

formed or it is not isolated (or the jets do not separate into two clusters). For larger M_{N_R}, the efficiencies for the large mixing case are always smaller than the corresponding no mixing ones. This is due to the smaller branching ratio for $N_R \rightarrow ejj$ (because the W_L leptonic channels are open) and to the fact that the jets (for most of the parameter space) tend to have smaller E_T and to be closer to each other.

In order to obtain an efficiency that is a continuous and smooth function of the masses (that will produce, in turn, smooth limit contours), a dense grid of points was generated with the **dummy** MC (every 10 GeV in M_{N_R} and 50 GeV in M_{W_R}). The efficiencies obtained were then scaled down (by 22% for the no mixing and 34% for the large mixing samples) to agree on average with the efficiencies derived from the fully simulated samples. For each value of M_{W_R}, the efficiency was then plotted versus the ratio of the masses (M_{W_R}/M_{N_R}) and fitted to a polynomial function with five parameters. For the large mixing case, the fit was performed for the points with $M_{N_R} > 80$ GeV only. The reason for this is that the overall efficiency has a dip (local minimum) due to the threshold W production (for $N_R \approx$ 80 GeV). Figure 5.5 shows parametrized efficiencies as a function of the ratio of the masses as well as contours of same efficiency for the no and large mixing cases.

Figure 5.6 shows distributions of invariant masses calculated using the MC reconstructed objects (electrons and jets) after all the cuts were applied on a no mixing sample. The invariant mass of the two electrons and the two largest E_T jets peaks at the input W_R mass, with the broadening due mostly to jet energy resolutions. Also, the invariant mass of the two jets and one of the electrons peaks at the input N mass but with an enlarged smearing due to the ambiguity in the assignment of the electron (two entries per event). Figure 5.7 shows the same distributions for the large mixing case. Here, the invariant mass of the two jets peaks at approximately 80 GeV, as expected from the W_1 decay mode of N. The large tail on the invariant mass distribution of the two jets is due to additional jets in the event (initial or final state radiation) that have larger transverse momentum than the W-decay jets.

The uncertainties on the overall efficiencies (shown in the tables) have contributions from:

- the final statistics of the MC samples,
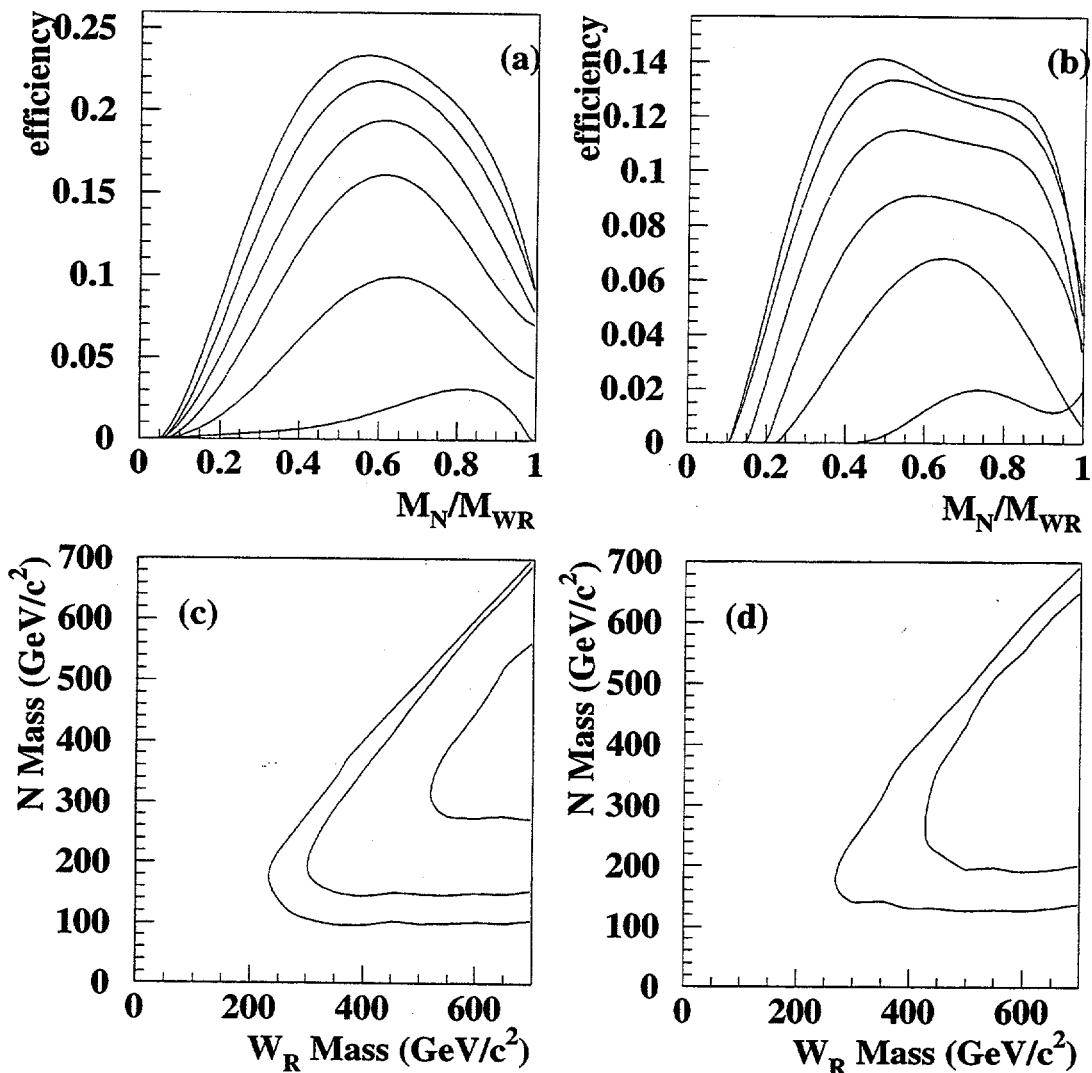
Figure 5.5: The overall efficiency of the analysis cuts. (a) and (b) show the results of the fits to the overall efficiency as a function of the ratio of the masses for the no and large mixing cases, respectively. The efficiencies are shown (from top to bottom) for M_{W_R} =700, 600, 500, 400, 300 and 200 GeV. The corresponding contours of 20%, 15%, and 5% efficiency are shown in (c) for the no mixing case. In (d) the contours of 10% and 5% efficiency are shown for the large mixing case.
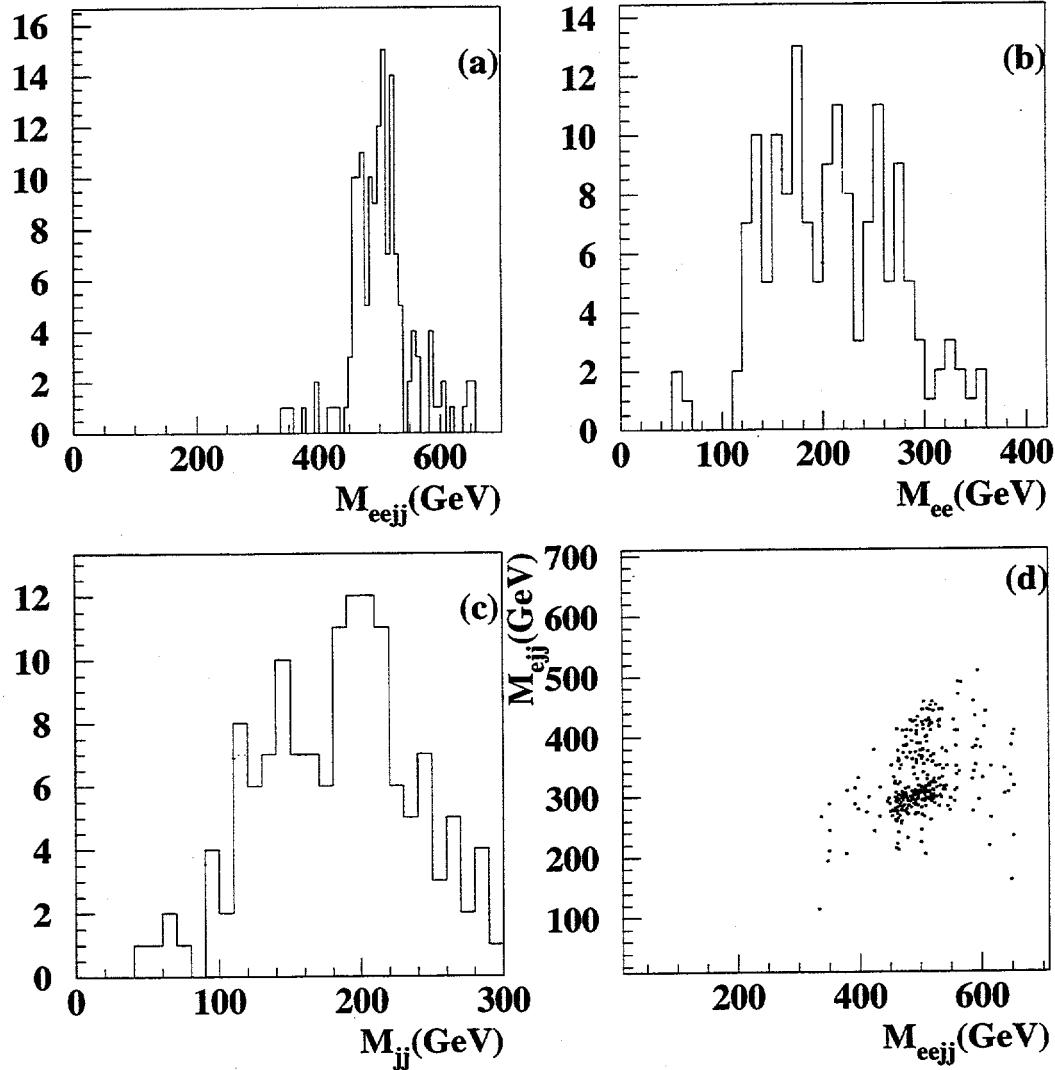
Figure 5.6: Reconstructed masses for a MC sample with $M_{W_R}=500$ GeV and $M_{N_R}=300$ GeV with *no mixing* after all the analysis cuts. Plot (a) shows M_{eejj} formed with the two matched electrons and the two largest jets, (b) shows M_{ee} (no events between 70 and 110 GeV due to the Z cut), (c) shows M_{jj} formed with the largest two jets and (d) shows a scatter plot of M_{ejj} versus M_{eejj} with two entries per event, as a result of the ambiguity in the assignment of the electron.
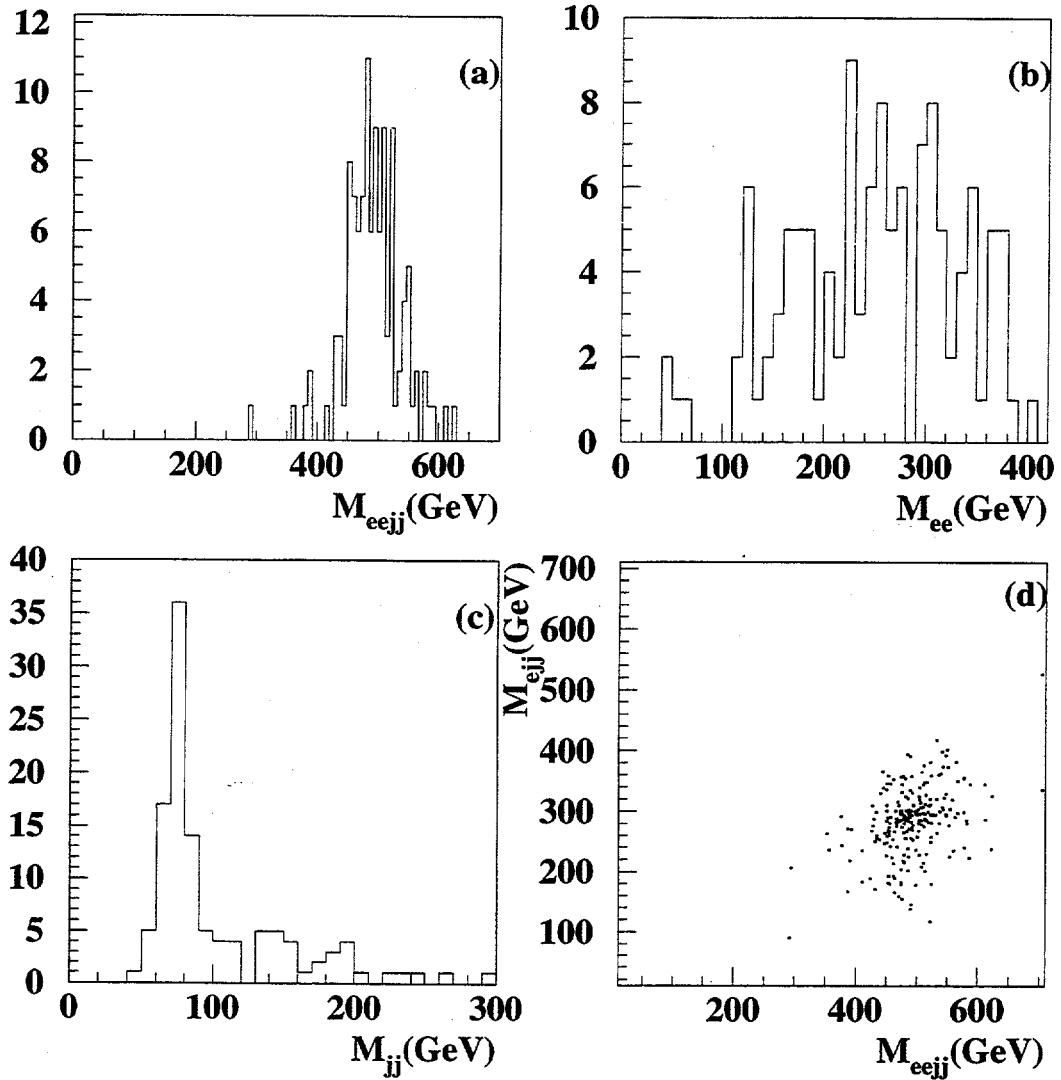
Figure 5.7: Reconstructed masses for a MC sample with M_{W_R}=500 GeV and M_{N_R}=300 GeV with *large mixing* after all the analysis cuts. Plot (a) shows M_{eejj} formed with the two matched electrons and the two largest jets, (b) shows M_{ee} (no events between 70 and 110 GeV due to the Z cut), (c) shows M_{jj} formed with the largest two jets, peaking at 80 GeV beacause the decay proceeds through mixing and (d) shows a scatter plot of M_{ejj} versus M_{eejj} with two entries per event, as a result of the ambiguity in the assignment of the electron.

- the electron identification efficiency with contributions due to the finite Z data sample available and the systematic uncertainty of the method used and

- the jet energy scale, which is determined from the data (see Sec. 4.4).

The error from the uncertainty on the jet energy scale was determined by calculating the efficiency with the same MC samples using jet energy scale corrections of $+\sigma$ and $-\sigma$ (see Fig. 4.4) with respect to the nominal correction. The changes on these efficiencies is most important for the samples that are more likely to have jets with E_T close to the cut value (25 GeV). The percentage change on the efficiency is plotted in Fig. 5.8 against the energy of N in the center of mass (CM) frame,

$$E_N^{\mathrm{CM}} = \sqrt{\left(\frac{M_{W_R}^2 - M_{N_R}^2}{2M_{W_R}}\right)^2 + M_{N_R}^2}. \tag{5.7}$$

This variable was chosen because the jet energies are expected to scale with it. As can be seen from the figure, the efficiency uncertainty (due to the jets scale uncertainty) is larger for smaller E_N values and very small for large E_N (for these, most of the jets are well above threshold). The value of the relative error on the efficiency was then chosen to be 10% for samples with $E_N < 200$ GeV, 5% for $200 < E_N < 400$ GeV and 2% for $E_N > 400$ GeV.

The choice of parton distribtion functions (PDF) could, in principle, add an additional uncertainty to the overall efficiency. Different PDF's lead to slightly different longitudinal momentum distribution of the produced W_R. This, in conjunction with a non uniform detector response (as is the case for electrons, because of the lack of EM coverage in the inter-cryostat region) can cause a PDF dependent overall efficiency. In order to investigate this, five dummy MC samples were generated with different PDF sets: CTEQ 2M (which was the set used for the fully simulated samples), DO 1.1, HMRSB, MRS D-' and GRV HO. The spread on the measured efficiencies ($\frac{\mathrm{Max-Min}}{2}$) was less than 2.5% and was only limited by the statistics of the samples used (4000 events each). Therefore, no additional error from this source was added to the efficiency.
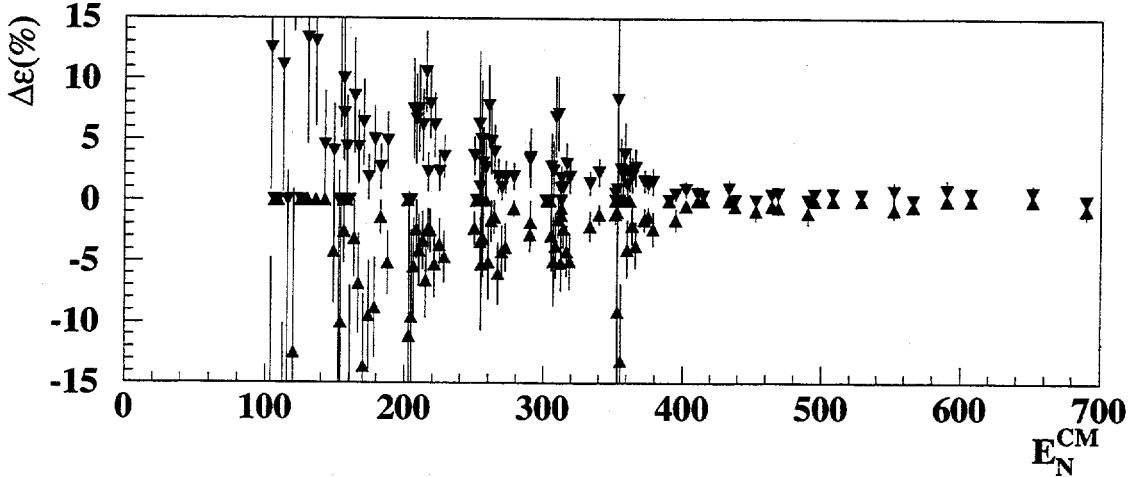
Figure 5.8: Percentage change of the efficiency using the nominal jet energy scale plus (minus) one σ of its error with respect to the nominal correction. The change is plotted against the N's CM energy E_N because the jet energies are expected to scale with it.

5.2.3 Background Estimation

Two events (see Sec. 5.2.1) passed all the analysis cuts applied and therefore were considered W_R candidate events. It is therefore important to understand and evaluate the background processes that can mimic such a signal. These can be divided into two subgroups, physics backgrounds and fake backgrounds.

The most important physics backgrounds are $Z, \gamma^* \to ee$ production in conjunction with jets (Z+jets), $t\bar{t}$ production with the two W bosons (from the t decays) each decaying into an electron and a neutrino, and W boson pair production (WW). For the Z+jets background, the Z mass cut is very effective at removing most of the events. However, the Breit-Wigner (Lorentzian) shape of the Z resonance has large tails, well beyond the window cut imposed. In order to calculate the expected yield from this process, 1,000,000 events of $Z, \gamma^* \to ee$ MC with a simple detector simulation (including energy resolution, vertex position smearing and fiducial acceptance) were used. The input mass (M_{ee}) spectrum to this MC was generated with PYTHIA (Z, γ^* process that includes interference). This MC

sample was used only to determine the ratio of events above(R_{hi}) and below(R_{low}) the Z window to the number within the window. Figure 5.9 shows the M_{ee} spectrum after the fiducial and kinematic cuts were applied on the two electrons for the whole sample and for the events with a large transverse momentum Z, $p_T^Z > 25$ GeV (that enhances Z+jets-like topologies). The second plot (labeled b in the figure) has 3.1% below the Z mass window and 3.5% above it. The corresponding values for a $p_T^Z > 40$ GeV cut are 4.1% below and 4.0% above. The first pair of values was used to determine the tail-to-peak ratios, while the difference between the ratios for the two cuts (25 and 40 GeV) was used to estimate the error in this quantities. Therefore, the values $R_{low} = 3.1 \pm 1.0\%$ and $R_{hi} = 3.5 \pm 0.5\%$ are used as the below and above ratios, respectively. Then, to obtain the expected number of events from Z+jets in the tails, the number of observed events inside the Z mass window (after subtracting the other background sources described in the following paragraphs) is multiplied by these tail-to-peak ratios. The error on the expected number of events has contributions from the uncertainty in the ratios and from the statistical error on the number of events in the peak.

For the $t\bar{t}$ background, fully simulated ISAJET MC events were used as well as the DØ measured [34] production cross section 6.4 ± 2.2 pb and the theoretical branching ratio (1/81). This MC sample contains also the contribution to the di-electron signal from events with one or two $\tau \to e\nu\nu$. The calculation was done assuming a top quark mass of 160 GeV. The dependence of the acceptance on the exact value of the top quark mass is small and was therefore ignored. Figure 5.10 shows the invariant mass of the two electrons and the missing transverse energy ($\not{E}_T$) for the $t\bar{t}$ events passing the fiducial and kinematic cuts.

The last physics background studied was W boson pair production. The SM cross section times branching ratio (both W's decaying into the electron channel) has been calculated to be 0.12 pb [44]. The expected yield from this source gets substantially reduced by the two jets requirement. Again, a fully simulated PYTHIA MC sample with 2500 events of $WW \to ee$ was used to estimate the number of events that would survive all the imposed cuts.

The fake backgrounds are processes that do not lead to a final state with two electrons and two jets, but are reconstructed as such. For instance, ocasionally, a hadronic jet can
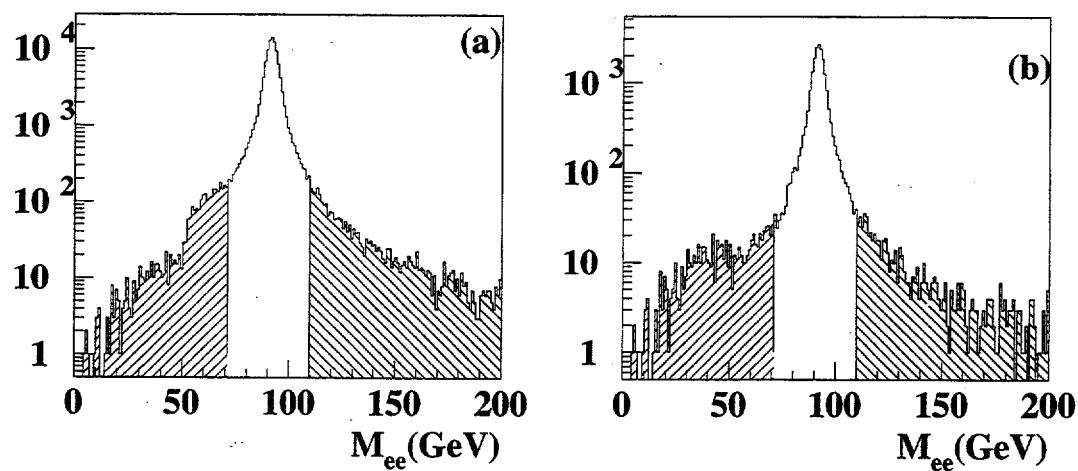
**Figure 5.9:** (a)Invariant mass of the two electrons in $Z, \gamma \rightarrow ee$ toy MC after the fiducial and kinematic cuts on the two electrons. (b) The same as (a) but requiring $p_T^Z > 25$ GeV to enhance Z+jets-like topologies. The ratios of the shaded areas to the entire distribution times the number of observed events in the peak region (in the data) gives the number of expected Z+jets events outside the peak.
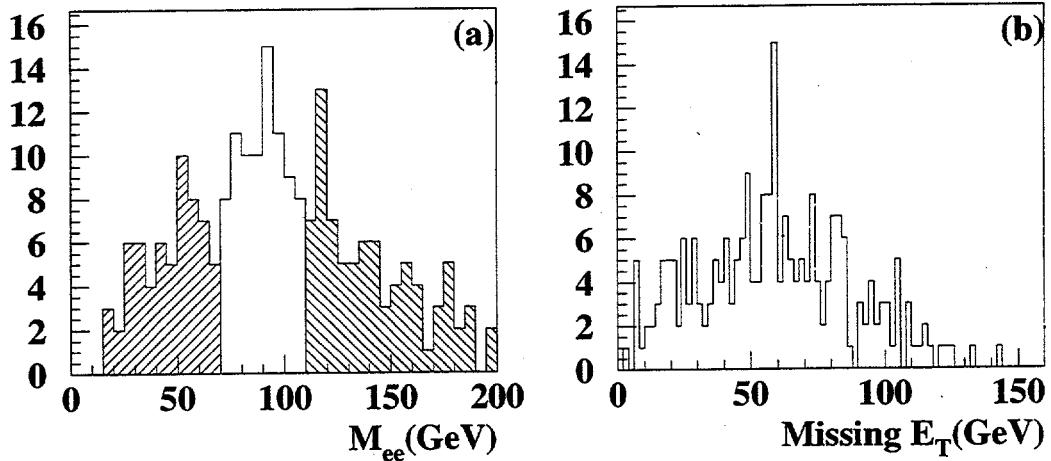
Figure 5.10: (a)Invariant mass of the two electrons in $t\bar{t} \to ee + 2$ or more jets MC after the fiducial and kinematic cuts. The shaded areas contribute to the background of the W_R signal. (b) The $\not{E}_T$ distribution for those events.

be mistakenly reconstructed as an electron and therefore it will be called a fake electron. A fake electron is produced when a jet for which most of its energy is carried by one or more π^0 mesons, producing a highly electromagnetic calorimeter shower, is overlapped by a soft charged particle (like a $\pi^\pm$), giving a track in the road of an EM cluster. Photon conversions (e.g. from a π^0 decay) can also produce fake electrons because they shower like an electron and have one or more tracks in the road (see Sec. 4.1).

The main source of fake background events is expected to be from QCD multijet production. This process has a very large cross section and therefore even a minuscule fake electron probability will contribute significantly to our sample. The calculation of the fake background was done separately for Run Ia and Run Ib. For Run Ia, the calculation was performed in two steps. First, the probability for a jet to be reconstructed as an electron (with the electron identification criteria used in this analysis) was calculated. To this effect, a sample of collider data events with a highly electromagnetic jet with $E_T > 25$ GeV and an additional hadronic jet with $E_T > 25$ GeV was selected. All the electron identification

single electron	$P_{j \to e}$ (10^{-4})	two-electron combination	$P_{j \to e} \cdot P_{j \to e}$ (10^{-8})
CC tight	1.12 ± 0.05	CC-CC	1.26 ± 0.11
EC tight	3.14 ± 0.14	CC-EC	9.05 ± 0.27
EC loose	8.06 ± 0.29	EC-EC	40.7 ± 3.03

Table 5.7: The probabilities for a jet to fake an electron using the electron identification criteria used in this analysis. The two-electron combinations include the contribution from allowing one loose electron in the EC. The errors quoted are only statistical and are dominated by the number of fake electrons in the sample: 536 in CC; 1811 (loose) and 706 (tight) in EC.

cuts were then applied on the highly electromagnetic jet. Most of the events passing these criteria are due to fake electrons. A small percentage (about 6%) of real W+jets events are removed from the sample by requiring $\not{E}_T < 20$ GeV. Real Z events (about 12%), with one electron reconstructed as a jet, are removed by requiring that the hadronic jet does not have a large EM fraction if the electron-jet mass is consistent with the Z hypothesis. A sample of QCD dijet events (that triggered on one jet with $E_T > 15$ GeV) was then used to obtain the number of events that had two jets with $E_T > 25$ GeV (without the highly EM jet requirement). The fake electron probability is then:

$$P_{j \to e} = \frac{N_{\text{fake}}}{N_{\text{jj}}} \frac{\mathcal{L}_{\text{jj}}}{\mathcal{L}_{\text{fake}}}, \tag{5.8}$$

where N_{fake} and N_{jj} are the number of fake electron events and two jet events in the fake and QCD samples respectively. $\mathcal{L}_{\text{fake}}$ and $\mathcal{L}_{\text{jj}}$ are the integrated luminosities of both samples. The values of the fake electron probabilities were calculated separately for CC and EC electrons and for the two-electron combinations with the cuts used in this analysis (allowing one loose electron in the forward region) and are shown in table 5.7.

The QCD sample was used one more time in the estimation of the fake background in the sample. This time, events were required to have at least three jets with $E_T > 25$ GeV in order to correctly emulate the topology of fake eej and $eejj$ events. For each event, all the two-jet combinations were used to fill a histogram of the invariant mass of the pair with a weight corresponding to the fake probability (CC-CC, CC-EC and EC-EC). Finally,

the invariant mass cut $M_{jj} < 70$ GeV or $M_{jj} > 110$ GeV was applied to obtain (given the luminosity of the QCD sample) the expected number of fake events in the Run Ia W_R sample.

To calculate the fake background in the Run Ib sample, the invariant mass spectrum of the pair of EM jets in events with four or more jets was scaled by a factor determined from a two-component fit to the inclusive dielectron data using the dielectron invariant mass spectrum from Z, γ^* MC and the measured inclusive di-EM-jet invariant mass. The details of the procedure are explained in what follows. From the Run Ib sample of events with two EM energy clusters, events that passed the trigger requirement and for which the two EM clusters had an EM fraction smaller than 0.95 were selected. The requirement of the small EM energy fraction ensures a negligible true electron content in this sample and was therefore used to estimate the shape of the QCD background in the inclusive dielectron data. The same kinematic and fiducial cuts were applied to the two EM jets as for the electrons in the signal sample. The invariant mass of the two EM jets was then computed for this inclusive sample, for the subset of events that had one or more additional jets ($E_T > 25$ GeV and in the same fiducial region) and for the subset of events with two or more additional jets. The inclusive dielectron invariant mass spectrum was obtained from the same parent sample, but requiring the electron identification criteria used for the signal (namely, two good electrons). This spectrum was then fitted to the sum of the QCD background (inclusive di-EM-jets) and the Z, γ^* MC. Since the goal of this procedure was to determine the QCD fraction in the tails of the M_{ee} distribution and because it is difficult to precisely simulate the peak region due to instrumental/reconstruction uncertainties, the peak region ($70 < M_{ee} < 110$ GeV) was collapsed into a single bin. The two plots in Fig. 5.11 show the result of this fit. The χ^2 per degree of freedom (for the collapsed histogram) is 0.9. The factor by which the QCD histogram was multiplied (a parameter of the fit) was 0.051 ± 0.012. This factor was then used to scale the QCD distributions for the samples with one and more jets and two or more jets to determine the expected background in the eej and $eejj$ samples, repectively.

For all the background processes studied, estimates of the yields above and below the Z peak region using the same cuts as in the collider data analysis are shown in table 5.8. Also shown are the number of events observed in the data sample. The agreement between
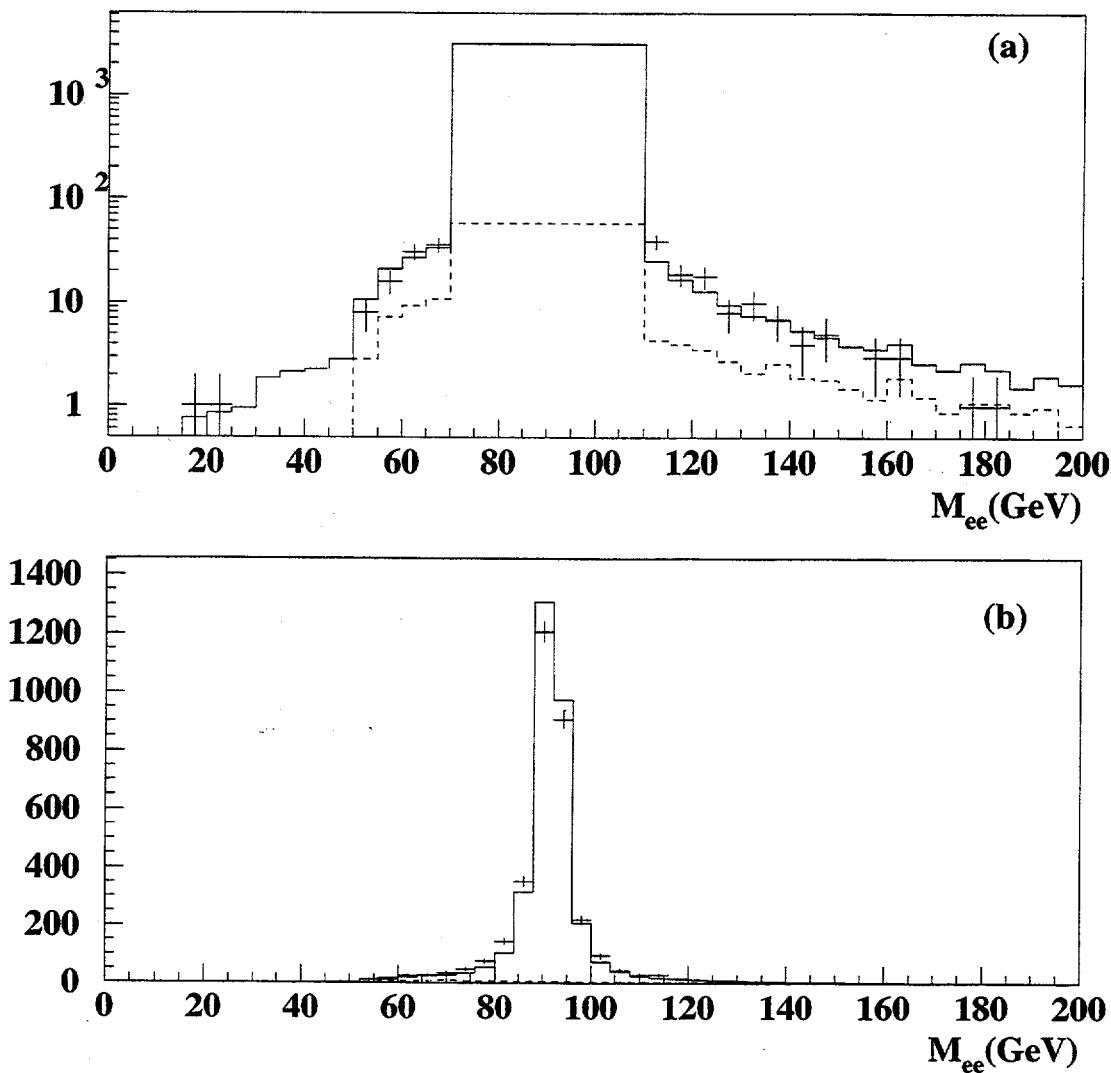
Figure 5.11: Fit to the dielectron data (points) to determine the QCD background (dashed) in the Run Ib sample. The solid histogram is sum of the Z, γ^* MC and the QCD background. In (a) the peak region was collapsed into one bin; (b) shows the same fit for the uncollapsed peak, with the same fitting parameters as (a).

Background	Event yield for 79.0 pb^{-1}		
Process	$M_{ee} < 70$ GeV	$M_{ee} > 110$ GeV	$M_{ee} < 70$ or $M_{ee} > 110$ GeV
$Z, \gamma \to ee + X$	0.59 ± 0.23	0.67 ± 0.17	1.26 ± 0.34
$t\bar{t}(160) \to ee + X$	0.18 ± 0.10	0.25 ± 0.12	0.43 ± 0.16
$WW \to ee + X$	< 0.01	0.01 ± 0.01	0.01 ± 0.01
fake	0.33 ± 0.18	1.05 ± 0.47	1.38 ± 0.68
Total	1.10 ± 0.31	1.98 ± 0.60	3.08 ± 0.78
Observed	0	2	2

Table 5.8: The expected background for the two electrons plus two jets signal. The observed number of events is consistent with the estimated background.

Background	Event yield for 79.0 pb^{-1}		
Process	$M_{ee} < 70$ GeV	$M_{ee} > 110$ GeV	$M_{ee} < 70$ or $M_{ee} > 110$ GeV
$Z, \gamma \to ee + X$	6.03 ± 1.97	6.81 ± 1.07	12.84 ± 2.31
$t\bar{t}(160) \to ee + X$	0.25 ± 0.10	0.36 ± 0.15	0.61 ± 0.35
$WW \to ee + X$	0.05 ± 0.01	0.08 ± 0.02	0.13 ± 0.02
fake	3.87 ± 1.60	6.03 ± 2.46	9.90 ± 4.01
Total Backgrounds	10.20 ± 2.54	13.28 ± 2.69	23.48 ± 4.64
Observed	8	15	23

Table 5.9: The expected backgrounds with two electrons plus one or more jets.

the expected number of background events and the observed number of events is good; the Poisson probability of observing 2 events from an expected 3.08 is 22%, while the probability of observing 2 or less is approximately 40%. As an additional verification of the background estimation, the same calculations were done requiring only one or more jets in addition to the two electrons. Table 5.9 shows the results of these estimations as well as the observed number of events.

5.2.4 Limits

The search for events with two electrons and two jets yielded two events observed in the data with an estimated background of 3.08 ± 0.78. There is therefore no evidence for W_R

decaying into an electron and a massive neutrino with decays as described in Sec. 2.2.2. Given the efficiency for detecting the signal and the integrated luminosity of the data sample used, upper limits on the cross section times branching ratio can be obtained. These cross section upper limits can, in turn, be converted into mass limits in the M_{W_R}-M_{N_R} plane after assuming some theoretical W_R production cross section and branching ratio into the eN channel.

Since both the signal and the backgrounds are Poisson processes, the 95% confidence level (CL) upper limit on the number of signal events is obtained using [45]:

$$CL = 1 - \frac{e^{-(\mu_B + U)} \sum_{n=0}^{n_o} \frac{(\mu_B + U)^n}{n!}}{e^{-(\mu_B)} \sum_{n=0}^{n_o} \frac{\mu_B^n}{n!}}, \tag{5.9}$$

where CL is the desired confidence level, μ_B is the expected background, n_o is the number of observed events and U is the upper limit of signal events with that confidence level. Using equation 5.9 for $n_o = 2$, $\mu_B = 3.08$ and $CL = 0.95$ gives $U = 4.418$. In order to take into account the uncertainty on the expected background, the equation was solved after integrating over μ_B with a Gaussian weight (with mean μ_B and width σ_{μ_B}). Using $\sigma_{\mu_B} = 0.78$, one then obtains a degraded upper limit of $U_b = 4.570$.

The uncertainties on the integrated luminosity and on the overall efficiency tend to further degrade this upper limit. Those are taken into account using a generalized version of the Poisson limit [46]:

$$U_{sb} = U_b \left(1 + U_b \frac{\sigma_s^2}{2} \frac{U_b + \mu_B - n_o}{U_b + \mu_B} \right), \tag{5.10}$$

where

$$\sigma_s^2 = \left(\frac{\sigma \mathcal{L}_{int}}{\mathcal{L}_{int}} \right)^2 + \left(\frac{\sigma \epsilon}{\epsilon} \right)^2 \tag{5.11}$$

and U_{sb} is the final 95% CL upper limit on the number of signal events that takes into account the uncertainties on the estimated background, the efficiency and the integrated luminosity. The cross section times branching fraction upper limit is then:

$$(\sigma B)_{95\%CL} = \frac{U_{sb}}{\epsilon \mathcal{L}_{int}}, \tag{5.12}$$

where ϵ is the overall efficiency (including the acceptance) for given masses of W_R and N and $\mathcal{L}_{int}$ is the integrated luminosity of the sample.

A more rigorous method of calculating the limit, using fully consistent Bayesian probabilities to incorporate the uncertainties in the background and the effect of systematic errors, led to results identical to the ones quoted here.

Figures 5.12 and 5.13 show the cross section times branching fraction limits as a function of the W_R mass for the no mixing and large mixing cases, respectively. For each case the limit is plotted for four different N masses. The theoretical cross section times branching ratio is also shown assuming $g_L = g_R$ and $V_{qq'}^L = V_{qq'}^R$. The points for which the cross section limit is below the theoretical value are ruled out at the 95% CL.

In order to illustrate the dependence of the mass limits on the parameters of the theory, the cross section times branching fraction is plotted in Fig. 5.14 for different values of the coupling constant and the right-handed quark-mixing matrix. A right-handed CKM matrix of the form III (see section 2.4.1) with $V_{ud}^R = 0$ and $V_{us}^R = 1$ was chosen to illustrate the effect resulting from the variation of these free parameters.

The excluded region of the parameter space from this analysis is shown in Fig. 5.15 for the no mixing case and in Fig. 5.16 for the large mixing case. The regions inside the contours are ruled out at the 95% C.L. The contours are shown for different values of the coupling constant and the right-handed CKM matrix. As expected, for low neutrino masses (below 100 GeV) this method does not yield useful limits. The analysis in the next section targets that region of the parameter space in particular.
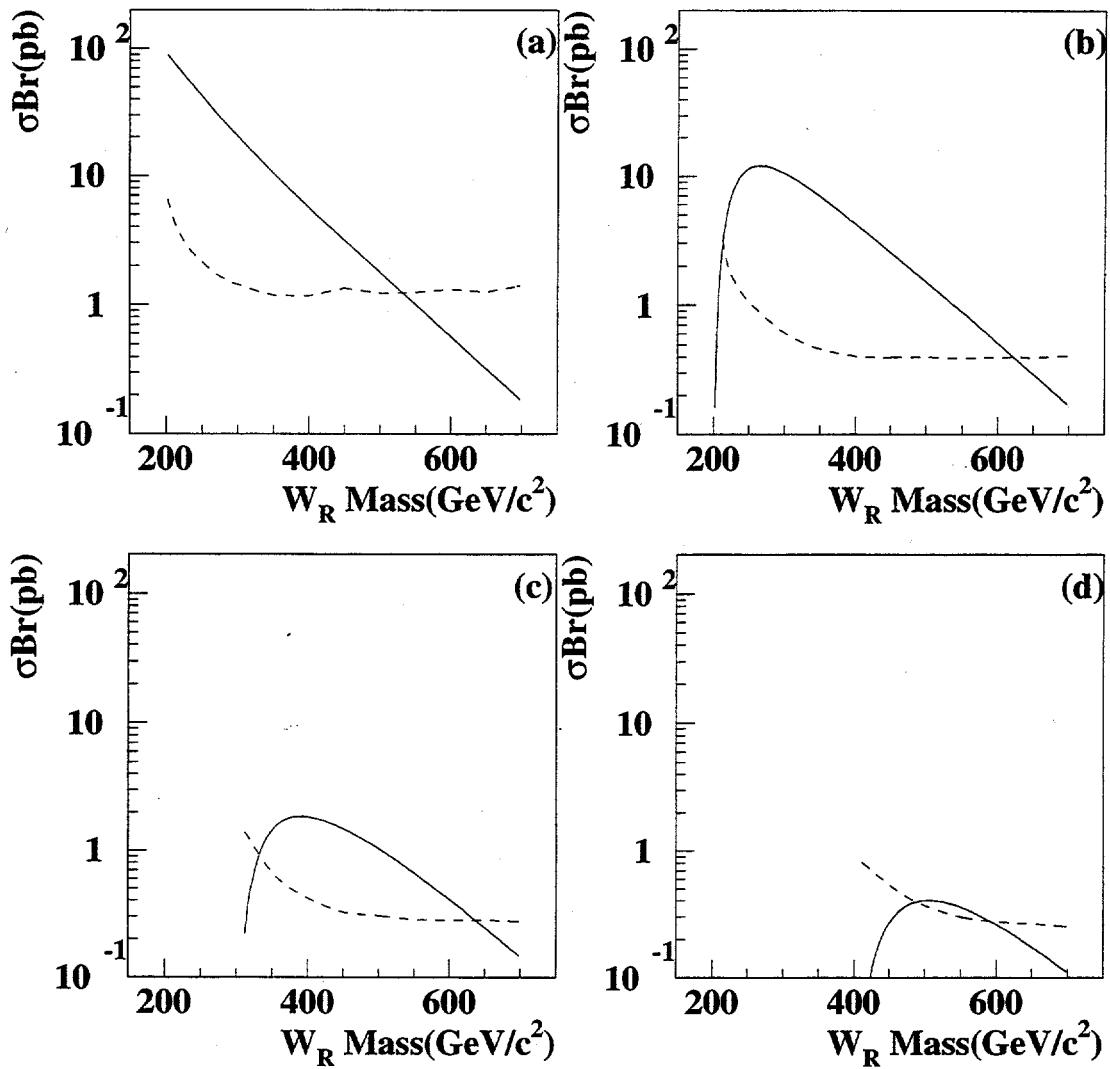
Figure 5.12: The 95% CL limit on the cross section times branching fraction of $W_R \to eejj$ for the *no mixing* case. The limits (dashed) and theoretical σB (solid) are shown for (a) $M_{N_R} = 100$, (b) $M_{N_R} = 200$, (c) $M_{N_R} = 300$ and (d) $M_{N_R} = 400$ GeV. The cross section was obtained using the MRS(H) PDF set, assuming that $g_L = g_R$ and $V_{qq'}^L = V_{qq'}^R$.
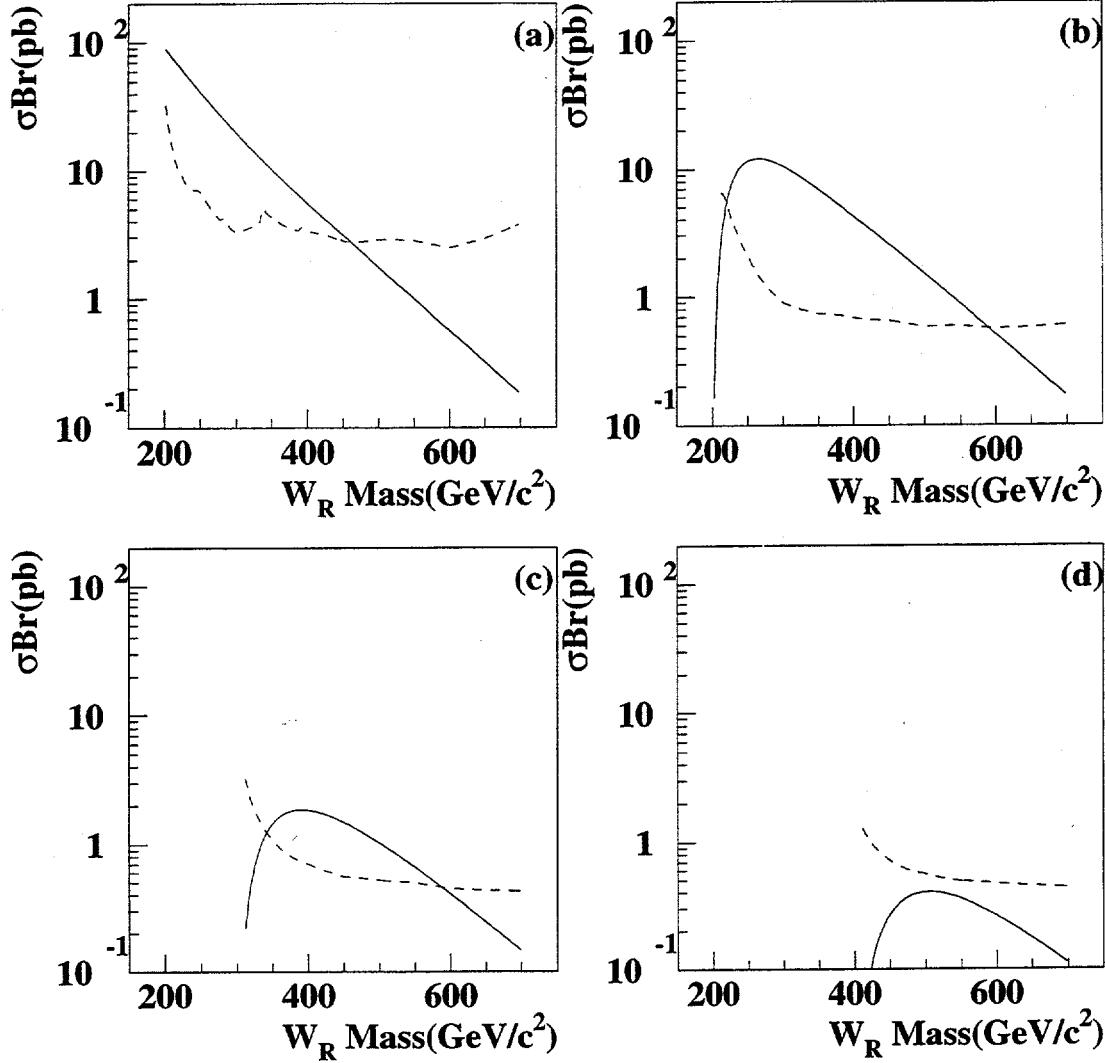
Figure 5.13: The 95% CL limit on the cross section times branching fraction of $W_R \rightarrow eejj$ for the *large mixing* case. The limits (dashed) and theoretical σB (solid) are shown for (a) $M_{N_R} = 100$, (b) $M_{N_R} = 200$, (c) $M_{N_R} = 300$ and (d) $M_{N_R} = 400$ GeV. The cross section was obtained using the MRS(H) PDF set, assuming that $g_L = g_R$ and $V_{qq'}^L = V_{qq'}^R$.
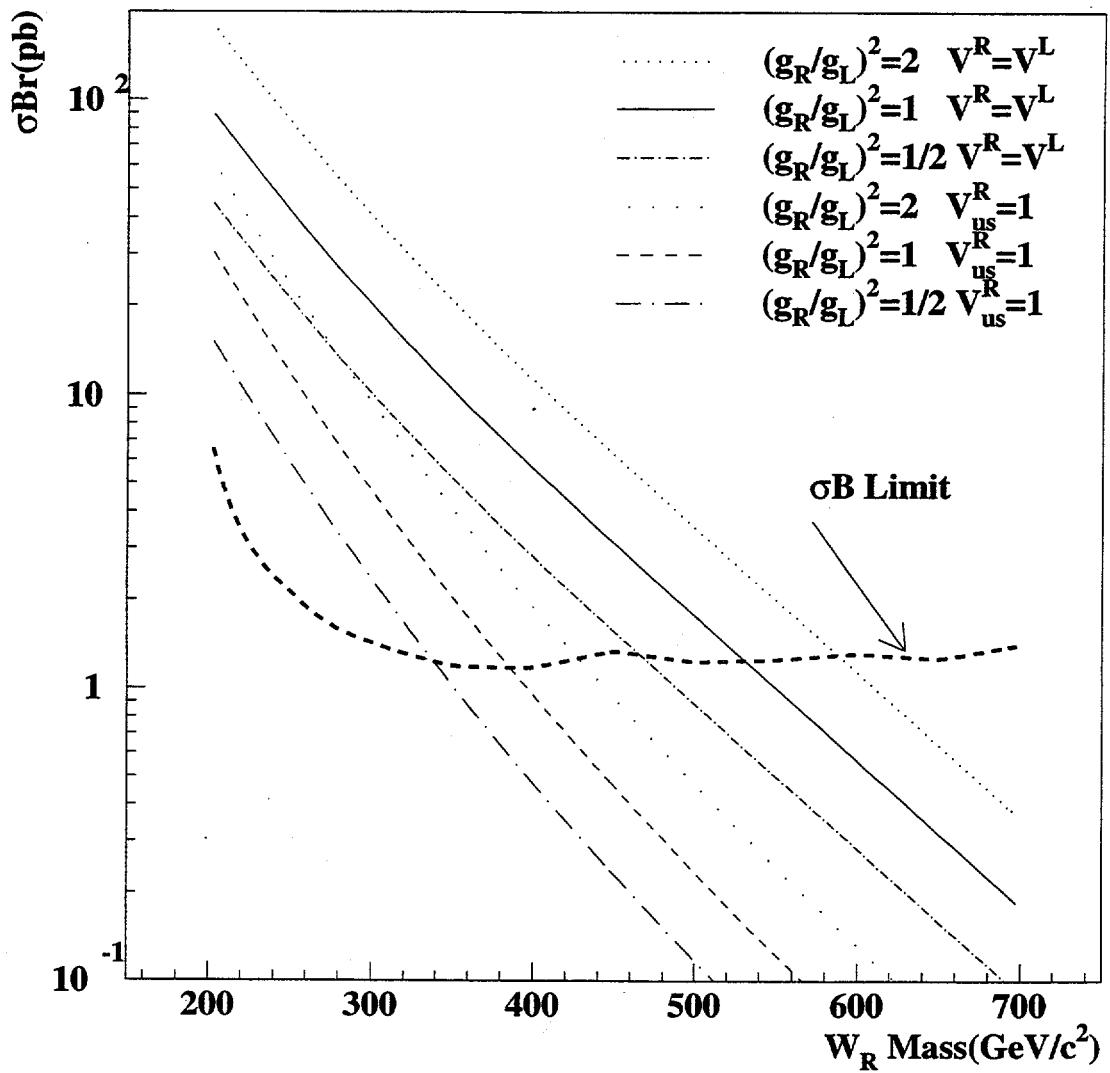
Figure 5.14: Effect of the model parameters on the mass limits. σB is shown for different values of the right-handed CKM matrix and the coupling constant. The 95% CL limit on the cross section times branching fraction for $M_{N_R} = 100$ GeV with no mixing is shown (thick-dashed) to illustrate the effect of the model parameters on the mass limits.
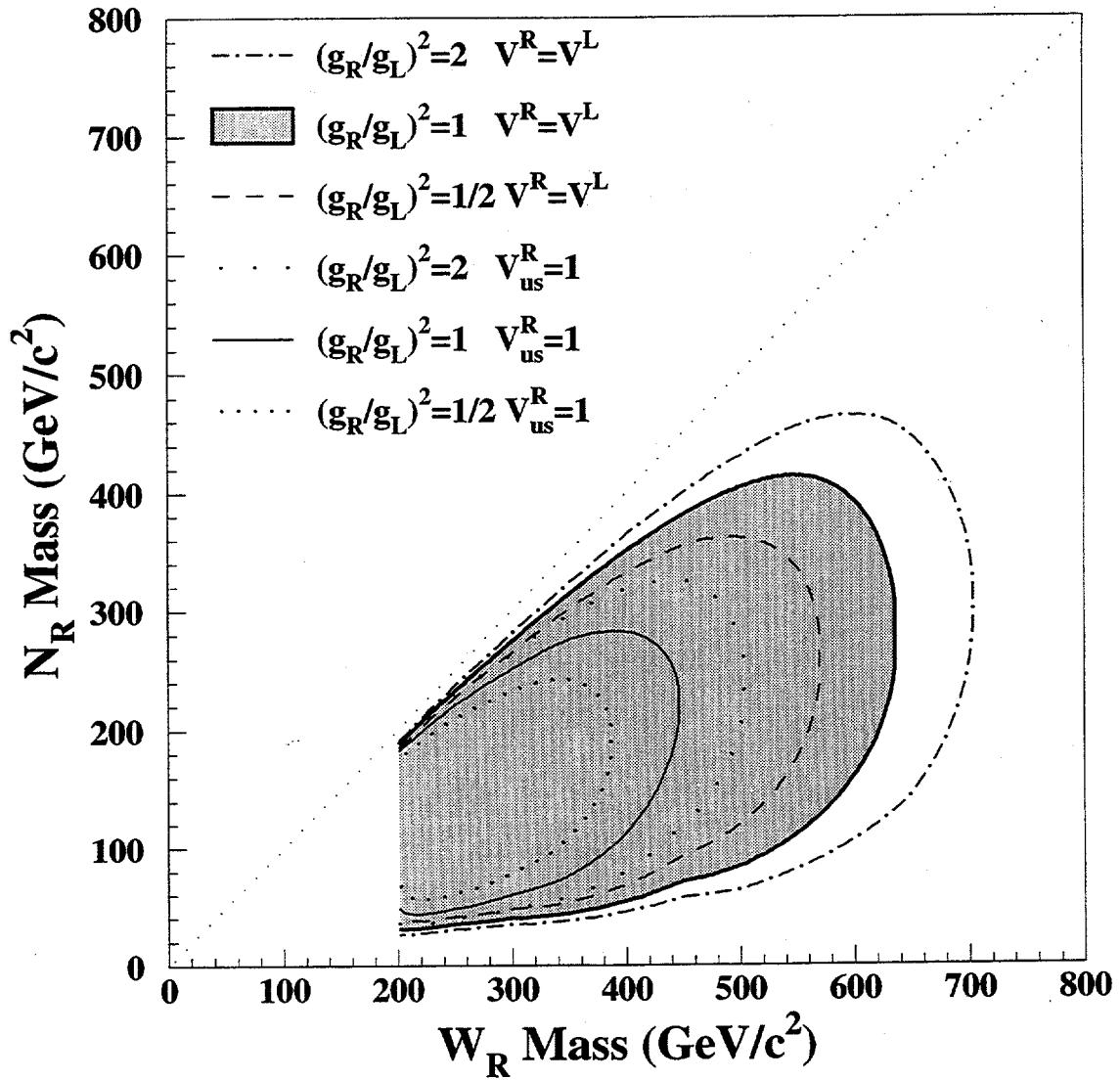
Figure 5.15: Excluded region of masses at the 95% C.L. from the $eejj$ search for the *no mixing* case. The region inside the lines are excluded for (shaded) $V_{qq'}^L = V_{qq'}^R$ and (solid) $V_{us}^R = 1$, assuming $(g_R/g_L)^2 = 1$. For each CKM matrix case, the excluded regions corresponding to $(g_R/g_L)^2 = 0.5$ and $(g_R/g_L)^2 = 2$ are also shown. The $M_{W_R} = M_{N_R}$ line represents the kinematical limit for the $W_R \to eN$ decay.
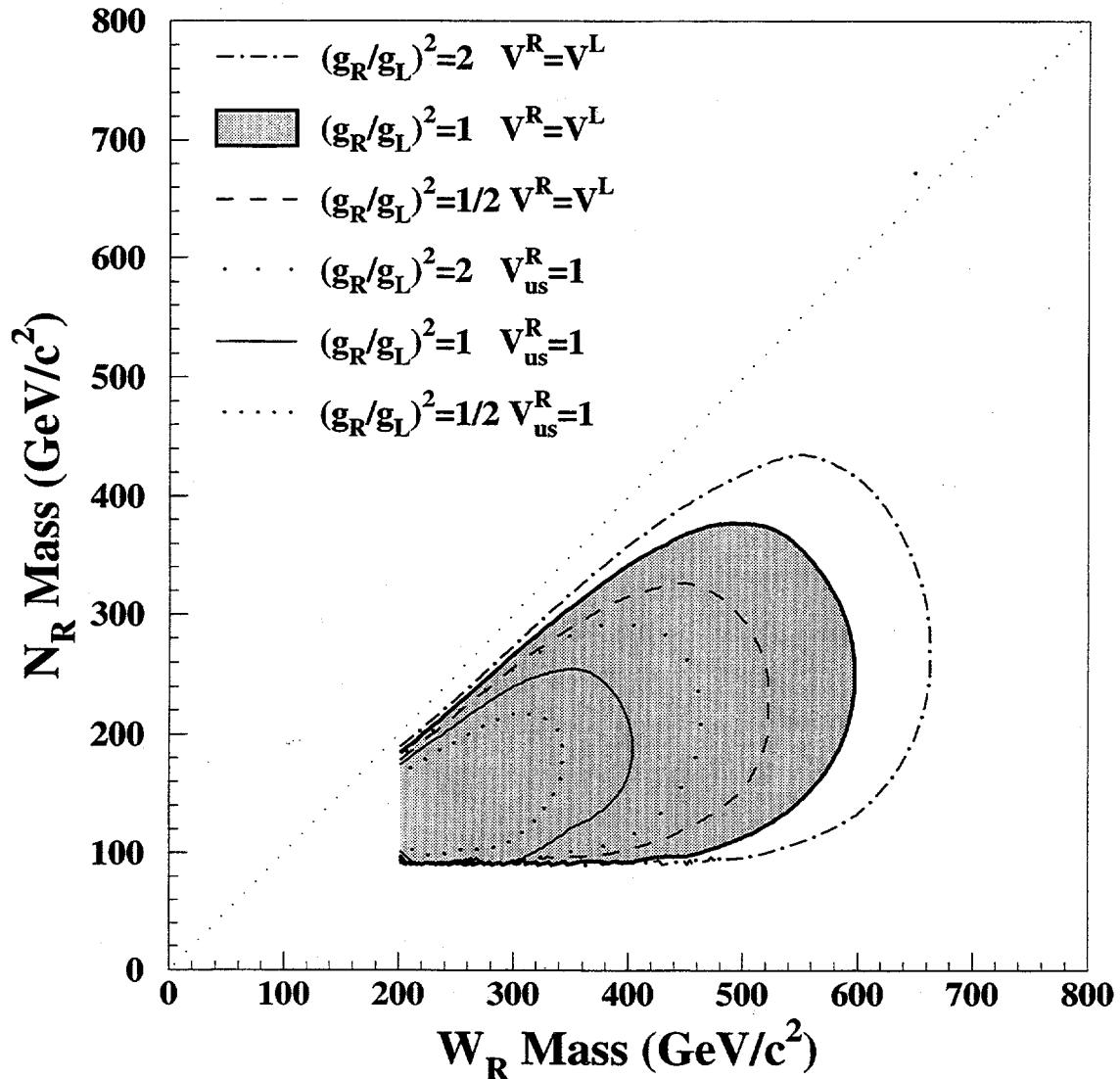
Figure 5.16: Excluded region of masses at the 95% C.L. from the $eejj$ search for the *large mixing* case. The region inside the lines are excluded for (shaded) $V^L_{qq'} = V^R_{qq'}$ and (solid) $V^R_{us} = 1$, assuming $(g_R/g_L)^2 = 1$. For each CKM matrix case, the excluded regions corresponding to $(g_R/g_L)^2 = 0.5$ and $(g_R/g_L)^2 = 2$ are also shown. The $M_{W_R} = M_{N_R}$ line represents the kinematical limit for the $W_R \to eN$ decay.

5.3 The Shape Analysis Search: $e + X$

In this section, the search for a Jacobian peak in the single electron E_T spectrum is described. Such a peak is characteristic of two-body decays such as in $W_R^\pm \to e_1^\pm N$. A sample of events with at least one central electron with large E_T is first selected. Since no other requirements are imposed on the events, other than the presence of the large E_T electron, very strict electron identification criteria are used to eliminate the reducible background (fake electrons). The irreducible background (real isolated electrons) is due primarily to W and Z boson production. The E_T and transverse mass (of the electron and the $\not{E}_T$ in the event) distributions are simultaneously fit to a combination of W/Z MC and QCD background. Limits on the size of a W_R component in the E_T distribution only are obtained. Even though this search was performed with a specific model for the N decays in mind (see Sec. 2.2.2), the result is valid irrespective of that assumption. This is a consequence of using the transverse energy distribution of the electron in $W_R \to eN$ as the signature. This distribution depends only on the masses of the W_R and N (see Sec. 2.3) and not on the decay mode, lifetime or interactions of the right-handed neutrino N. This search strategy was chosen with the goal of making the analysis sensitive to a leptonically decaying W_R, without the strong assumptions on the nature of the right-handed neutrinos and their decays used in previous W_R searches.

5.3.1 Data Selection

A data sample from both run Ia (complete) and run Ib (incomplete) with an integrated luminosity of $\mathcal{L}_{int} = (74.4 \pm 4.1)$ pb^{-1} was analyzed. The effective integrated luminosity for this analysis is slightly different than the one described in the previous sections. Two factors contribute to this difference. First, the Level 1 single electron trigger in Run Ib had an additional hardware veto to avoid junk events due to the Main Ring activity, decreasing the effective luminosity. Second, the data selection for this search was done at a later date and therefore some additional data had been fully processed for offline analysis.

The parent sample was the set of 45,656 events that had at least one electromagnetic cluster with $E_T > 50$ GeV (before EM scale correction) and with a track in the road (see

Sec. 4.1). Most events in this sample are due to fake electrons.

In order to enhance the true electron content in the sample, the following requirements were imposed:

Trigger: Events from run Ia and run Ib had to pass a hardware-level trigger (Level 1) requiring one EM trigger tower with $E_T > 10$ GeV. For part of run Ib there was an additional and more sophisticated trigger level (Level 1.5), requiring two adjacent EM towers with a total of $E_T > 15$ GeV and with EM fraction $> 85\%$. In run Ia, at the software level trigger (Level 2), an EM cluster with $E_T > 20$ GeV, some isolation and good electron shape (see Sec. 3.6) was required (ELE_HIGH). In run Ib that same filter was not kept unprescaled because of its large rate. Therefore, a filter with a $E_T > 40$ GeV threshold and looser shape requirements was used (EM1_GIS_HIGH).

Electron: One golden electron with $E_T > 55$ GeV (corrected energy) must be found in the event. A golden electron is an energy cluster (see Sec. 4.1 for details on these quantities):

- with high electromagnetic fraction: EMF > 0.95,

- in the central region defined by $|\eta_{det}| < 1.1$,

- with shape consistent with that of an electron: H-matrix $\chi^2 < 50$,

- that is isolated: ISO < 0.05,

- with a track matching in ϕ and θ with significance (TMS) < 2.5 and

- with a track ionization consistent with a single minimum ionizing particle: $\frac{dE}{dx} < 1.5$.

These electron identification criteria are more stringent than the ones used in the previous analysis. The electromagnetic fraction cut is very efficient for high energy electrons because of the large depth in radiation lengths (20.5 X_0) of the EM calorimeter and its hermeticity. To verify this, a fully simulated MC sample (with the detailed geometry of the uranium plates and liquid argon gaps) of 400 GeV single electrons was used. The efficiency of the EMF cut was found to be greater than 95% for these very large energy MC electrons.
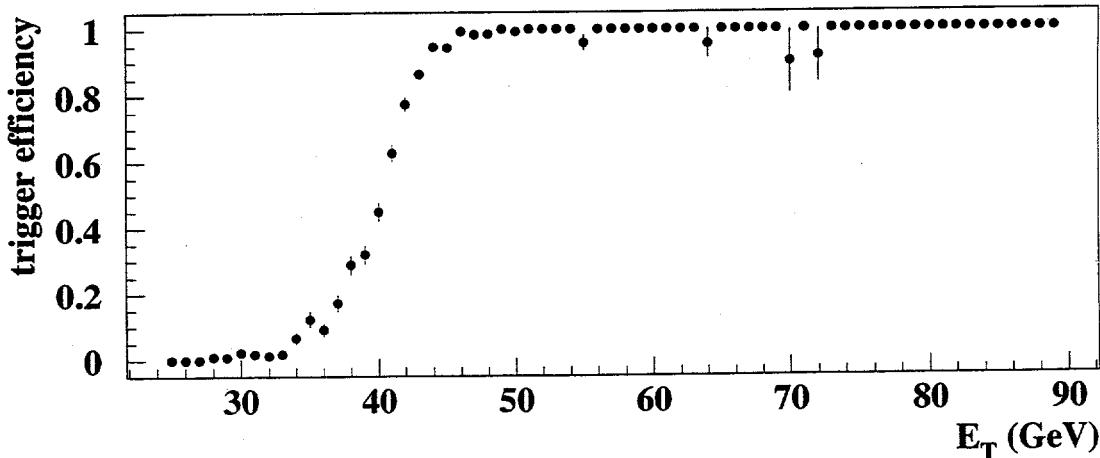
Figure 5.17: The trigger efficiency for the Run Ib filter. This filter has a 40 GeV threshold and it becomes fully efficient at 50 GeV.

Additional evidence for this (expected) large efficiency comes from test beam measurements of electrons with up to 150 GeV.

Only central electrons are used because the electron identification is significantly better in this region. In addition, the W_R signal is preferentially central as well. Since a shape analysis is going to be performed on these data, it is important to demonstrate that the triggers are fully efficient (flat) at the the cut value (55 GeV), and will therefore not modify the shape of the spectrum. This is specially important because the backgrounds for this search were simulated using a simple detector simulation that could not be used to reproduce the details of the trigger requirements. The run Ia filter, with a 20 GeV threshold, is safely below the cut value and it is therefore fully efficient. On the other hand, for run Ib, the filter threshold of 40 GeV is close to the cut value. Figure 5.17 shows the turn-on curve for the run Ib filter generated using a lower threshold (but prescaled) filter. Since the filter becomes fully efficient at approximately 50 GeV, no distorting effect is expected.

After these very stringent requirements, 1597 events remain in the sample. The transverse energy, missing transverse energy, transverse mass (formed with the electron and $\not{E}_T$)

and the invariant mass of the two electrons (if there is a second electron in the event) for these events are shown in Fig. 5.18. The transverse energy distribution falls nearly exponentially and no evident additional structure (such as bumps) is observed. The large peaks in the $\not{E}_T$ and M_T distributions are due to real W boson decays into an electron and an undetected neutrino, while the low mass shoulder is due to Z events in which the recoiling hadronic energy is mismeasured. The 191 events that have an additional electron are mostly due to Z boson production, as is evident from the peak at 90 GeV of the M_{ee} distribution.

The 101 events with $E_T > 100$ GeV were scanned in search for anomalies. One event (run 88391, event 12124), was found to be caused by a cosmic ray muon that produced an EM shower due to a hard bremsstrahlung. In that event, there are clear muon hits in the three muon detector layers pointing to the EM shower and energy depositions in the hadronic layers consistent with a single minimum ionizing particle traversing the calorimeter. In addition the track found does not point to the primary vertex. The event was therefore removed from the sample.

There is no doubt (based on the visual inspection of the event display by many physicists familiar with muon and electron identification in DØ) that the event discarded is the result of a cosmic ray muon that interacted in the calorimeter. This can be interpreted as a 100% efficiency of this cut for real electrons. Ongoing efforts exist to try to implement such cosmic-ray rejecting cuts in an algorithmic way, for which the efficiency and rejection can be directly measured.

5.3.2 Signal Monte Carlo

The Monte Carlo used to simulate the W_R signal was described in Sec. 5.1. In the present case, however, the definition of a **matched** electron was restricted to match the first electron in $W_R^\pm \to e_1 N$. This choice was made to make this analysis insensitive to the assumptions about the massive neutrino decay. With this matching criterium, if the right-handed neutrino does decay into ejj (as was assumed in the search for two electrons and two jets) the acceptance for the W_R signal might be underestimated, which will lead to conservative limits. This will happen for events in which the electron from the N decay is central and has $E_T > 55$ GeV, while the electron from $W_R \to eN$ does not meet these
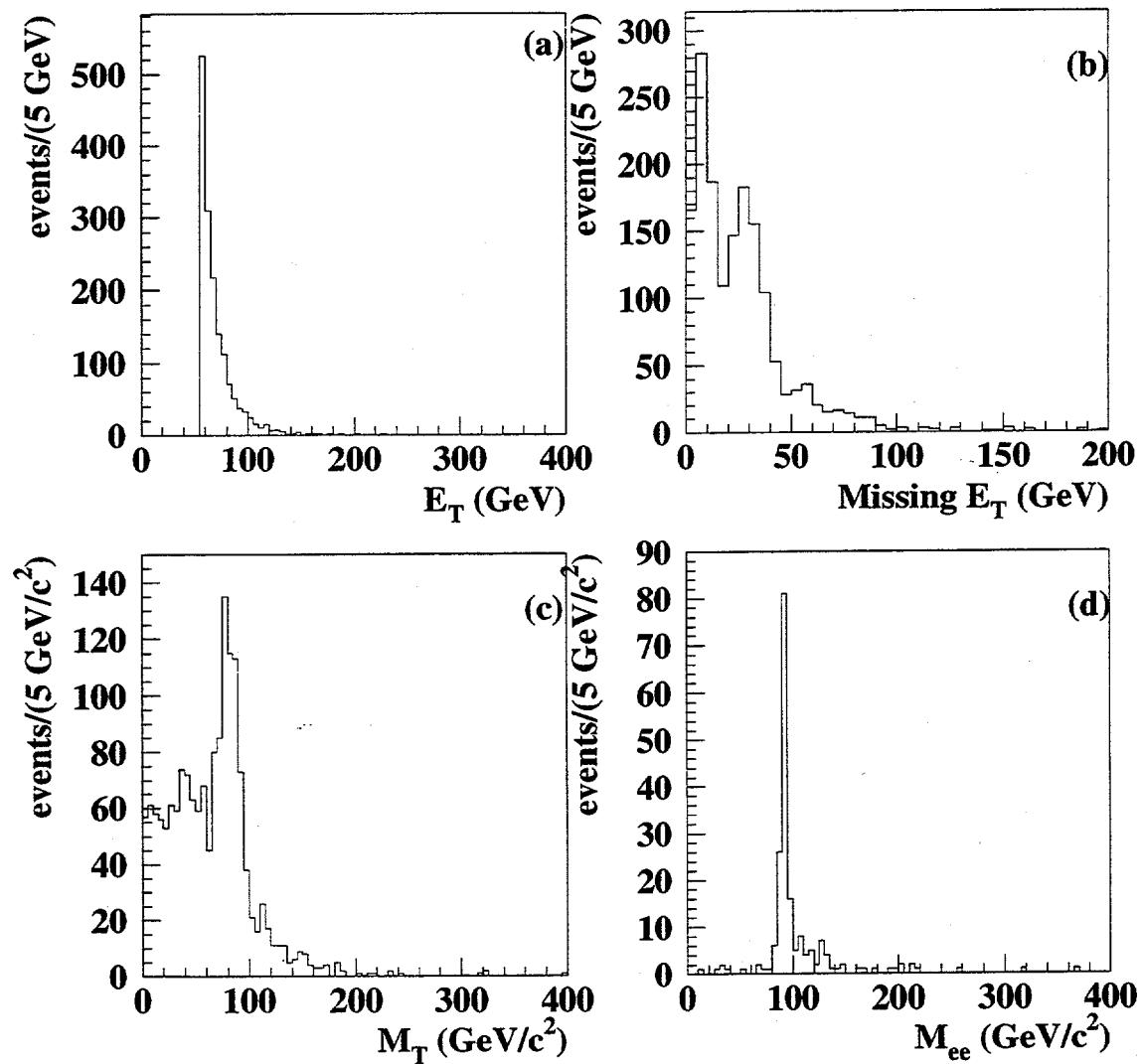
Figure 5.18: Distributions of the 1597 events passing all the requirements for the Jacobian peak search: (a) transverse energy of the golden electron, (b) missing transverse energy, (c) transverse mass of the electron-$\not{E}_T$ system and (d) The invariant mass of the two electrons for the 191 events that had an additional electron.

criteria.

Figure 5.19 shows the E_T and M_T distributions of the matched electron and $\not{E}_T$ for two different MC samples. The E_T distributions have the expected Jacobian peak but the transverse mass distributions show no structure, because there are no undetected neutrinos in the final state. The inclusion of non-matched electrons (from the model dependent N-decay) would have increased the normalization of the histograms, but their shapes would have remained almost identical to the ones shown.

The **dummy** Monte Carlo (see Sec. 5.1) was used also in this part of the search to fill up the parameter space (M_{W_R} and M_{N_R}) with a dense grid of points. There is, however, one important difference between the **dummy** and the fully simulated Monte Carlo. In the **dummy** MC, the efficiency for reconstructing and electron is uniform in ϕ (the azimuthal angle). On the other hand, the fully simulated MC has reconstruction inefficiencies at the azimuthal boundaries of the central calorimeter modules (32). These inefficiencies, which are a realistic representation of the detector's response, account for an additional 8% loss for electrons in the central region.

5.3.3   Background Simulation

The main source of events with a large E_T electron is W and Z production. To simulate these backgrounds, a toy Monte Carlo was used. This toy simulation [47] uses the W and Z line shape, as extracted from PYTHIA, to generate events. The transverse momentum of the gauge boson is generated according to a theoretical calculation [48] that includes both a non-perturbative part (for low p_T) and a perturbative part (for high p_T). A toy detector simulator was then used to emulate the effects of the EM and hadronic energy resolution, primary vertex position, multiple vertices, and the fiducial and kinematic cuts. In this way, 5,000,000 $W \rightarrow e\nu$ (including the $W \rightarrow \tau\nu \rightarrow e\nu\nu\nu$ contribution) and 1,000,000 $Z \rightarrow ee$ events were generated. Figure 5.20 shows distributions from these MC samples. The main features of these distributions are explained in what follows.

The spectra of electron transverse energy for W and Z bosons have nearly an exponential shape (plots (a) and (b) in the figure). These are the tails of the corresponding Jacobian peaks. These peaks, however, are not visible in the plots because of the $E_T > 55$ GeV cut
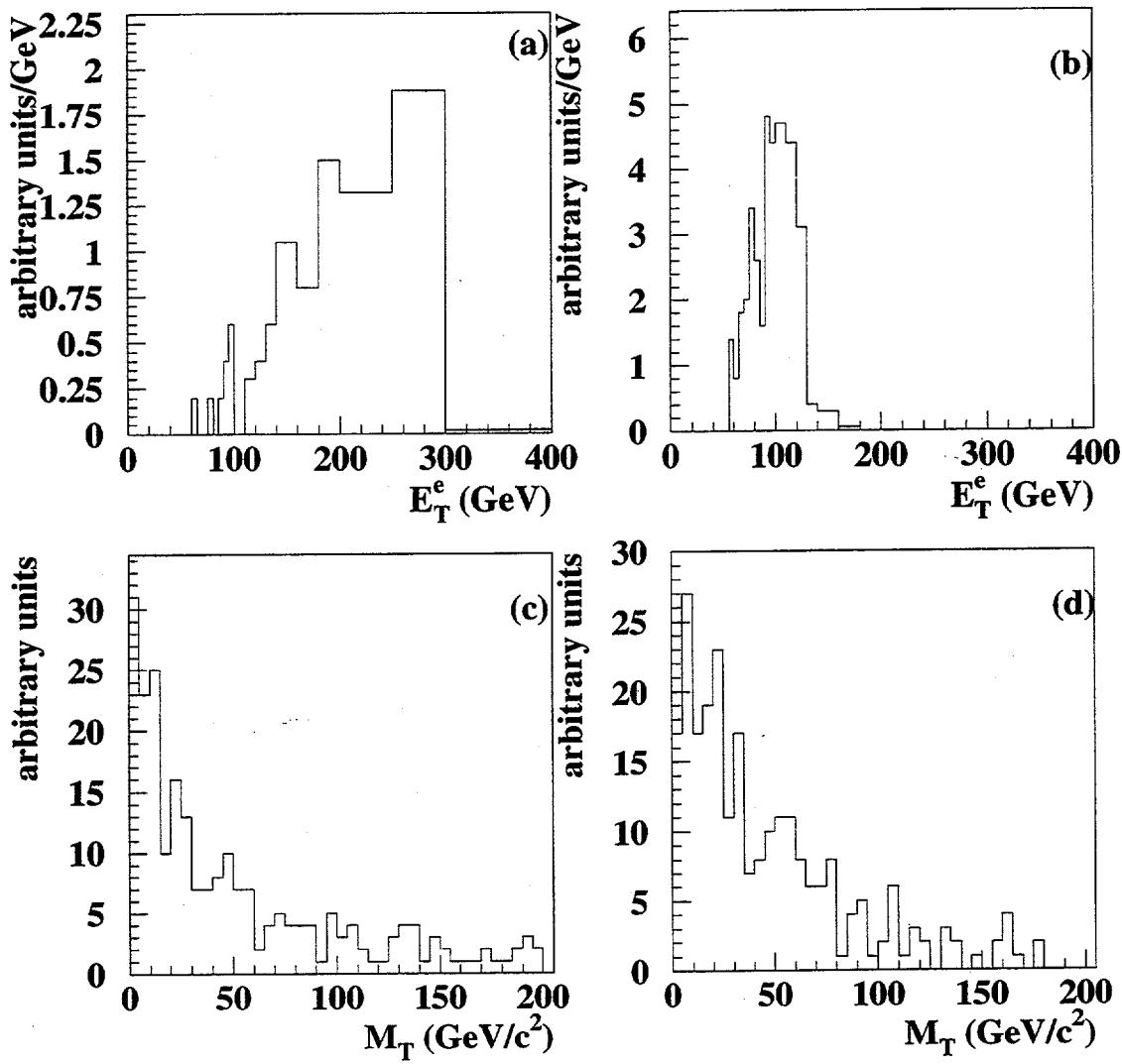
Figure 5.19: (a) Transverse energy of the matched electron and (c) transverse mass of the electron-$\not{E}_T$ system for a MC sample with $M_{W_R} = 600$ GeV and $M_{N_R} = 100$ GeV. In (b) and (d) the same distributions are shown for a sample with $M_{W_R} = 400$ GeV and $M_{N_R} = 100$ GeV.

(they are at ~ 40 GeV and ~ 45 GeV for W and Z respectively). On the other hand, the missing transverse energy distributions (plots (c) and (d)) are radically different. The large peak in the $\not{E}_T$ distribution for W bosons is due to the undetected neutrino. The smaller peak is caused by the kinematic cut on the electron. Events with $\not{E}_T > 55$ GeV are most likely to come from highly offshell (large mass) W bosons, while those with $\not{E}_T < 55$ GeV are due mostly to on-shell large transverse momentum W bosons. The small $\not{E}_T$ in Z events is due primarily to the underestimation of the hadronic energy recoiling against the Z boson. The transverse mass distribution for W's (plot (e)) shows the expected peak at the W mass ~ 80 GeV. The second peak at ~ 110 GeV is due to the $E_T > 55$ GeV cut, as explained above. Finally, the structure in the transverse mass for Z's is due to the correlation between the underestimated hadronic energy recoil and the transverse momentum of the Z boson.

The W and Z samples were then combined into a single sample, using the D∅ measured value [49] of the ratio:

$$R = \frac{\sigma_W \cdot B(W \to e\nu)}{\sigma_Z \cdot B(Z \to ee)} = 10.90 \pm 0.49. \tag{5.13}$$

The resulting distributions are shown in Fig. 5.21.

For the W background, two different types of events contribute to the sample. The first is due to predominantly low p_T W bosons from the high mass tail of the Breit-Wigner resonance. The second is due to large p_T W production mostly from the mass peak. In order to verify the accuracy of the toy MC, the p_T spectrum of the W candidates was compared to the simulated one. For this purpose, the subset of events with $\not{E}_T > 25$ GeV with no additional electron was selected. Figure 5.22 shows the comparison of the W enriched data sample with the MC, with the same kinematic cuts. The two distributions are consistent.

The top quark background (mostly from e+jets decays) was calculated to be less than 1% of the combined W and Z (assuming a 180 GeV top with 8 pb production cross section). In addition, the shapes of the electron E_T and M_T distributions are almost identical to the W background ones. For this reason, the top background was not explicitly included.

Finally, the fake electron background was considered. This type of background is due to QCD multijet events, in which one of the jets is misidentified as an electron (see Sec. 5.2.3). In order to model this background, the same single electron parent sample was used. This time, however, anti-cuts were imposed on the quality of the electron to ensure a negligible
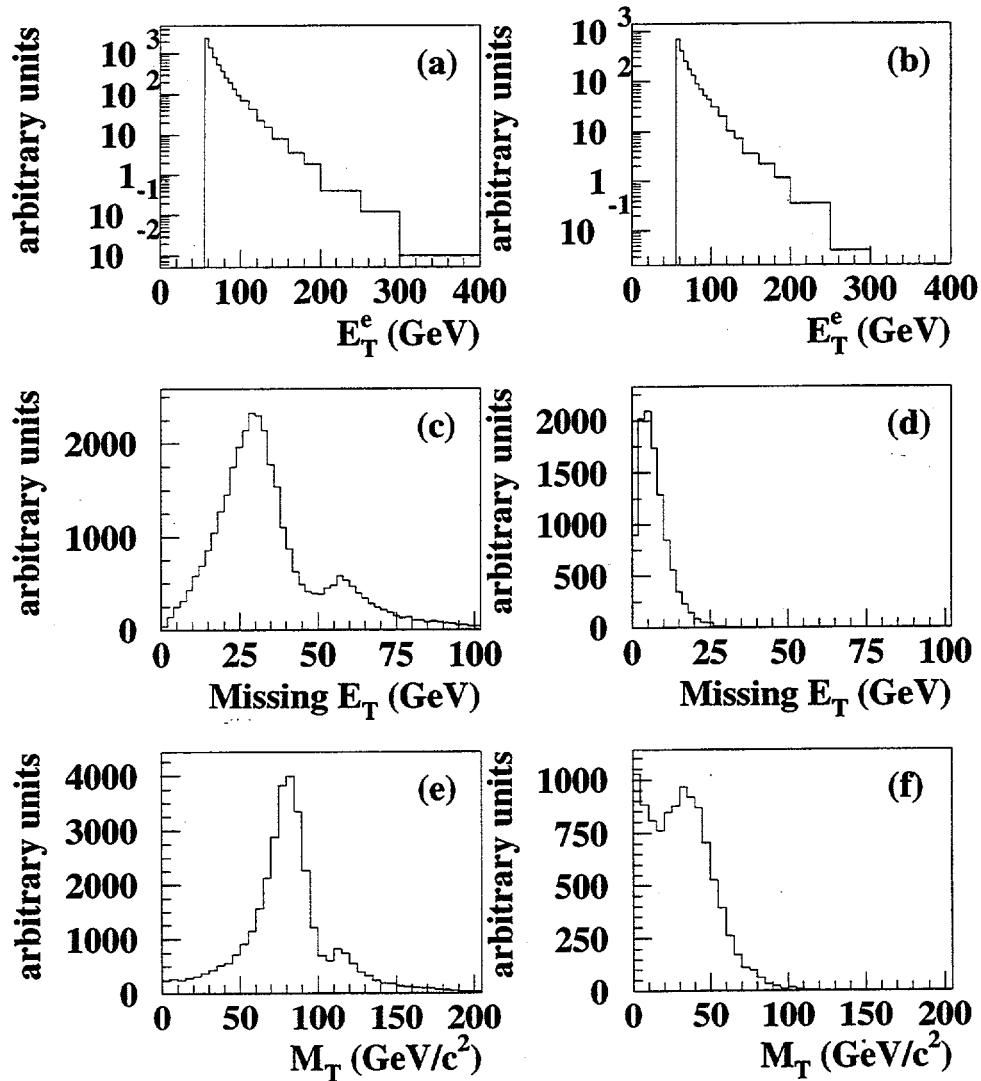
Figure 5.20: Transverse energy of the highest E_T central electron for (a) W toy MC and (b) Z toy MC. (c) and (d) show the missing transverse energy in the two samples, respectively. (e) and (f) show the transverse mass.
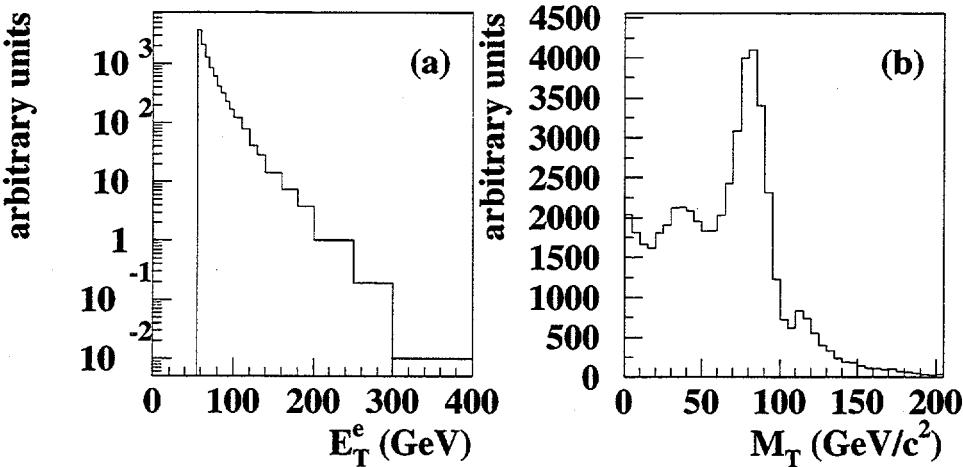
Figure 5.21: (a) Transverse energy of the highest E_T central electron for the combined W and Z toy MC sample. (b) The transverse mass of the same combined sample.

true-electron contribution. Two non-overlapping QCD background samples were generated with the requirements listed in table 5.10 in order to demostrate that the shapes of the distributions are nearly independent of the specific choice of anti-cuts. Figure 5.23 shows kinematic distributions from these samples. The $\not{E}_T$ and M_T show no peak, because most of the W events were removed by the anti-quality cuts. The advantage of creating fake background samples from the same parent sample (having some electron-like properties) is that the topology and the characteristics of these events will be close to the fake electron events that will pass all of the electron identification criteria. As can be seen in Fig. 5.23 the two orthogonally defined QCD background samples have nearly identical distributions (shape). Only the first sample is used to model the QCD background.

5.3.4 Fitting Procedure

In the absence of a W_R signal, the events that passed all the selection criteria (see Sec. 5.3.1) are ascribed to the background processes. The first step was therefore to verify this hypothesis with a simultaneous fit of the E_T and M_T distributions. In the fit, the weights
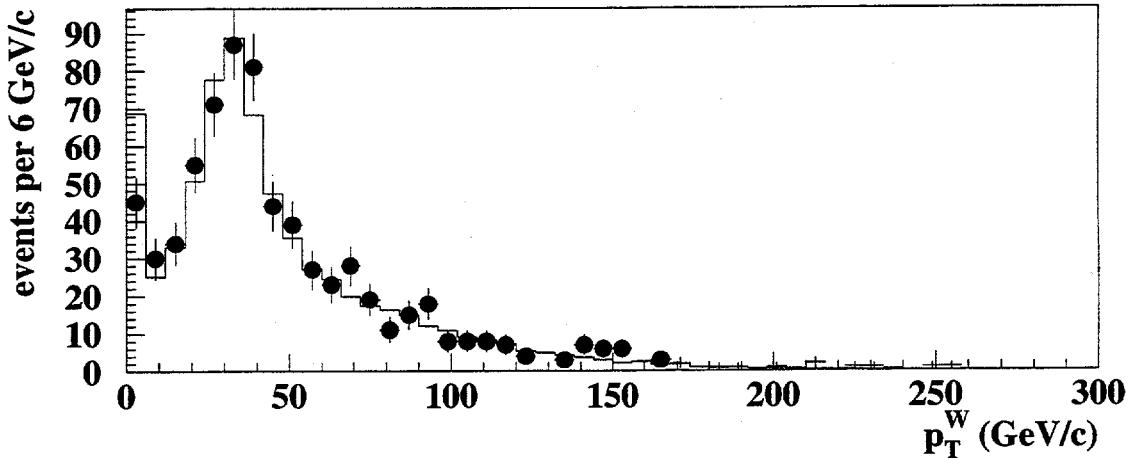
Figure 5.22: Transverse momentum of the 699 W boson candidates (points) in the sample. These were selected by requiring that there be no other electron candidate in the event and that $\not{E}_T > 25$ GeV. The same distribution is shown for a toy W MC sample (histogram). The MC has been normalized to the same number of events.

	QCD sample I	QCD sample II
electron-like (AND) requirements	$\frac{dE}{dx} < 1.5$ TMS < 5.0	$\chi^2_H < 100$ EMF > 0.95 ISO < 0.1
electron-unlike (OR) requirements	$\chi^2_H > 100$ EMF < 0.95 ISO > 0.1	$\frac{dE}{dx} > 1.5$ TMS > 5.0

Table 5.10: The cuts used to define the two QCD background samples. There is no overlap between the two samples or between them and the electron enriched sample. The fiducial and kinematic cuts are identical to the ones applied to the signal sample.
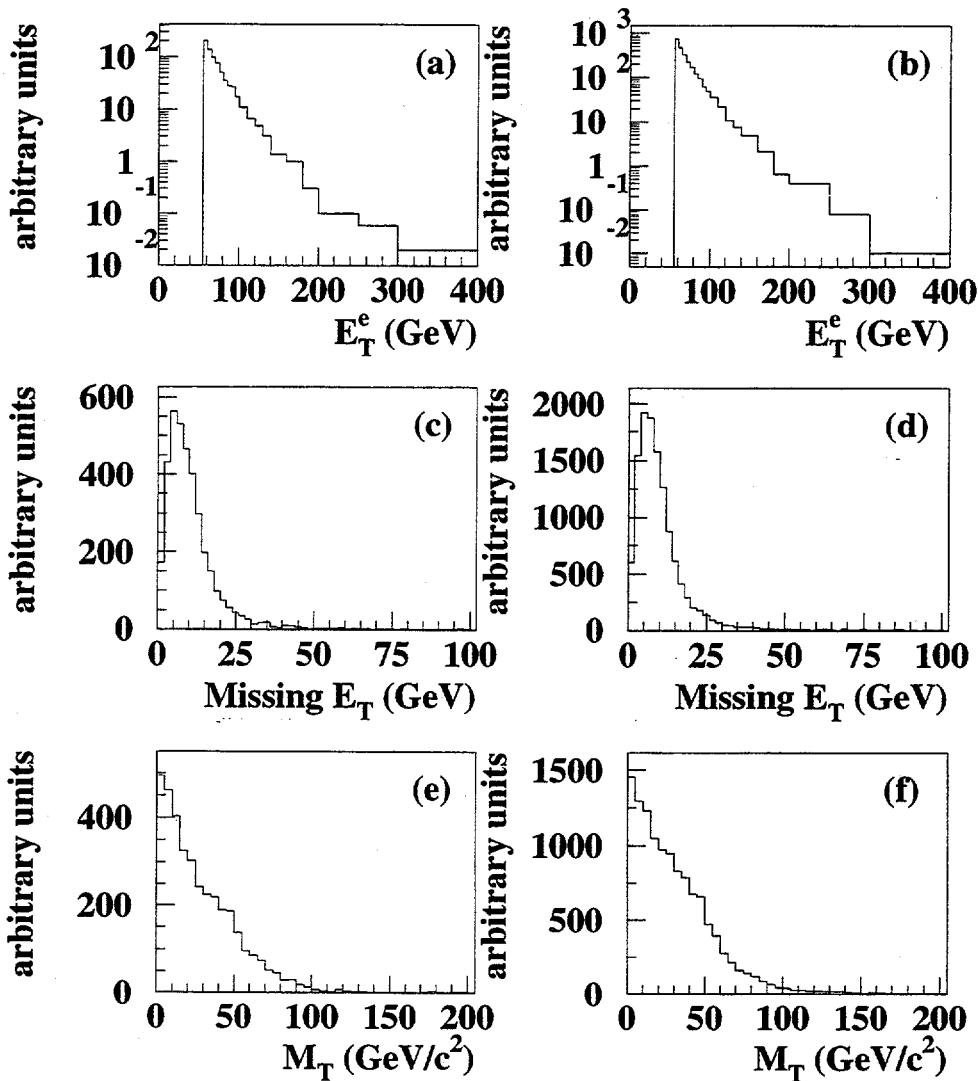
Figure 5.23: Transverse energy of the highest E_T central non-good electron for (a) QCD sample I and (b) QCD sample II. The $\not{\!\!E}_T$ in the two samples is shown in (c) and (d), respectively. (e) and (f) show the transverse mass.

of the W/Z background (combined W and Z toy MC) and the fake background (obtained from the data) are allowed to vary to reach the combination that best describes the data.

The fit was performed by maximizing the logarithm of the likelihood function:

$$\mathcal{L} = \prod_{i=1}^{B_{E_T}} P(\mu_{i,E_T}, n_{i,E_T}^{obs}) \prod_{j=1}^{B_{M_T}} P(\mu_{j,M_T}, n_{j,M_T}^{obs}), \qquad (5.14)$$

where

$$\mu_{i,E_T} = f^{WZ} \, n_{i,E_T}^{WZ} + f^{QCD} \, n_{i,E_T}^{QCD} \qquad (5.15)$$

and

$$\mu_{j,M_T} = f^{WZ} \, n_{j,M_T}^{WZ} + f^{QCD} \, n_{j,M_T}^{QCD}. \qquad (5.16)$$

P is the Poisson probability of observing the measured n_i^{obs} events in the i-th bin given a mean of μ_i; n_i^{WZ}, n_i^{QCD} and n_i^{WR} are the number of events in the i-th bin of the W/Z and QCD fakes histograms, respectively; and f^{WZ} and f^{QCD} are the fitted parameters and represent the weights of each of the two distributions. B_{ET} and B_{MT} are the numbers of bins being fitted in the E_T and M_T distributions, respectively. The MINUIT [50] program was used to find the maximum of the logarithm of $\mathcal{L}$.

Figure 5.24 shows the result of the simultaneous fit. In the figure, the points with errors represent the observed spectra while the solid histograms represent the best fit. The dashed histograms represent the part of the background due to QCD (approximately $3 \pm 2\%$). Both distributions are simultaneously well described by the sum of the W/Z and QCD backgrounds. The χ^2 per degree of freedom values are 1.01 and 0.82 for the E_T and M_T fits, respectively. With a more sophisticated analysis of the probability for the observed distribution, with full simulation of independent bin-by-bin Poisson fluctuations, a 71% C.L. was obtained for the E_T distribution and a 90% C.L. for the M_T fit. In Fig. 5.25 the ratio of the data to the fitted background is plotted as a function of the transverse energy of the electron. No evidence for statistically significant bumps is observed in this ratio.

5.3.5 Limits

The shape analysis, as described in the previous section, produced no clear evidence of the presence of a Jacobian peak in the single electron E_T spectrum. This implies the
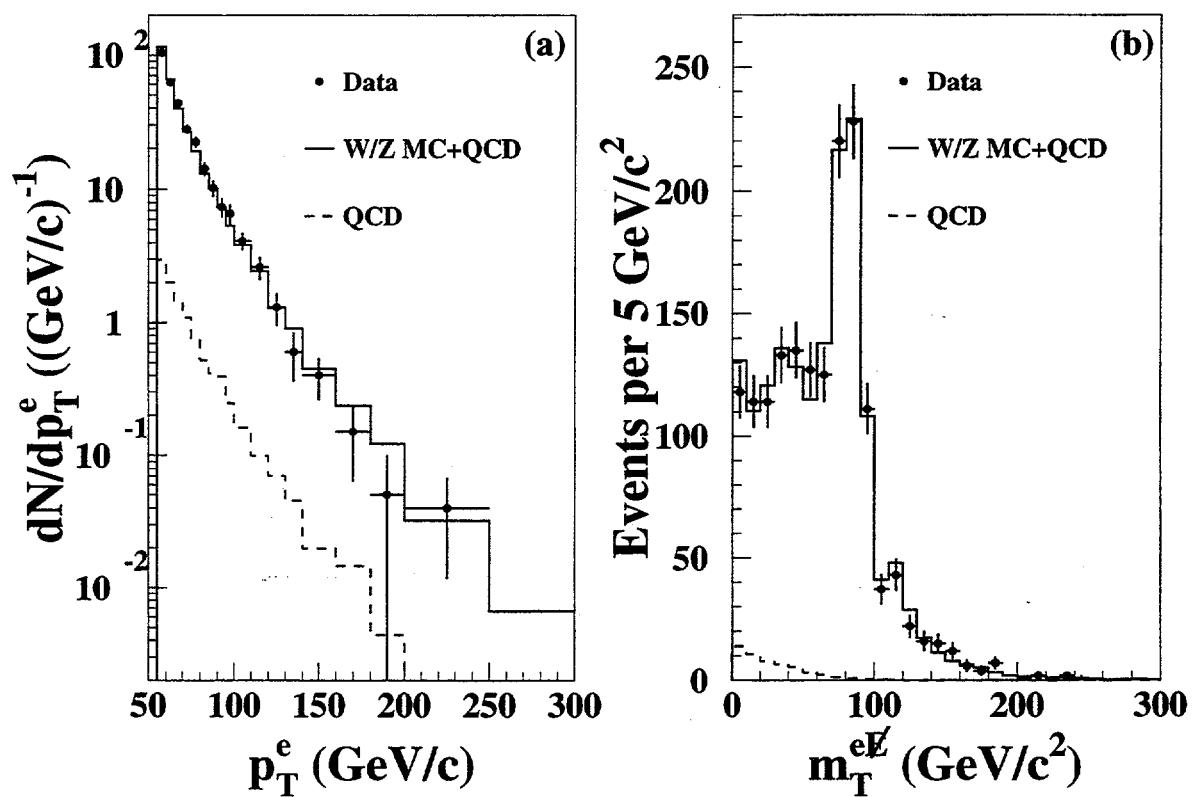
Figure 5.24: Result of the simultaneous fit of the E_T and M_T distributions. (a) E_T spectrum of the data (points with errors), the fitted sum of the backgrounds (solid histogram) and the QCD part of the background (dashed histogram). (b) Same as (a) but for the M_T spectrum.
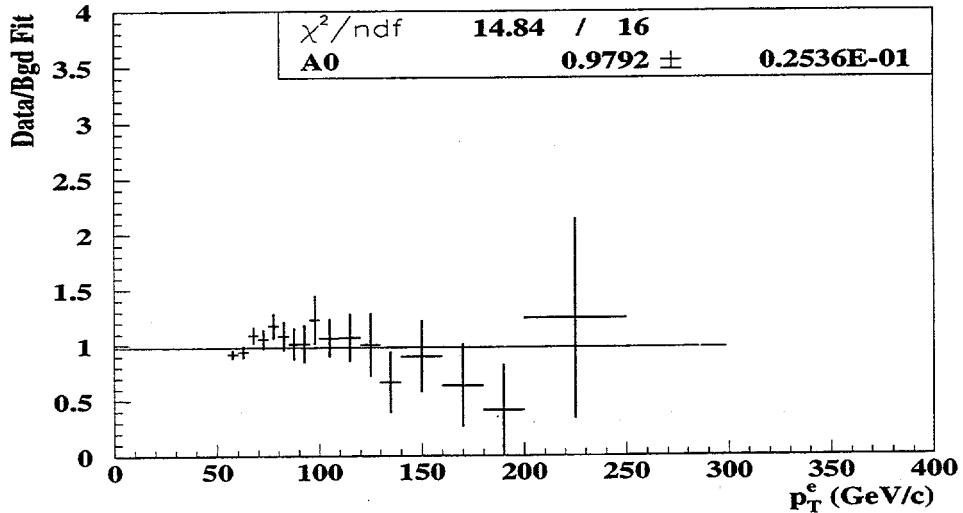
Figure 5.25: The ratio of the data over the fitted background as a function of the transverse momentum of the electron. The solid line is a fit to a constant.

absence of a clear W_R signal in the data sample and can be turned into an upper limit on its production cross section times branching ratio (σB). These cross section upper limits can, in turn, be converted into an excluded region in the M_{W_R}-M_{N_R} plane after assuming a theoretical W_R production cross section and branching ratio into the eN channel.

In order to obtain limits, the E_T distribution only was fitted allowing for an additional W_R component. In these fits (performed for a grid of input M_{W_R} and M_{N_R} masses), the W/Z component was fixed to the value determined from the simultaneous fit (see previous section) and the QCD background and the W_R components were allowed to vary. Varying the QCD background produces slightly less stringent limits (a conservative choice) than those obtained by fixing the QCD background to the fitted values from the simultaneous fit because it leaves more room for a potential W_R component (note that the shapes of the E_T distributions for W/Z and QCD are almost identical). However, the difference is not significant due to the smallness and the large error of the fitted QCD background ($3 \pm 2\%$).

The 95% CL upper limit on the W_R signal weight for a given fit (corresponding to a mass point) was obtained by integrating the likelihood function and solving:

$$\int_0^{f_{95}^{W_R}} \mathcal{L}(f^{WZ}, f^{QCD}, f^{W_R}) \, df^{W_R} = 0.95 \int_0^\infty \mathcal{L}(f^{WZ}, f^{QCD}, f^{W_R}) \, df^{W_R}, \qquad (5.17)$$

where f^{WZ} and f^{QCD} are known from the previous fits. $f_{95}^{W_R}$ is the upper limit for the signal weight. The uncertainty on the W/Z component (from the initial simultaneous fit) was included in the limit by integrating (not shown in equation 5.17) over a Gaussian with mean f^{WZ} and $\sigma = \sigma_{f^{WZ}}$. $f_{95}^{W_R}$, the 95% CL limit on the W_R component, is typically two to three times the value of the uncertainty on f^{W_R}, as expected.

The 95% CL on the cross section times branching ratio is then obtained using the normalization provided by the W/Z component (for which the production cross section is known) with:

$$N_{95}^{W_R} = f_{95}^{W_R} \, N_{gen}^{W_R} \, A^{W_R} = \mathcal{L}_{int} \, (\sigma B)_{95}^{W_R} \, A^{W_R} \, \epsilon_e, \qquad (5.18)$$

where $N_{95}^{W_R}$ is the upper limit on the number of W_R events. $N_{gen}^{W_R}$ is the number of generated W_R events (400 for most points). A^{W_R} is the kinematic and fiducial acceptance of the cuts applied and $\mathcal{L}_{int}$ is the integrated luminosity of the sample. Finally, ϵ_e is the efficiency for reconstructing an electron (with the given electron quality cuts) that is within the acceptance and $(\sigma B)_{95}^{W_R}$ is the cross section upper limit.

An analogous expression can be written for the W/Z background:

$$N^{WZ} = f^{WZ} \, N_{gen}^{WZ} \, A^{WZ} = \mathcal{L}_{int} \, (\sigma B)^{WZ} \, A^{WZ} \, \epsilon_e. \qquad (5.19)$$

Notice that ϵ_e is assumed to be the same as in equation 5.18, namely, the efficiency for the detection of an electron from W/Z decays is the same as for W_R decays. The 95% CL upper limit can then be written as:

$$(\sigma B)_{95}^{W_R} = \frac{N_{gen}^{W_R}}{N_{gen}^{WZ}} \frac{f_{95}^{W_R}}{f^{WZ}} (\sigma B)^{WZ}. \qquad (5.20)$$

In order to calculate the last ratio, the DØ measured value [49] of the W production cross section times branching fraction of $2.36 \pm 0.07 \pm 0.13$ nb was used as well as the number of generated toy MC events.

The W/Z toy Monte Carlo does not simulate the loss of efficiency near the edges of the central calorimeter modules. The same is true for the W_R **dummy** MC (see Sec. 5.3.2).

On the other hand, the fully simulated W_R MC does include this effect. For this reason, the effective value of the efficiency for the fully simulated events has to be increased by 8%, while no factor has to be added to the **dummy** MC events.

Figure 5.26 shows the 95% CL upper limit on the cross section times branching ratio as a function of the energy of the first electron in the CM frame E_e^{CM}. The circles and the squares show the limits obtained for the fully simulated and **dummy** MC mass points, respectively. Some basic features of this graph can be readily explained with simple arguments. First, the limits improve rapidly with increasing E_e^{CM}. This is due to the almost exponential form of the background. Second, at large E_e^{CM} the limit flattens out. This is due to the limited statistics (e.g. with no observed events, the 95% CL upper limit on the number of signal events is 3 regardless of the expected background).

In order to produce smooth mass contours without disconnected regions from cross section times branching ratio limits obtained at discrete values of the W_R and N masses, a parametrization was used. This parametrization, which is plotted also (solid line) in Fig. 5.26, is an empirical function designed to be a conservative limit (i.e. leaving most of the points below it):

$$(\sigma B)_{95}^{W_R} = e^{e^{2.7052 - 0.01350 E_e^{CM}} - 2} \tag{5.21}$$

where $(\sigma B)_{95}^{W_R}$ is the upper limit on the cross section times branching ratio in picobarn units.

Figure 5.27 shows the 95% CL upper limits on σB as a function of the W_R mass. The corresponding exclusion contours are shown in Fig. 5.28 for various values of the LRM parameters. The systematic uncertainty on the W/Z background normalization was included in the limit. It has contribution from the uncertainty on the measured W cross section (dominated by the 5.5% uncertainty in the integrated luminosity). As expected, this method is most powerful for the low values of the right-handed neutrino mass.

Because the limits in this part of the search were extracted from the lack of an excess or peak in the E_T distribution of the electron, without any other requirements on the event, they are valid irrespective of the assumptions about the massive neutrino such as its decays, interactions and lifetime. For instance, if the massive neutrino does not decay inside the detector and escapes detection (like the standard light neutrino), the M_T distribution will
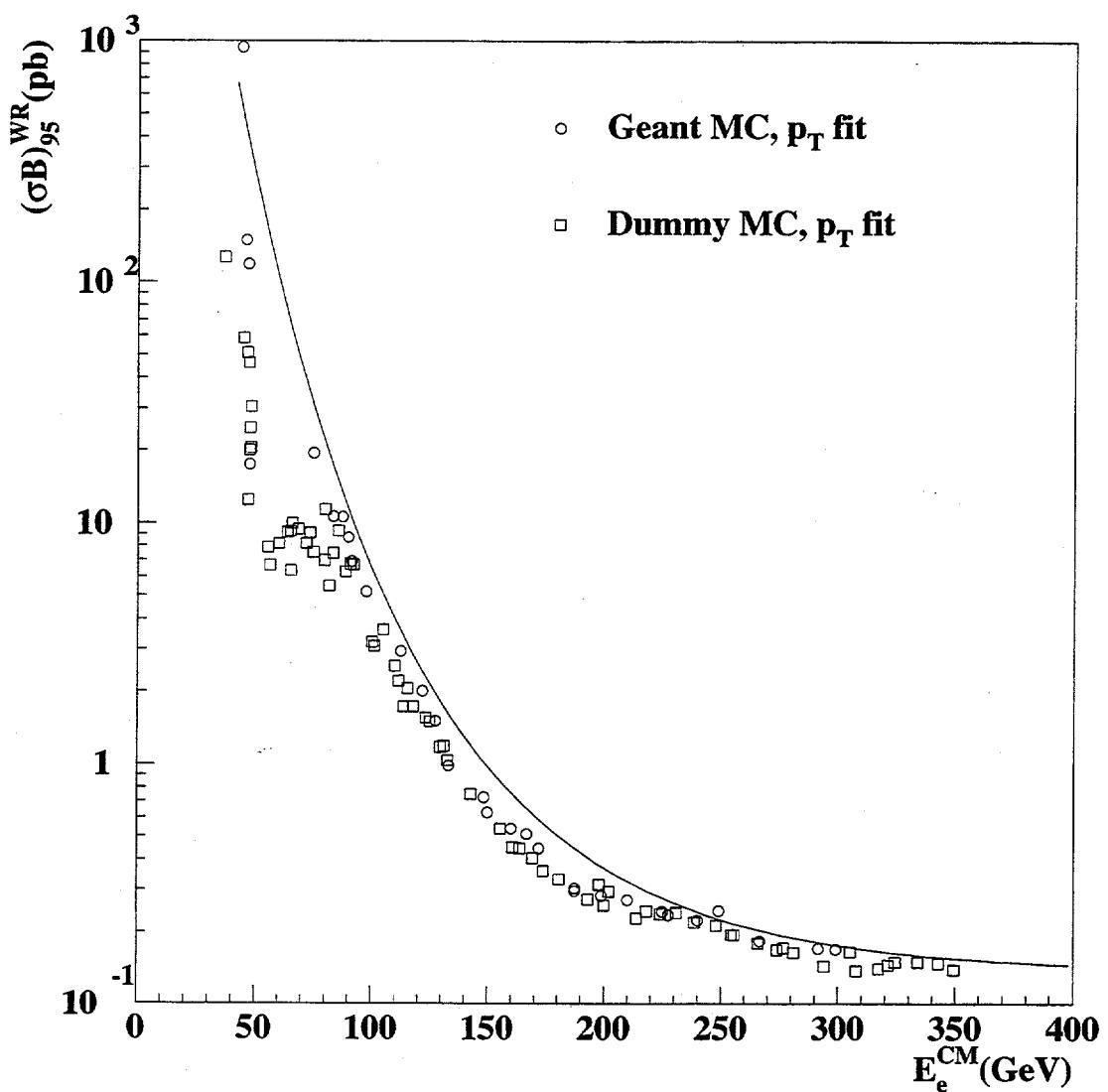
Figure 5.26: 95% confidence upper limits on the cross section times branching ratio for $W_R \rightarrow eN$ versus the energy of the first electron in the CM frame. The circles and the quares are the limits obtained for the fully simulated and **dummy** MC mass points, respectively. The function is the conservative limit used to set the mass limits.
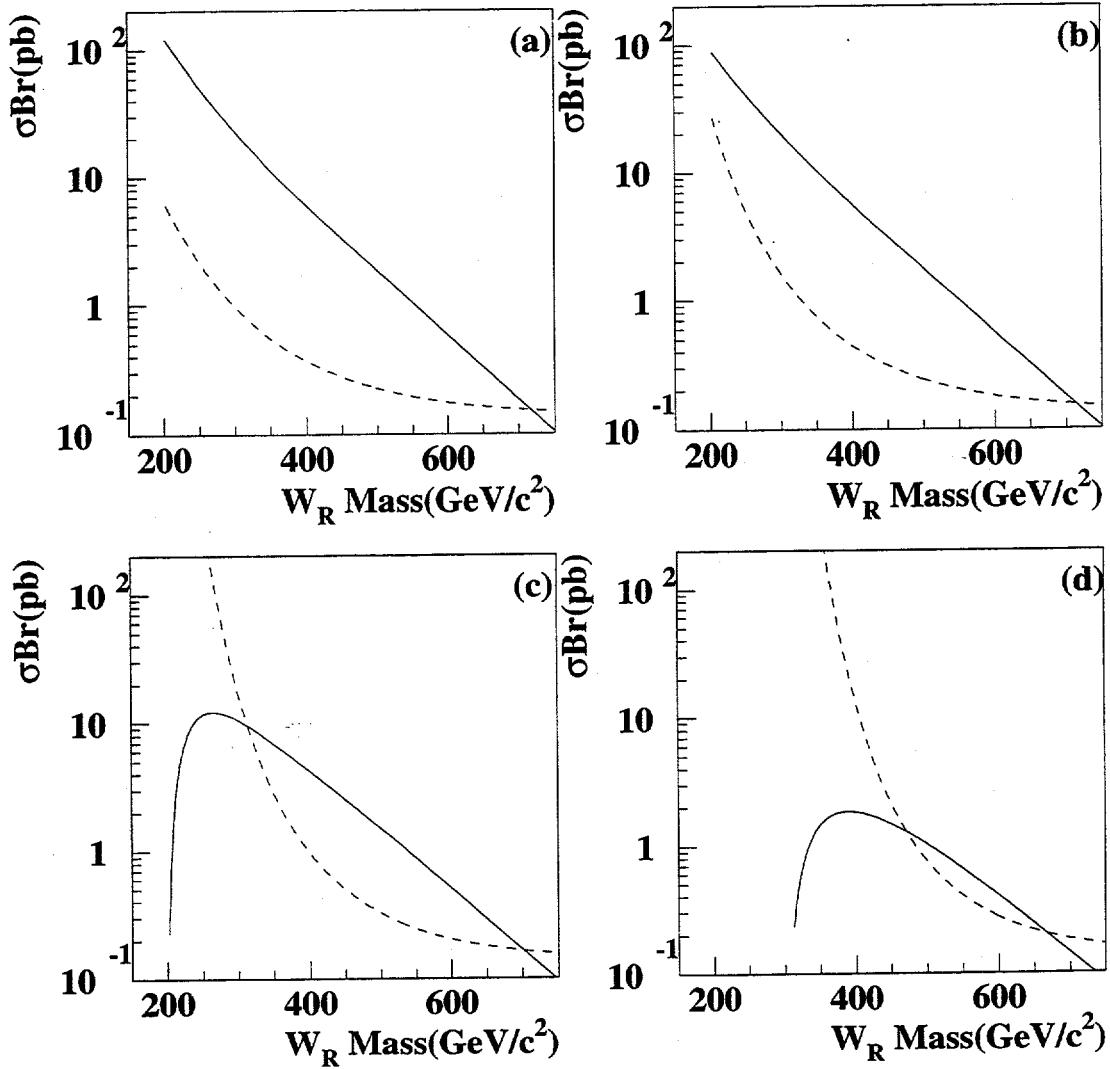
Figure 5.27: The 95% CL limit on the cross section times branching fraction of $W_R \to eN$ irrespective of the N decay. The limits (dashed) and theoretical σB (solid) are shown for (a) $M_{N_R} = 0$, (b) $M_{N_R} = 100$, (c) $M_{N_R} = 200$ and (d) $M_{N_R} = 300$ GeV. The cross section was obtained using the MRS(H) PDF set, assuming that $g_L = g_R$ and $V_{qq'}^L = V_{qq'}^R$.
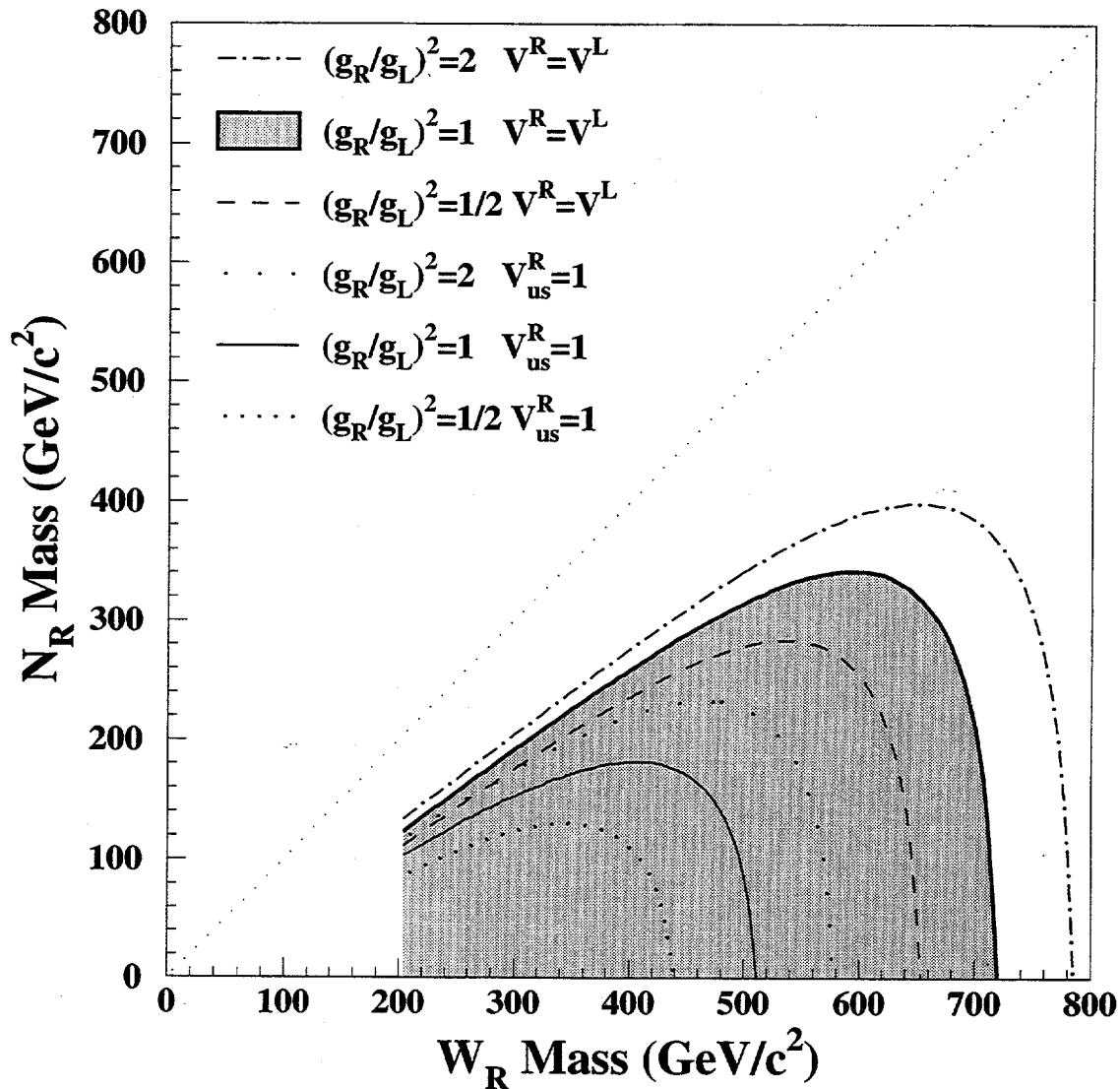
Figure 5.28: Excluded region of masses at the 95% C.L. from the E_T peak search. The region inside the lines are excluded for (shaded) $V_{qq'}^L = V_{qq'}^R$ and (solid) $V_{us}^R = 1$, assuming $(g_R/g_L)^2 = 1$. For each CKM matrix case, the excluded regions corresponding to $(g_R/g_L)^2 = 0.5$ and $(g_R/g_L)^2 = 2$ are also shown. The $M_{W_R} = M_{N_R}$ line represents the kinematical limit for the $W_R \rightarrow eN$ decay.

be sharply peaked at the value of M_{W_R}. This is radically different from the M_T obtained from the assumed massive neutrino decays (see Fig. 5.19). The E_T distribution, on the other hand, is identical in both cases.

5.4 Results

The two methods described in Sec. 5.2 and 5.3 yielded no statistically significant excesses that could be ascribed to the presence of W_R bosons in the data.

From the search for two electrons and two jets, 95% C.L. excluded regions were obtained for the two extreme mixing cases. These are shown in Fig. 5.15 and Fig. 5.16, respectively. For other values of the mixing angle, an area of intermediate size (between the two extreme cases) is excluded, as shown in Fig. 5.29.

The 95% C.L. excluded regions from the search for additional peaks in the electron transverse energy distribution are shown in Fig. 5.28. These mass limits are independent of the N_R decay.

Figure 6.1 summarizes the null results of the two methods used for the search as an exclusion region in the (M_{W_R}, M_{N_R}) plane at the 95% confidence level. A substantial region is excluded by both methods. There is a large correlation between the two limits in the region where their contours intersect. For this reason, no significant improvement can be obtained by combining the two limits.

The methods used for this search do not distinguish between the helicity states of the gauge bosons or of the final state particles. Therefore, the limits obtained are valid also for gauge bosons with left-handed couplings. In particular, they represent a new limit on the mass of a heavy left-handed gauge boson (W'_L) decaying into an electron and a neutrino $W'_L \to e\nu$.
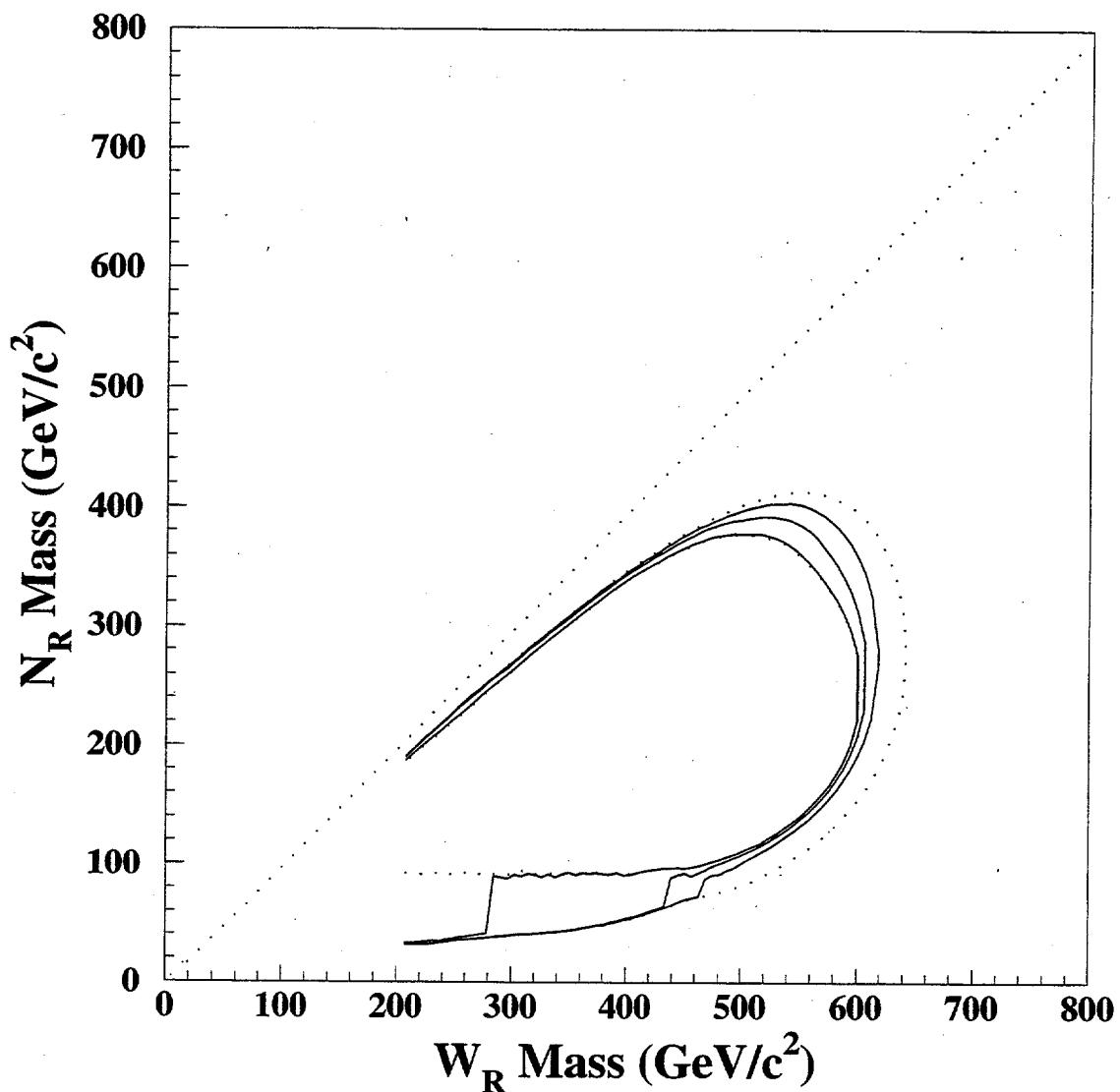
Figure 5.29: 95% C.L. excluded W_R mass regions from the search for two electrons and two jets as a function of the mixing angle ξ. From the inside out the limits are shown for $\xi = 1$ (large mixing case), 0.05 (approximately the present upper limit on ξ), 0.01, 0.005 and 0 (no mixing case).

Chapter 6

Conclusions

In conclusion, a search for right-handed W bosons with mass greater than 200 GeV/c^2 decaying into an electron and a massive right-handed neutrino $W_R \rightarrow eN_R$ was performed using data corresponding to an integrated luminosity of 79 pb^{-1} collected with the DØ detector at Fermilab. Two methods, optimized for different values of the N_R mass, were used for the search. In the first, an excess of events with two electrons and two jets, from the subsequent decay (through a charged current) of the right-handed neutrino to an electron and two jets, was sought for. In the second, a search for an additional peak in the transverse energy spectrum of the inclusive electron data was performed.

No statistically significant excess was found with either method. From the search for additional peaks, mass limits independent of the N_R decay were set: $M_{W_R} > 650$ GeV/c^2 and $M_{W_R} > 720$ GeV/c^2 at the 95% confidence level (C.L.), valid for $M_{N_R} < \frac{1}{2}M_{W_R}$ and $M_{N_R} \ll M_{W_R}$ respectively (assuming Standard Model couplings). From the search for an excess of events with two electrons and two jets, model dependent limits were set: $M_{W_R} > 550$ GeV/c^2, valid for $\frac{1}{5}M_{W_R} < M_{N_R} < \frac{3}{4}M_{W_R}$ if the mixing between W_R and W_L is negligible (and assuming Standard Model couplings).

Figure 6.1 summarizes the null results of the two methods used for the search as an exclusion region in the (M_{W_R}, M_{N_R}) plane at the 95% confidence level. A substantial region is excluded by both methods. There is a large correlation between the two limits in the region where their contours intersect. For this reason, no significant improvement in

the limit can be obtained by combining them. The exclusion region from the peak search is valid irrespective of the specific decay of the right-handed neutrino, making this the first analysis of its type.

The methods used for this search do not distinguish between the helicity states of the gauge bosons or of the final state particles. Therefore, the limits obtained are valid also for gauge bosons with left-handed couplings. In particular, they represent a new limit on the mass of a heavy left-handed gauge boson (W'_L) decaying into an electron and a neutrino $W'_L \to e\nu$: $M_{W'_L} > 720$ GeV/c^2 at the 95% C.L.

These new limits on the mass of right-handed W bosons represent stringent, though somewhat model dependent, limits on possible $V + A$ couplings. Therefore, they should be considered when planning future low energy experiments looking for deviations from the $V - A$ predictions. For instance, new muon decay experiments will have to reach a sensitivity of 0.00035 on the measurement of $1 - \xi P_\mu \frac{\delta}{\rho}$ to be able to further improve these limits. This corresponds to a factor of two improvement in the systematic error of the best existing measurement [21] of the parameter $1 - \xi P_\mu \frac{\delta}{\rho}$, assuming negligible statistical errors in a hypothetical new experiment.

Future and ongoing efforts to search for W_R bosons at colliders should concentrate on both hadronic and leptonic final states. In the leptonic case (if $M_{N_R} < M_{W_R}$), searches can probe simultaneously the existence of W_R bosons and the Majorana type of right-handed neutrino using final states with two same-sign leptons and two jets. In the hadronic case, the generic searches for bumps in the dijet mass spectrum and searches for $W_R \to tb$ [18] can provide important model independent limits.
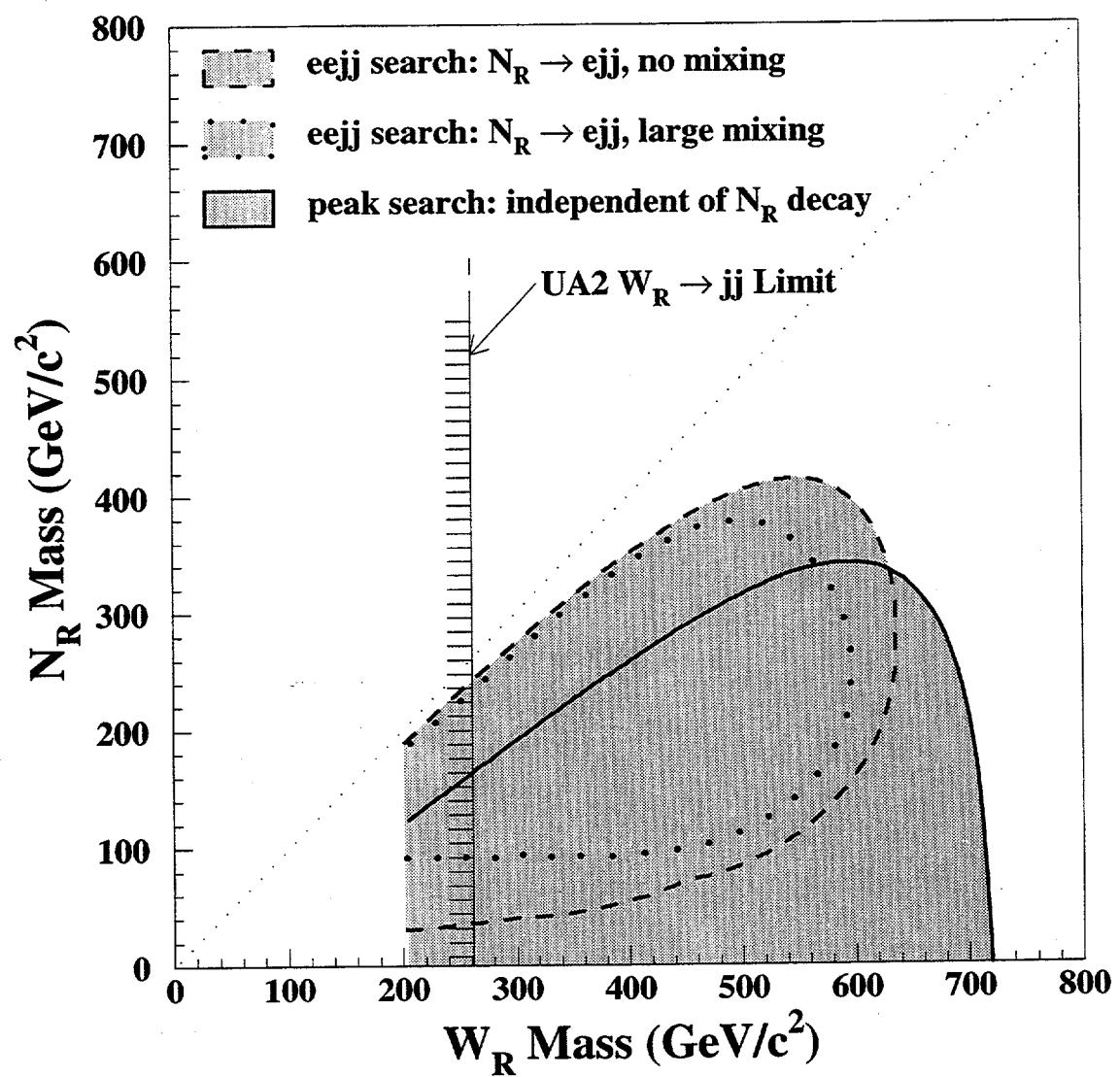
Figure 6.1: Excluded regions of W_R mass at 95% CL assuming $g_R = g_L$ and $V^R = V^L$ from the two search methods used.

Appendix A

EM Shower Position Measurement

The position measurement of electromagnetic showers plays an important role in electron and photon identification and measurement. For electrons, the EM shower centroid is used to determine the level of agreement between the shower position and the projection of the corresponding central track. This, in turn, is used to reject backgrounds from EM jets with overlapping charged tracks (from charged mesons in jets).

For photons and electrons, the shower centroid position is used to calculate the momentum vector, given the energy measurement from the calorimeter and the position of the primary vertex.

The energy depositions in cells of the finely segmented (in ϕ and η) third layer of the EM calorimeter (EM3) are used to calculate a weighted mean $\vec{x}_c$ of the cell coordinates $\vec{x}_i$ [34] ,

$$\vec{x}_c = \frac{\sum_i w_i \vec{x}_i}{\sum_i w_i}. \tag{A.1}$$

The weights w_i are defined as

$$w_i = \max\left(0, w_0 + \ln\left(\frac{E_i}{E}\right)\right), \tag{A.2}$$

where E_i is the energy of the ith cell, E is the total energy of the cluster, and w_0 is a position and energy dependent parameter, chosen to minimize the position resolution. Simpler weighting schemes, such as an arithmetic mean, yield worse position resolutions because they tend to give negligible weights to cells in the tails of the shower that contain

small amounts of energy due to the exponential lateral profile of EM showers.

To investigate possible biases in the position measurement determined using equation A.1, single electron Monte Carlo samples with plate-level simulation were used. The first plot (a) in Fig. A.1 shows the difference between the z position calculated with equation A.1 and the true position of the MC electron (determined with the projection of the MC track to the EM3 layer) as a function of the measured z position for 50 GeV electrons in the central calorimeter. Only one half (positive z values) of the calorimeter is shown due to the detector symmetry. A bias as large as 1 cm is measured for electrons near the edge of the CC.

In order to eliminate this position bias in the CC, two changes are introduced in the algorithm for central EM showers. These changes apply only to the z coordinate measurement, leaving the ϕ coordinate measurement as shown in equation A.1. The first is the use of a *collapsed cell* instead of single cells. A *collapsed cell* results from adding the energy in cells at a given z into a single quantity (collapsing the ϕ coordinate). The same weighted mean is then used to determine the z position using the *collapsed cell* energies and their corresponding z coordinates. In this case, a fixed w_0 (independent of energy and position) is used. The second plot (b) in Fig. A.1 shows the z position bias using the algorithm with *collapsed cells*.

The remaining bias is due to a dependence of the algorithm on the angle of incidence of the electron. This bias results from the different energy distributions in the EM3 layer from showers developing at different angles with respect to the flat (parallel to the z axis) uranium absorber plates. The first plot (a) in Fig. A.2 shows the difference between the z position calculated using the *collapsed cells* and the true position of the MC electron as a function of the angle of incidence θ for the 50 GeV MC sample. A clear dependence can be observed. This bias was parameterized using a seventh order anti-symmetric polynomial function (without the even power terms). In order to verify that the observed dependence is not due to some residual z dependence, the remaining plots in the figure (b, c and d) show the same plot for three different z-regions along with the same function.

The third plot (c) in Fig. A.1 shows the improvement achieved after an additional correction for the angle of incidence dependence is applied.

Angle of incidence dependences were also observed in the position measurement of EC
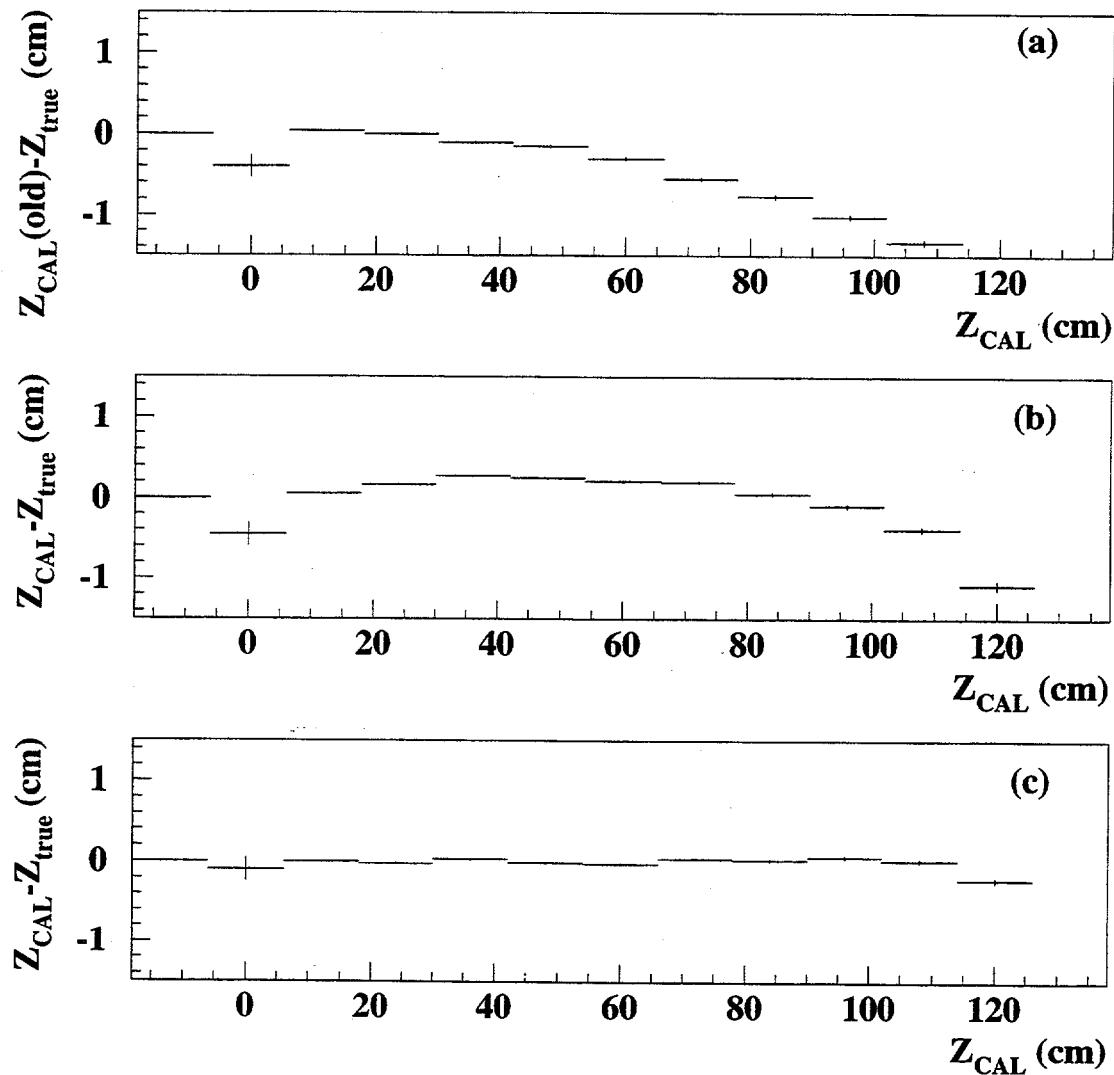
Figure A.1: Position measurement bias as a function of the z position. The position bias is shown (a) for the original (now obsolete) single cell weighting scheme, (b) for the algorithm using *collapsed cells*, and (c) for the algorithm using *collapsed cells* with an additional angle of incidence correction.
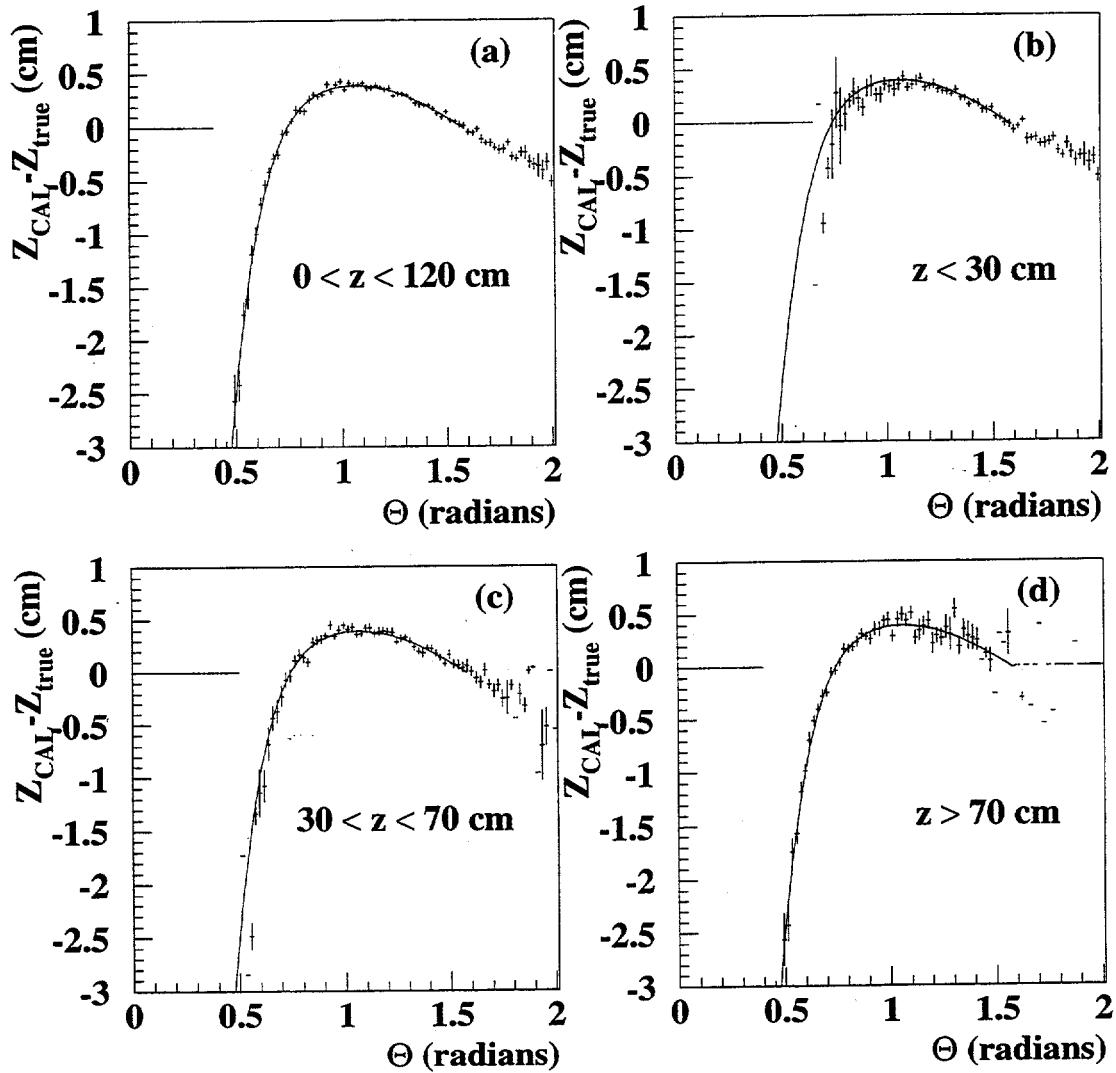
Figure A.2: Position measurement bias as a function of the angle of incidence. The position bias is shown (a) for the entire CC (points). The other plots (b,c,d) show the bias for three different z-coordinate ranges. The function (solid line) is a parametrization to correct for this bias.

electrons. These are also corrected using a parametrization. The EM position measurement algorithm with the described corrections have been implemented in the current standard DØ software code for measurement and identification of electrons and photons.

Bibliography

[1] R. N. Mohapatra: **Unification and Supersymmetry**, New York, Springer-Verlag, 1992

[2] J. C. Pati and A. Salam, Phys. Rev. **D10**, 275 (1974)

[3] S. L. Glashow, Nucl. Phys. **22**, 579 (1961); S. Weinberg, Phys. Rev. Lett. **19**, 1264 (1967); A. Salam, **Elementary Particle Theory**, ed. N. Svartholm (Almquist and Wiksells, Stockholm, 1968)

[4] M. Gell-Mann, P. Ramond and R. Slansky: **Supergravity**, edited by D. Freedman and P. Van Nieuwenhuizen, North-Hollnad, Amsterdam (1979)

[5] G. Senjanović, Nucl. Phys. **B153**, 334 (1979)

[6] R. N. Mohapatra and G. Senjanović, Phys. Rev. **D23**, 265 (1981)

[7] V. D. Barger,R. J. N. Phillips: **Collider Physics**, Redwood City, California, Addison-Wesley Publishing Company, 1988

[8] R. Hamberg, J. van Neervan, and T. Matsuura, Nucl. Phys.B359,343 (1991).

[9] E. Eichten, I. Hinchliffe, K. Lane and C. Quigg, Rev. Mod. Phys. **58**, 1065 (1995)

[10] A. D. Martin, R. G. Roberts and W. J. Stirling, Phys. Lett. **306B**, 147 (1993) and Erratum-ibid. **309B**, 492 (1993)

[11] A. D. Martin, R. G. Roberts and W. J. Stirling, RAL-93-077 (1993)

[12] C. Weinheimer *et al.*, Phys. Lett. **B300** 210 (1993); E. Holzschuh, M. Fritschi and W. Kuendig, Phys. Lett. **B287** 381 (1992); H. Kawakami *et al.*, Phys. Lett. **B256** 105 (1991); R.G.H. Robertson *et al.*, Phys. Rev. Lett. 67 957 (1991)

[13] Particle Data Group, *Review of Particle Properties*, Phys. Rev. **D50** (1994)

[14] W. Keung and G. Senjanović, Phys. Rev. Lett. **60**, 1427 (1983)

[15] M. Gronau, C. N. Leung and J. L. Rosner, Phys. Rev. D **29**, 2539 (1984)

[16] P. Langacker, R. W. Robinett and J. L. Rosner, Phys. Rev. D **30**, 1470 (1984)

[17] H. Tso-hsiu, C. Cheng-rui and T. Zhi-jian, Phys. Rev. D **42**, 2265 (1990)

[18] J. L. Rosner and E. Takasugi, Phys. Rev. D **42**, 241 (1990)

[19] P. Langacker and S. U. Sankar, Phys.Rev.D40 1569, (1989)

[20] R. Barbieri and R. N. Mohapatra, Phys. Rev. **D39**, 1229 (1989;)G. Raffelt and D. Seckel, Phys. Rev. Lett. **60**, 1793 (1988)

[21] J. Carr *et al.*, Phys. Rev. Lett. **51**, 627 (1983); A. E. Jodidio *et al.*, Phys. Rev. **D34**, 1967 (1986); A. E. Jodidio *et al.*, Phys. Rev. **D37**, 237(E) (1988)

[22] Lawrence K. Gibbons (Chicago U.) Ph.D. Thesis. Aug 1993; C. Geweniger *et al.*, Phys.Lett. **52B**, 108 (1974); S. Gjesdal *et al.*, Phys.Lett. **52B**,113 (1974)

[23] A. Chen *et al.*, Phys. Rev. Lett. **52**, 1084 (1984)

[24] H. Albrecht *et al.*, Phys. Lett. **B192** 245 (1987)

[25] C. Haxton and G. J. Stephenson, Prog Nucl. Part. Phys. **12** 409 (1984)

[26] CDF Collaboration, F. Abe *et al.*, Phys. Rev. Lett. **74**, 2900 (1995)

[27] DØ Collaboration, S. Abachi *et al.*, Phys. Lett. **B358**, 405 (1995)

[28] UA2 Collaboration, J. Alitti *et al.*, Nucl. Phys. **B400**, 3 (1993)

[29] CDF Collaboration, R. Harris, presented at the 10th Topical Workshop on Proton-Antiproton Collider Physics at FNAL, May 1995; FERMILAB-Conf-95/152-E, 1995.

[30] D. Möhl, G. Petrucci, L. Thorndahl and S. van der Meer, Physics Reports **C58** 73 (1980); M. D. Church and J. P. Marriner, Annu. Rev. Nucl. Part. Sci. **43** 253 (1993)

[31] Joey Thompson, FERMILAB-TM-1909 and DØ internal report No. 2367, October 1994

[32] DØ Collaboration, S. Abachi *et al.*, Nucl. Instr. and Meth. in Phys. Res. **A338**, 185 (1994)

[33] M. Paterno, DØ internal report No. 1782, 1993 (unpublished)

[34] DØ Collaboration, S. Abachi *et al.*, Phys. Rev. **D52**, 4877 (1995)

[35] ALEPH Collaboration, Buskulik *et al.*, Zeit. Phys. **C62**, 539 (1994); DELPHI Collaboration, Abreu *et al.*, Nucl. Phys. **B418**, 403 (1994); L3 Collaboration, Acciari *et al.*, Zeit. Phys. **C62**, 551 (1994); OPAL Collaboration, Akers *et al.*, Zeit. Phys. **C61**, 19 (1994)

[36] CDF Collaboration, F. Abe *et al.*, Phys. Rev. Lett. **69**, 2898 (1992)

[37] T. Sjöstrand, Computer Physics Comun. **82**, 74 (1994)

[38] Based on the CERN program GEANT: R. Brun and F. Carminati, CERN Program Library Long Writeup W5013, 1993 (unpublished)

[39] W. G. D. Dharmaratna, R. Raja and C. Stewart, DØ internal report No. 1730, May 1993, (unpublished).

[40] F. Paige and S. Protopopescu, BNL Report no.BNL38034, 1986 (unpublished).

[41] DØ Collaboration, S. Abachi *et al.*, Phys. Rev. Lett. **72**, 965 (1994)

[42] D. M. Norman, Ph.D. Thesis, University of Maryland, 1993 (unpublished)

[43] U. Heintz and M. Narain, DØ internal report No. 1814, July 1993, (unpublished). S. Chopra, U. Heintz and M. Narain, DØ internal report No. 2351, December 1994 (unpublished).

[44] J. Ohnemus, Phys. Rev. **D44**, 1403 (1991)

[45] Particle Data Group, *Review of Particle Properties*, Phys. Rev. **D50**, Part I p. 1281 (1994)

[46] R. D. Cousins and V. L. Highland, Nucl. Instr. Meth. **A320**, 331 (1992)

[47] Danilo Pušeljić, private communication

[48] P.B. Arnold and R. Kauffman, Nucl. Phys. **B349**, 381 (1991)

[49] DØ Collaboration, S. Abachi *et al.*, Phys. Rev. Lett. **75**, 1456 (1995)

[50] F. James, CERN Program Library Long writeup D506, CERN (1978)